The Pennsylvania State University

The Graduate School

EXPLORING MAGNETISM IN VAN DER WAALS

2D MATERIALS AND HETEROSTRUCTURES

A Dissertation in

Physics

by

Ya-Wen Chuang

Submitted in Partial Fulfillment
of the Requirements
for the Degree of

Doctor of Philosophy

August 2020

The dissertation of Ya-Wen Chuang was reviewed and approved by the following:

Jun Zhu

Professor of Physics

Dissertation Advisor, Chair of Committee

Vincent Crespi

Distinguished Professor of Physics, Materials Science and Engineering, and Chemistry

Mauricio Terrones

Verne M. Willaman Professor of Physics

Distinguished Professor of Physics

Professor of Chemistry and Materials Science & Engineering

Roman Engel-Herbert

Associate Professor of Materials Science and Engineering and Physics

Nitin Samarth

Professor of Physics

George A. and Margaret M. Downsbrough Department Head

Abstract

Since the successful isolation of graphene in 2004, 2D van der Waals materials have drawn a lot of interests of the community because of their potential in advancing fundamental physics understandings and next-generation device applications. Van der Waals materials with diverse properties have been synthesized and studied and many fundamental phenomena of condensed matter physics including the quantum Hall effect, superconductivity, and magnetism have been observed. Robust room-temperature 2D magnetism remains a goal of the field.

We have explored three van der Waals 2D materials to realize magnetism. This includes bilayer graphene, gallium selenide (GaSe), and manganese bismuth telluride ($MnSb_{1.8}Bi_{0.2}Te_4$). A strain-tuning technique based on a piezoelectric substrate is developed and will offer convenient tuning of magnetic properties. This dissertation begins with an introduction, which is followed by four chapters, each of which discusses a material platform or technique.

Chapter 1 gives an overview of the properties of 2D materials, which forms the basis of our investigations in the following chapters. We discuss different ways to manipulate the properties of 2D materials. Chapter 1 also gives a brief introduction on the current state of magnetism in 2D.

Chapter 2 presents findings in WSe_2/bilayer graphene heterostructures. Our original goal was to introduce spin-orbit coupling into bilayer graphene through proximity coupling. The effect was found to be very small. Instead we observed large modifications to the Landau level energies of bilayer graphene, which suggests a possible way to

engineer the quantum Hall effect. A systematic study of Landau level gaps at filling factors $\nu = 1, 2, 3$ is presented and offers insight to the rich competing many-body interactions in bilayer graphene.

Chapter 3 describes our effort in making electrical contacts to GaSe using various materials and procedures. We also discuss different fabrication ideas to enhance the quality of GaSe devices. Our original goal was to study the predicted gate-tunable ferromagnetism in few-layer GaSe. We were not successful in the end however this work provides valuable information to the challenging problem of contacting thin GaSe flakes.

Chapter 4 reports our observations of a ferromagnetic ground state in $MnSb_{1.8}Bi_{0.2}Te_4$, a van der Waals magnetic compound. This work was done with collaborators in synthesis and structural characterizations. The development of ferromagnetism in $MnSb_{1.8}Bi_{0.2}Te_4$, in contrast to commonly observed anti-ferromagnetism in this family of materials, is supported by magneto-transport measurements, bulk magnetometry and neutron scattering. Our finding contributes to the understanding of a newly discovered family of ferromagnetic topological insulators.

Chapter 5 describes our design and fabrication of a strain-tuning substrate that is based on piezoelectric lead zirconate titanate (PZT) and suitable for devices made of van der Waals materials. Strain is a powerful tool for manipulating 2D material properties, including magnetism. Our substrate integrates strain tuning, Al_2O_3 gating, ionic liquid gating, and electrical measurement capabilities. We aim for a platform compatible with cryogenic measurements and available for convenient and reliable strain tuning.

Table of Contents

Chapter 1:

Introduction

Chapter 2:

Landau Levels of Bilayer Graphene

Chapter 3:

Toward Better Electrical Contact to Few-Layer GaSe

Chapter 4:

Ferromagnetism in van der Waals Compound MnSb$_{1.8}$Bi$_{0.2}$Te$_4$

Chapter 5:

Piezoelectric Substrate for 2D Materials

List of Figures

List of Tables

List of Abbreviations

AFM – antiferromagnetic

BLG – bilayer graphene

BN – hexagonal boron nitride

CDW – charge density wave

LL – Landau level

PDMS – poly dimethyl siloxane

PMMA – poly(Methyl MethAcrylate)

PPC – propylene carbonate

QAHE: quantum anomalous Hall effect

SOC – spin orbit coupling

TMD – transition metal dichalcogenide

Acknowledgements

Chapter 1

Introduction

1.1 Introduction of 2D Materials

Graphene was the first 2D material that was isolated experimentally [1]. Before that, it was a hypothetical material since atomically-thin 2D materials were believed to be unstable compared to curved structures like fullerenes and nanotubes. Graphene turns out to be an air-stable 2D material with many outstanding properties. Some advantages are inherent by being a 2D material: lightweight, flexible, and transparent, which make graphene a good candidate for making foldable touch screens and wearable electronics. But it possesses more unique properties that make it stand out from all the 2D materials. Firstly, its electrical and thermal conductivity are among the highest. It has an unprecedentedly high room-temperature mobility up to 140,000 cm^2/Vs [2]. Its carrier density and carrier type can be easily tuned by gating. Being an atomically thin material with strong σ bonds, graphene is both flexible and mechanically strong [3]. It also has an excellent biocompatibility with a variety of biomolecules, such as cells, enzymes, antibodies, and proteins, which makes it a promising material for making biosensors with large surface area [4].

However, monolayer graphene has a drawback which prevents it from being applied in semiconductor industry—it does not have a band gap. Bilayer graphene not only inherits all the above advantages from graphene, but also has a band gap that can be controlled by a perpendicular electric field. More interestingly, such property offers us a way to control the pseudospin, the extra degree of freedom in stemming from the inequivalent K and K' valleys [5-7]. In a magnetic field, bilayer graphene has an 8-fold

degenerate zero energy Landau level, which offers a playground for the study of competing many-body interactions. We will go into more detail in Chapter 2.

The success of graphene stimulates the search and studies of other 2D materials, or 2D van der Waals materials. In van der Waals materials, different layers are weakly bonded by van der Waals force while intralayer bondings are formed by strong covalent or ionic bondings, or both. When a van der Waals material is thinned down to one to a few atomic layers, it becomes a 2D material in which 2D properties distinct from those of bulk parental materials emerge. Van der Waals materials span a wide electronic spectrum from insulating hexagonal boron nitride (BN) to semiconducting transition metal dichalcogenides (TMDS) to superconducting $NbSe_2$.

In the search for semiconducting 2D materials, TMDs gain a lot of attention due to their excellent properties such as indirect-to-direct band gap transitions [8] and strong spin orbit coupling (SOC) [9]. Their unique properties make them good candidates for fundamental studies and applications in spintronics [10], optoelectonics [11], and energy harvesting [12].

TMDs have the molecular form as MX_2, where M is a transition metal atom (such as Mo or W) and X is a chalcogen atom (such as S, Se or Te). Like the graphene system, they are van der Waals materials. TMDs exist in several different structural phases and the most common phases are trigonal prismatic (2H) and octahedral (1T) phases (Figure 1-1). These phases can be viewed in terms of the stacking order of the three atomic planes (chalcogen-metal-chalcogen) [13]. The 2H phases correspond to the ABA stacking, where the chalcogen atoms of different planes occupy the same position A and sit on top of each other in the direction perpendicular to the plane. The 1T phases are

characterized by an ABC stacking. For five of the six TMDs formed by group VI transition metals (M = Mo or W and X = S, Se or Te), the 2H phase is thermodynamically stable and 1T phase can be obtained as a metastable phase [13]. The exception is WTe_2, whose thermodynamically stable bulk phase at room temperature is the orthorhombic $1T_d$ phase. Figure 1-2 shows a "periodic table" of TMDs summarizing the electronic phases such as charge density wave (CDW), superconductive, and topological phases. This figure also confirms the versatility of 2D materials.
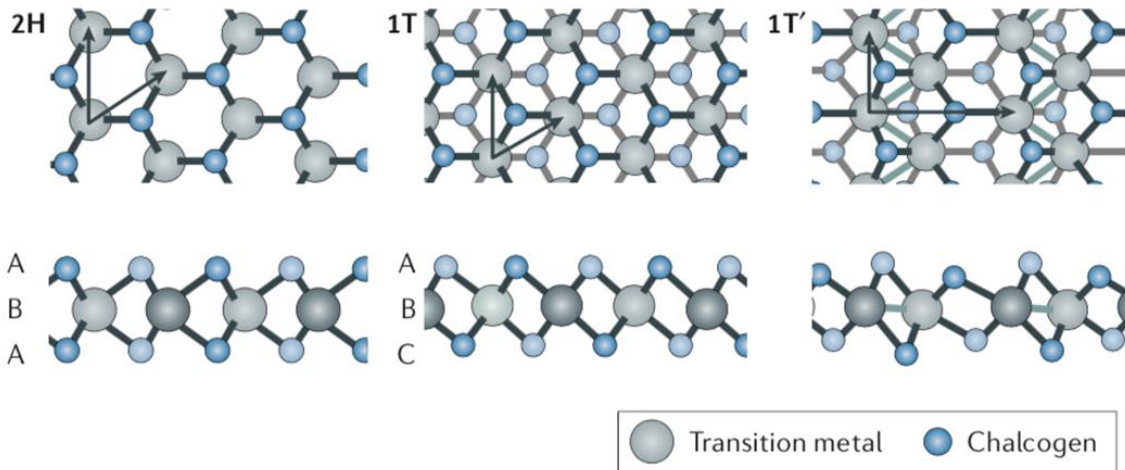
Figure 1-1. Lattice structures of monolayer TMD.
Three common phases are shown: trigonal prismatic (2H), distorted octahedral (1T) and dimerized (1T') phases. 2H phase features ABA stacking while 1T and 1T' phases are characterized by ABC stacking. The arrows represent the lattice vectors. (Figures taken from Ref. [13].)

IV   V

Ti — M, I / CDW / SC / -

V — M / CDW / - / -

VI

Zr — M, I / - / -

Nb — M / CDW / SC / M / CDW / SC / -

Mo — I / - / SC / dis / M, I / - / Topo

VII

X

Pd — I / - / SC

	2H		1T
dis		Distorted	
M		Metallic	
I		Insulating	
CDW		Charge density wave	
SC		Superconducting	
Topo		Topological	

Hf — M, I / - / -

Ta — M / CDW / SC / M / CDW / SC / -

W — I / - / SC / dis / M, I / - / Topo

Re — dis / I / - / -

... **Pt** — M, I / - / -
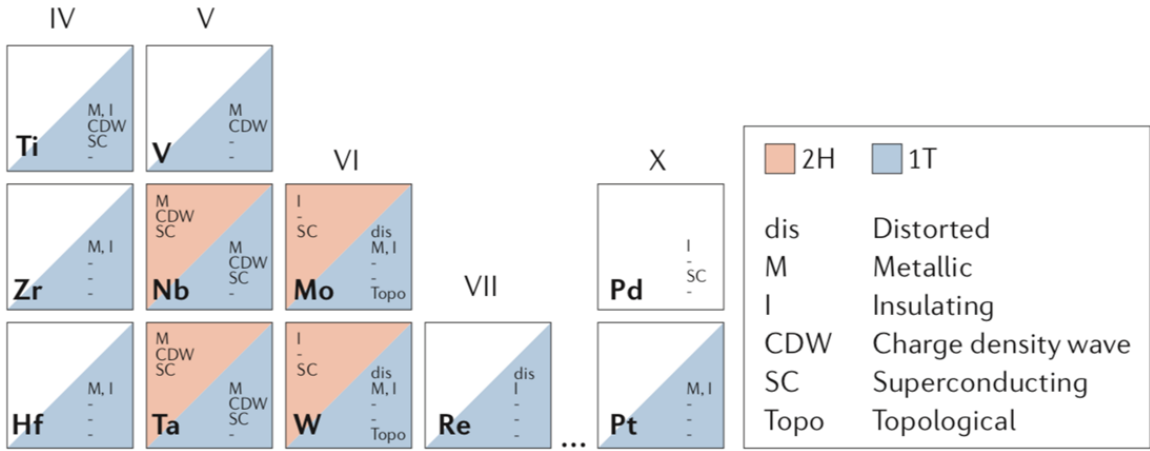
Figure 1-2. "Periodic table" organized based on the transition metal involved.
The table lists different structural and electronic phases found before June 2017. (Figures taken from Ref. [13].)

Although not gaining as much attention as 2D TMDs, 2D transition metal monochalcogenides, such as GaSe, GaS, and InSe, have electronic and optoelectronic properties distinct from TMDs [14-18]. As a typical representative, few-layer GaSe simultaneously has superior nonlinear optical properties with a wide transparency range [14, 19], high photoresponsibility [20], layer-dependent band gap, and direct-to-indirect band gap transition [17, 18, 21]. GaSe has also been predicted to have a carrier-density-dependent ferromagnetism [18], which we will discuss more in Chapter 3.

There are various ways to obtain 2D materials. Graphene was firstly isolated via mechanical exfoliation [1], which is also a major method to obtain high-quality single-crystal few-defect flakes of most 2D materials. In addition, mechanical exfoliation produces flakes with smaller bonding with the substrate so the flakes can be more easily dry transferred and made into heterostructures. Mechanical exfoliation relies on the probability of most layers adhere to the tape and few layers adhere to the substrate.

Therefore compared to other synthesis methods, the yield is low, the size is relatively small, the flake thickness is not controllable, and the person-dependent manual process is less controllable and difficult to be completely reproduced by others. Researchers have worked on improving the yield of larger flakes from mechanical exfoliation. For example, Huang et al. developed a modified method with additional substrate cleaning and heating which yields hundreds-of-micron size of graphene and bismuth strontium calcium copper oxide [22]. Desai et al. showed that gold substrate can increase the yield of large TMD flakes [23].

Besides top-down methods like mechanical exfoliation, bottom-up methods such as molecular beam epitaxy (MBE), chemical vapor deposition (CVD), and metal-organic chemical vapor deposition (MOCVD) have been utilized to produce 2D materials. These methods share one advantage that mechanical exfoliation lacks: scalability [24]. Epitaxially grown 2D materials are single-crystalline and clean because the films are grown in high vacuum or ultra-high vacuum [25, 26]. Epitaxial techniques also provide control over layer thickness. On the other hand, CVD offers a low-cost and relatively simple route for large-scale 2D material growth, which makes it applicable in industry [17, 27-30]. Compared to CVD, MOCVD provides more control over grown material with better homogeneity [31]. MOCVD can grow large-scale 2D materials layer by layer [32]. One of its favorable abilities is that it can grow several different materials in one apparatus and thus grow new heterostructures [33]. It can also grow a wide range of 2D materials that cannot be grown in other methods [34]. Limitation of both CVD and MOCVD are their relatively high impurity and defect levels.

1.2 Tuning Knobs for 2D Materials

There is a large toolkit to manipulate the properties of 2D materials, such as gating, doping, making heterostructures by growth or transfer, pressure, and strain modulation. A table summarizing several different techniques is organized in a review paper of Bhimanapati et al. [24]. We will focus on strain modulation and heterostructure in the following.

Strain can be an effective control knob tuning properties related to lattice constants, like superconductivity [35] , ferroelectricity [36], ferroelasticity [37], electronic properties [38, 39], optical properties [40], and magnetism [41-43]. External strain can be applied through various methods. Tensile strain can be applied by pushing a suspended flake with a microscope tip [3, 44, 45], which produces strain in the range around 0.1 ~3% [44, 46]. Flexible substrate such as PDMS together with a holding stage offer a platform that can provide uniaxial tensile strain up to 30% and bending strain up to 18.7% [27]. But the above methods cannot produce homogeneous compressive or biaxial strain. Piezoelectric substrate is a good way to achieve highly controllable biaxial tensile or compressive strain [46, 47]. Piezoelectric can also be integrated into electronic devices more easily. I will describe our piezoelectric substrate fabrication procedure in Chapter 5.

The ability of forming heterostructures largely increase the functionality of 2D materials. Desired properties from different materials can possibly be achieved simultaneously by stacking these materials together. For example, air-stable BN is often incorporated in van der Waals heterostructures as a substrate free of dangling bonds for a high-quality device, a capping layer to prevent other 2D materials from quick oxidation, and as well as a gating dielectric [2, 7, 48-52]. Heterostructures of TMD/graphene have

been fabricated to integrate graphene's striking electronic properties and TMD's strong SOC [53-57].

Stacking 2D materials in a manner as wished is challenging because the lateral dimension of each flake is often tens of microns or smaller and flakes can be easily folded or broken due to their atomic thinness. The first graphene on BN substrate is demonstrated with a wet transfer method by Dean et al. [48]. The technique starts by exfoliating BN onto a SiO_2/Si substrate. Graphene flakes are exfoliated onto substrate coated with a water-soluble layer and a hydrophobic Poly(Methyl MethAcrylate) layer (PMMA). Later the substrate is floated on the surface of water and the water-soluble polymer dissolves. The floating PMMA film with flakes is then fished by a transfer slide and transferred onto a substrate with BN under an optical microscope. Graphene devices fabricated this way have mobility about an order higher than graphene on SiO_2 substrate and have a sharper resistance peak as a function of carrier density [48]. However contaminants are introduced during this transfer method. This wet transfer method is not suitable for transferring materials which are less stable and oxidize faster in humid air, such as GaSe.

A dry, contamination-free transfer technique is developed by Wang et al. in 2013 [2]. The method begins with exfoliation of BN (as top BN) onto a Si substrate coated with propylene carbonate (PPC). A desired top BN flake is identified optically. Later the PPC film is manually peeled from the Si substrate and put onto a transparent elastomer stamp (poly dimethyl siloxane, PDMS) with BN facing upward. The stamp is then affixed onto a slide. In parallel, BN (as bottom BN) and graphene flakes are exfoliated onto separate substrates. After a target graphene flake is identified, the PDMS stamp is positioned so

the top BN is aligned with the target graphene. Afterward, the top BN flake is brought into contact with the graphene flake. Due to the stronger van der Waals bonding between graphene and BN, graphene adheres to BN and is removed from its substrate after the stamp is lifted. Bottom BN flake can be added to the bottom of graphene with the same procedure. Finally the BN/graphene/BN heterostructure is released onto another clean substrate by increasing the platform temperature to melt the PPC film. To contact graphene, the heterostructure is etched by CHF_3/O_2 plasma to expose graphene edge for Cr/Pd/Au contact. Graphene devices fabricated by this method achieve mobility of 140,000 cm^2/Vs, which is comparable to the theoretical phonon scattering limit [58, 59]. And surprisingly the one-dimensional edge contact has a substantially lower contact resistance than a typical plane contact.

Van der Waals heterostructure is a very flexible platform. Besides stacking different materials, the properties of the heterostructures can be manipulated by the "twist angle", the rotation between crystals. By stacking two monolayer graphene with a small angle, the stacked material, twisted bilayer graphene, exhibits insulating and superconducting states absent in a single graphene sheet [60, 61]. Such exciting finding opens up a new field of "twistronics". Twisted bilayer graphene offers a platform to study strongly correlated electron phenomena, which yields unconventional forms of superconductivity and magnetism [62-64].

1.3 Toward 2D Magnetism

In modern electronics, information processing and information storage are achieved by different techniques and in different materials: the former is accomplished by semiconductor devices while the latter utilizes magnetic metals [65]. Magnetic semiconductors have the potential to integrate information processing and storage in one material, thus advancing electronics to the next generation [66]. The study of magnetism in 2D layered materials can potentially contribute to both fundamental knowledge and application potentials of this class of materials. Based on Heisenberg model, Magnetism is forbidden in isotropic 2D materials [67]. In other words, long-range magnetic ordering in 2D systems requires lowering the symmetry, which can be provided by the substrate [68], an external magnetic field, or anisotropic crystal structure [69].

There may be several approaches towards the synthesis of a 2D magnetic materials. Inspired by previous research in diluted magnetic semiconductors [70 , 71, 72], efforts have been made to dope manganese (Mn) into monolayer MoS_2 [73]. The studies show that the incorporation of Mn sensitively depends on the substrate of growth and increasing the Mn concentration to over 2 atom % leads to the loss of 2D morphology of MoS_2. However, theory predicts that 10 atom % Mn might be necessary to achieve room-temperature ferromagnetism in monolayer MoS_2 [74].

We tried an alternative approach to obtain magnetic 2D semiconductors, which is realizing a 2D semiconductor that is predicted to have a carrier-driven ferromagnetic phase transition in the valence band. Calculations show that when doped to carrier density around $3\times10^{13} \sim 1\times10^{14}/cm^2$, monolayer GaSe undergoes a ferromagnetic phase transition [18]. In graphene, the formation of the magnetism by introducing another kinds

of atoms or defects is theoretically predicted. However, the experimental results are ambiguous when we started this study in 2016 [75, 76]. Furthermore, the predicted carrier density-drive phase transition in GaSe may have important technological consequences since the carrier density in a semiconductor can be controlled by a gate. In 2018, gate-tunable magnetism was reported in CrI_3, $Cr_2Ge_2Te_6$, and Fe_3GeTe_2 [77-80]. In the case of GaSe, it is challenging to make electrical contact to atomically thin GaSe due to its large band gap, which increases with decreasing layer number [17, 21] and reaches a band gap of 3.3 eV in monolayers. Chapter 3 discusses the efforts we made in fabricating GaSe devices with better electrical contact.

The first 2D magnetism was realized in flakes mechanically exfoliated from bulk-ferromagnetic materials CrI_3 and $Cr_2Ge_2Te_6$ in 2017, which was observed using magneto-optical Kerr effect microscopy technique [68, 81]. Monolayer, bilayer, and trilayer CrI_3 flake show ferromagnetic coupling within individual layer with out-of-plane easy axis and interlayer antiferromagnetic order. The Curie temperature of monolayer is 45 K, slightly lower than that of the bulk crystal 61 K. Few-layer $Cr_2Ge_2Te_6$ is a soft ferromagnetic crystal whose paramagnetism/ferromagnetism phase transition can be achieved at a low magnetic field of 0.3 T. One year later, bulk VSe_2 was reported to have ferromagnetic ordering in monolayer limit and such ferromagnetic ordering can persist to above room temperature [82].

More recently, an even more interesting van der Waals material family with both magnetic and topological properties are caught in the spotlight. Recent research activities have identified $Mn(Bi, Sb)_2Te_4$ to be promising candidates in realizing the quantum anomalous Hall effect (QAHE) above dilution refrigerator temperatures [83-94]. Like

CrI$_3$, most members in Mn(Bi, Sb)$_2$Te$_4$ have intralayer ferromagnetic order and interlayer antiferromagnetic order. For an antiferromagnetic material to achieve QAHE, its layer number needs to be odd to achieve unbalanced layer polarization. QAHE has been realized in MnBi$_2$Te$_4$ [86]. The odd-layer-number restriction can be lifted in a ferromagnetic material. Furthermore, ferromagnetic order was reported to be able to stabilize QAHE against thermal fluctuations and realize QAHE at a higher temperature [86]. In Chapter 4, we presented our finding of a ferromagnetic phase in thin MnSb$_{1.8}$Bi$_{0.2}$Te$_4$ flakes.

Despite that many exciting new phenomena have been observed, there is a long way toward the realization of controllable and robust 2D magnetism. Many challenges remain in this field, such as understanding the origin and mechanism of 2D magnetism thoroughly, producing larger-area 2D materials, controlling spin polarization, reaching a higher operating temperature, and integrating the new materials into modern electronic devices [69].

Chapter 2

Landau Levels of Bilayer Graphene

2.1 Introduction to Monolayer and Bilayer Graphene

This chapter will start from introducing monolayer and bilayer graphene's lattice structures, electronic structures, and a tight-binding model capturing their low-energy bands. Then we will use a semiclassical model to derive the results of quantum Hall effect in a general 2D system and in bilayer graphene. We will focus on $E = 0$ octet in bilayer graphene, share our systematic study of the D- and B-dependences of $v = 1, 2, 3$ gaps in BN encapsulated WSe$_2$/BLG heterostructures, and give a quantitative comparison to the corresponding energies in pristine BLG.

2.1.1 Lattice and electronic structures

This section is based on the review paper of McCann et al. [95]. Graphene is a single atomic layer of carbon atoms bonded in hexagonal lattice structure (shown in Figure 2-1(a)). The primitive lattice vectors $\mathbf{a_1}$ and $\mathbf{a_2}$ can be expressed in the following form:

$$\boldsymbol{a_1} = \left(\frac{a}{2}, \frac{\sqrt{3}a}{2}\right), \qquad \boldsymbol{a_2} = \left(\frac{a}{2}, -\frac{\sqrt{3}a}{2}\right), \tag{2-1}$$

where $a = |\boldsymbol{a_1}| = |\boldsymbol{a_2}| = 2.46\text{Å}$ is the lattice constant, the distance between adjacent cells. Note that a is not the distance between adjacent carbon atoms, which is $a_{CC} = a/\sqrt{3} = 1.42\text{Å}$. One unit cell has two carbon atoms, labelled as A and B in Figure 2-1(a). The atomic sites of A and B are inequivalent because they cannot be connected by a lattice vector of the form $\mathbf{R} = $ n$_1$$\mathbf{a_1}$ + n$_2$$\mathbf{a_2}$. Graphene (monolayer) and bilayer graphene have the same reciprocal lattice, which is illustrated in Figure 2-1(b). The primitive

reciprocal lattice vectors $\mathbf{b_1}$ and $\mathbf{b_2}$ can be chosen to follow the convention $\boldsymbol{a_i} \cdot \boldsymbol{b_i} = 2\pi$ and $\boldsymbol{a_i} \cdot \boldsymbol{b_j} = 0$ $(i \neq j)$. Thus we have

$$\boldsymbol{b_1} = \left(\frac{2\pi}{a}, \frac{2\pi}{\sqrt{3}a}\right), \qquad \boldsymbol{b_2} = \left(\frac{2\pi}{a}, -\frac{2\pi}{\sqrt{3}a}\right). \qquad (2\text{-}2)$$

There are two inequivalent K and K' points at the corners of the first Brillouin zone (shaded area in Figure 2-1 (b)). We are particularly interested in the energy bands near K and K' points because the low-energy bands only appear in these regions.

Bilayer graphene can exist in the AB form, which is also called the Bernal-stacked form, or in the metastable AA form, which is less common. In the dissertation, I will focus on the Bernal-stacked bilayer graphene. The Bernal-stacked bilayer graphene has two coupled monolayers with interlayer spacing 3.35Å [96] and a unit cell consisting of four atoms (Figure 2-1 (c) and (d)). Atomic sites B1 and A2 are called dimer sites, where they are vertically aligned. Atomic sites A1 and B2 are non-dimer sites, at which atoms do not have counterparts that are directly above or below on the other layer.
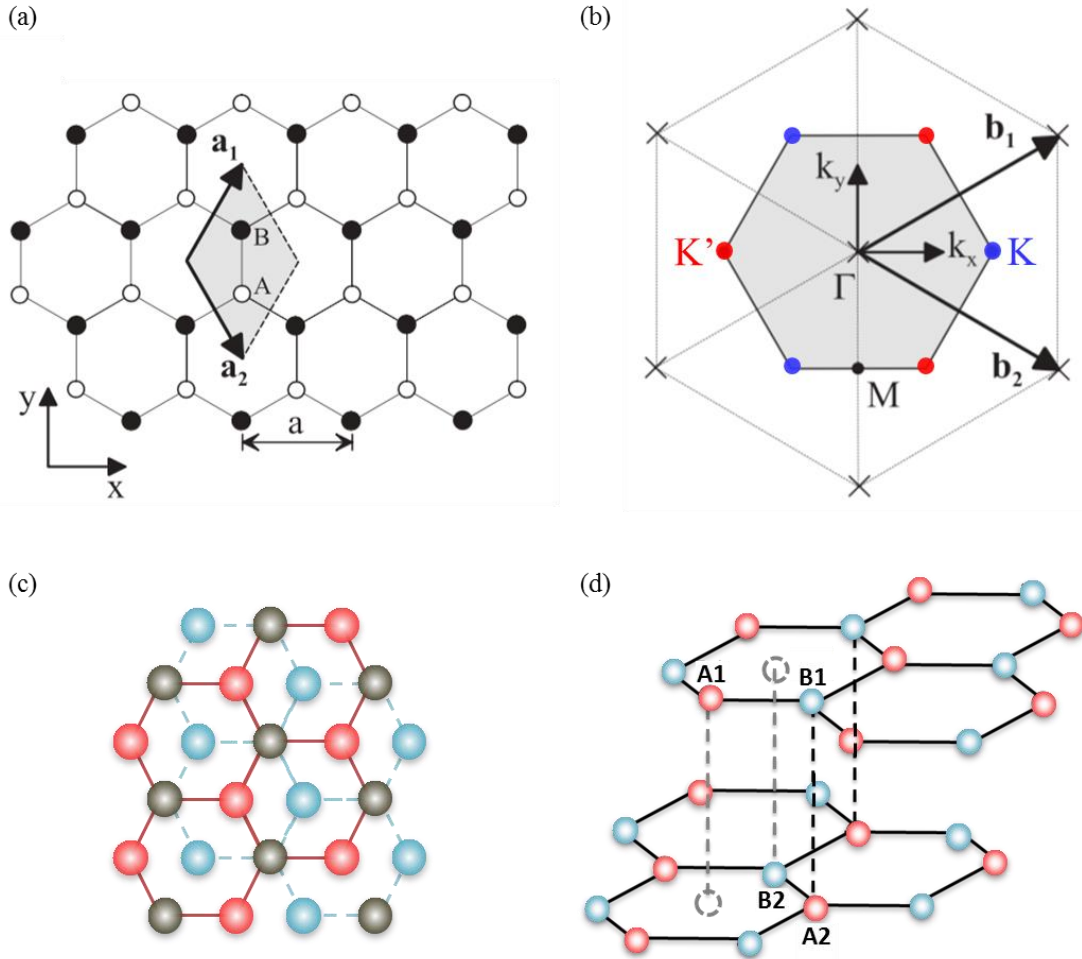
Figure 2-1. Crystal structure of monolayer and bilayer graphene.

(a) Crystal structure of monolayer graphene. A and B sublattices are shown as white and black circles, respectively. The shaded rhombus is a conventional unit cell with primitive lattice vectors a_1 and a_2. The lattice constant a = 2.46Å [97]. (b) Reciprocal lattice of monolayer and bilayer graphene. b_1 and b_2 are primitive reciprocal lattice vectors and the lattice points are marked by crosses. The shaded hexagon is the first Brillouin zone with Γ at its center and two inequivalent corners, K (blue) and K'(red). (c) and (d) are top and side view schematic of Bernal stacked bilayer graphene lattice structure. In (c), teal and red circles illustrate non-dimer atomic sites A_1 and B_2 respectively. At non-dimer sites, carbon atoms do not overlap with any atom from the other layer. Gray circles denote dimer sites, where carbon atoms from the top layer at B_1 site sits on A_2 sites of the bottom layer. (Figure 2-1 (a) and (b) are from McCann et al. [95].)

2.1.2 The tight-binding model

This section describes the tight-binding model and its application to bilayer graphene following the derivation of Slonczewski et al. [98] and McCann et al. [95]. Tight-binding model starts from atomic orbitals and assume a simple form of wave functions. So it is often the basis for constructing models that are more realistic but more complicated.

In monolayer graphene, 2p$_z$ orbitals form π bonds and contribute to the electronic conductivity. So let's just take into account the 2p$_z$ orbital at each site in a unit cell and use them as the basis: $\{|\phi_m\rangle\} = \{|\phi_A\rangle, |\phi_B\rangle\}$. Consider interaction between nearest neighbors. Set the on-site energies as zero: $\langle\phi_A|\mathcal{H}|\phi_A\rangle = \langle\phi_B|\mathcal{H}|\phi_B\rangle = 0$. Then we can write the Hamiltonian in the following form [95]:

$$H_\xi = v_F \begin{pmatrix} 0 & \xi p_x - ip_y \\ \xi p_x + ip_y & 0 \end{pmatrix}. \tag{2-3}$$

$\xi = \pm 1$ represent K and K' valleys, respectively. Fermi velocity $v_F = \sqrt{3}a\gamma_0/2\hbar$, where a is the lattice constant a = 2.46Å and γ_0 is a Slonczewski-Weiss-McClure (SWM) parameter $\gamma_0 = \langle\phi_A|\mathcal{H}|\phi_B\rangle$, describing the intralayer nearest neighbor hopping [98]. Note that in graphene the Fermi velocity is independent of momentum. The eigenenergies and eigenstates of the Hamiltonian are

$$E_\pm = \pm v_F p, \quad \psi_\pm^\xi = \begin{pmatrix} \psi_A \\ \psi_B \end{pmatrix} = \frac{1}{\sqrt{2}} e^{i\vec{p}\cdot\vec{r}/\hbar} \begin{pmatrix} e^{-i\xi\theta/2} \\ \pm\xi e^{i\xi\theta/2} \end{pmatrix} \tag{2-4}$$

where θ is defined as $\tan(\theta) = \frac{p_y}{p_x}$. The eigenenergy is linear in momentum so graphene has a linear dispersion, satisfying massless Dirac equation. Thus the low energy bands in graphene are called Dirac cones and the zero energy point is referred as Dirac point. There are two components in the wavefunction, just like spin-1/2 system. If all electron

density is at site A, the wavefunction can be written as $\begin{pmatrix} 1 \\ 0 \end{pmatrix}$ and the state can be viewed as a "pseudospin up" $|\uparrow\rangle \equiv \begin{pmatrix} 1 \\ 0 \end{pmatrix}$. Similarly the state with all electron density at site B can be viewed as a "pseudospin down" $|\downarrow\rangle \equiv \begin{pmatrix} 0 \\ 1 \end{pmatrix}$. Usually a system is at a superposition state of the pseudospin up and down.

In bilayer graphene, a band structure shown in Figure 2-2(b) can be obtained if we consider one $2p_z$ orbital from each of the four atoms in the unit cell. There are four bands: a pair in valence band and the other pair in conduction band. Throughout most of Brillouin zone, each pair is separated by an energy of the order of the coupling between the dimers γ_1 ($\gamma_1 = \langle \phi_{A2} | \mathcal{H} | \phi_{B1} \rangle$). Because there is much larger overlap of $2p_z$ orbitals between the dimer sites than the non-dimer sites, the high-energy bands are the bonding and anti-bonding bands formed by the strongly-coupled dimer sites. The lower-energy bands arise from the coupling between non-dimer sites. In pristine bilayer graphene, the Fermi level lies at where the two low-energy bands touch ($E = 0$ in Figure 2-2(b)). Because low energy band only appears near K and K' points, region near K and K' points is relevant for the study of electronic properties and will be the focus in this chapter. The energy bands centered at K (K') points are called K (K') valleys.

In the SWM model that describes bulk graphite, four hopping parameters can be defined in bilayer graphene as following [98]:

$$\gamma_0 = -\langle \phi_{A1} | \mathcal{H} | \phi_{B1} \rangle = -\langle \phi_{A2} | \mathcal{H} | \phi_{B2} \rangle,$$

$$\gamma_1 = \langle \phi_{A2} | \mathcal{H} | \phi_{B1} \rangle, \tag{2-5}$$

$$\gamma_3 = -\langle \phi_{A1} | \mathcal{H} | \phi_{B2} \rangle,$$

$$\gamma_4 = \langle \phi_{A1} | \mathcal{H} | \phi_{A2} \rangle = \langle \phi_{B1} | \mathcal{H} | \phi_{B2} \rangle.$$

Figure 2-2(a) illustrates the hopping parameters in bilayer graphene's crystal structure. γ_0 is the coupling between the nearest neighbors of the same layer (different sublattices) and γ_4 is the interlayer coupling between same sublattices. γ_1 and γ_3 are the coupling between the dimers and non-dimers, respectively.
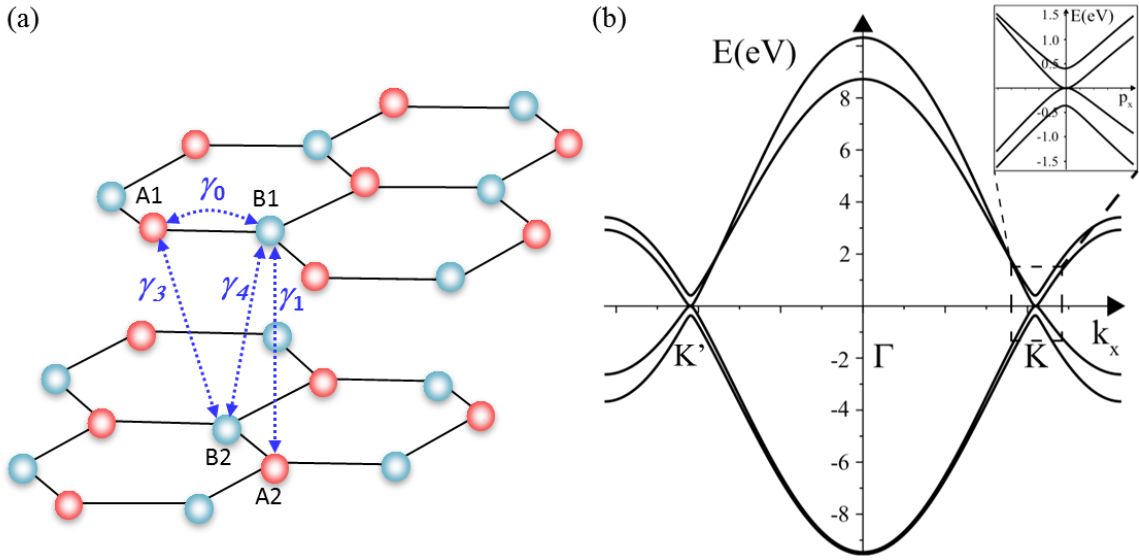
Figure 2-2. Hopping parameters and energy bands of bilayer graphene.

(a) Crystal structure of bilayer graphene with tight-binding hopping parameters γ_0, γ_1, γ_3, γ_4 labeled. B_1 and A_2 are dimer sites. A_1 and B_2 are non-dimer sites. (b) Energy bands of bilayer graphene arising from $2p_z$ orbitals along k_x axis. The inset shows the enlarged view near K point. Plots were made with parameter values $\gamma_0 = 3.16eV$, $\gamma_1 = 0.381eV$, $\gamma_3 = 0.38eV$, $\gamma_4 = 0.14eV$. The on-site energy is set as 0 at non-dimer sites and is 0.022eV at dimer sites [99]. (Figure 2-2(b) is adapted from McCann et al. [95].)

We are interested in the energy bands near the Fermi level so let's apply low-energy approximation and use orbitals on the non-dimer sites as the basis $\{|\phi_m\rangle\} =$

$\{|\phi_{A1}\rangle, |\phi_{B2}\rangle\}$. Set the on-site energy at the non-dimer sites as zero. Then the Hamiltonian takes the following form:

$$H_\xi = -\frac{1}{2m^*}\begin{pmatrix} 0 & (\xi p_x - ip_y)^2 \\ (\xi p_x + ip_y)^2 & 0 \end{pmatrix}$$
(2-6)

where effective mass can be written in the form $m^* = \frac{\gamma_1}{2v_F^2}$ and γ_1 describes the hopping between the two dimer sites. The eigenenergies and eigenfunctions of the Hamiltonian are

$$E_{\pm} = \pm\frac{p^2}{2m^*} \quad, \quad \psi_{\pm}^{\xi} = \begin{pmatrix} \psi_{A1} \\ \psi_{B2} \end{pmatrix} = \frac{1}{\sqrt{2}}e^{i\vec{p}\cdot\vec{r}/\hbar}\begin{pmatrix} e^{-i\xi\theta} \\ \mp\xi e^{i\xi\theta} \end{pmatrix}.$$
(2-7)

One can also define pseudospin in bilayer graphene. Interestingly the pseudospin degree of freedom in bilayer graphene is correlated with the distribution of electrons in the two graphene layers in the low energy approximation. All electrons reside on the top graphene layer in pseudospin up state $|\uparrow\rangle \equiv \begin{pmatrix} 1 \\ 0 \end{pmatrix}$ while all electrons are on the bottom layer in pseudo spin down state $|\downarrow\rangle \equiv \begin{pmatrix} 0 \\ 1 \end{pmatrix}$.

2.1.3 Introduction to integer quantum Hall effect

In classical mechanics, electrons circulate in a magnetic field. And thus when a current flows in a magnetic field perpendicular to it, a potential difference perpendicular to both the current and the field is generated, which is known as Hall effect. There is a quantum-mechanical version of Hall effect, integer quantum Hall effect, in two-dimensional electron gas subject to a high magnetic field at low temperature, in which ρ_{xx} vanishes and ρ_{xy} takes on quantized values. Such complete quantization was

observed experimentally by von Klitzing et al in 1980 [100]. To be more specific, $\rho_{xx} = 0$ and ρ_{xy} takes on quantized values $\rho_{xy} = \frac{h}{\nu e^2}$ when magnetic field $B = \frac{n}{\nu}\Phi_0$. Here ν is an integer known as filling factor, n is carrier density, and $\Phi_0 = \frac{h}{e}$ is magnetic flux quantum. The value of ν is measured to be an integer to extremely high accuracy, about one part in 10^9 [101]. Therefore integer quantum Hall effect is used as a basis to determine the ratio of the fundamental constants $\frac{h}{e^2}$.

In this section, we will derive the key features listed above with a semiclassical model. We will follow the derivation in Ref. [102]. Start from the Hamiltonian for a single electron in a 2D system subject to a magnetic field: $H = \frac{1}{2m}(\boldsymbol{p} + e\boldsymbol{A})^2$ where $\boldsymbol{B} = B\hat{z} = \nabla \times \boldsymbol{A}$. By choosing Landau gauge $\boldsymbol{A} = xB\hat{y}$, Hamiltonian becomes $H = \frac{1}{2m}(p_x^2 + (p_y + eBx)^2)$ and is therefore translationally invariant in y direction. Because H and p_y commute, it is tempting to assume that the eigenfunction of the Hamiltonian takes the form $\psi_k(x,y) = e^{iky}f_k(x)$. Note that the plane wave e^{iky} and $\psi_k(x,y)$ are both eigenstates of the y-momentum operator p_y associated with eigenvalue $\hbar k$. Then H can be rewritten as $H = \frac{1}{2m}(p_x^2 + (\hbar k + eBx)^2) = \frac{p_x^2}{2m} + \frac{m\omega_B^2}{2}(x + kl_B^2)^2$ where $l_B = \sqrt{\frac{\hbar}{eB}}$ is magnetic length of the system and $\omega_B = \frac{eB}{m}$ is cyclotron frequency. Now the Hamiltonian takes the form as a one-dimensional harmonic oscillator centered at $x_0 = -kl_B^2$. For a one-dimensional harmonic oscillator, eigenenergies are $E_j = \hbar\omega_B(j + \frac{1}{2})$ and eigenfunctions are

$$\psi_{j,k}(x,y) \sim e^{iky}u_j(x + kl_B^2), \quad j = 0, 1, 2, \ldots \tag{2-8}$$

where $u_j(x + kl_B^2) \sim e^{-(x+kl_B^2)^2/2l_B^2} H_j(x + kl_B^2)$ is a Gaussian function times a Hermite polynomial. Energy levels associated with the discrete energies E_n are called Landau levels (LLs) (shown in Figure 2-3(a)). Due to the Gaussian function, $\psi_{j,k}(x,y)$ is localized around x₀ on the length scale of l_B. On the other hand, it is completely extended in y direction.

Note that E_n is independent of momentum so we should expect a huge degeneracy at each LL. To calculate the degeneracy, consider a finite sample size $L_x \times L_y$. In y direction, we have $k = \frac{2\pi}{L_y} \times$integer. The harmonic oscillation center has to be within the sample: $0 \leq x_0 = -kl_B^2 \leq L_x$, which gives the condition $-\frac{L_x}{l_B^2} \leq -\frac{x_0}{l_B^2} = k_y \leq 0$. The one-dimensional density of states of plane wave is $\frac{L_y}{2\pi}$. Thus the number of states at each LL is given by $N = \frac{L_y}{2\pi} \int_{-L_x/l_B^2}^{0} dk_y = \frac{L_y L_x}{2\pi l_B^2} = \frac{eBA}{h} = \frac{\Phi}{\Phi_0}$, where A is the area of the sample, $\Phi = AB$ is the total flux through the sample, and $\Phi_0 = \frac{h}{e}$ is the magnetic flux quantum. The Landau level degeneracy is defined as the carrier density needed to fill one LL: $G = \frac{N}{A} = \frac{eB}{h}$. When the νth LL is occupied, the carrier density of the system is $n = \nu G = \frac{\nu N}{A} = \frac{\nu eB}{h}$; in other words, $B = \frac{nh}{\nu e} = \frac{n}{\nu} \Phi_0$.
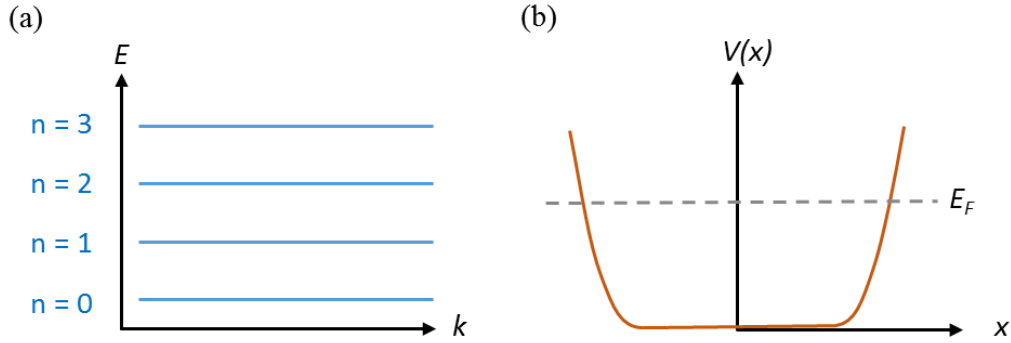
Figure 2-3. Landau level band diagram and potential profile modeling sample edges. (a) Landau level energy band diagram. (b) Potential profile $V(x)$ considered to model the sample edge. $V(x)$ stays as a constant in the bulk and increases rapidly at edges.

To model the sample edges, consider a potential well illustrated in Figure 2-3(b) and the Hamiltonian becomes $H = \frac{1}{2m}\left(p_x^2 + (p_y + eBx)^2\right) + V(x)$. As the wavefunction is localized near x_0 in x direction, $V(x) \approx V(x_0) + (\partial V / \partial x)(x - x_0)$. Now let's look at the group velocity along y direction $v_y = -\frac{1}{eB}\frac{\partial V}{\partial x}$. We see that $v_y = 0$ in the bulk and v_y at the left and right edges have opposite signs. Again due to the localization in x direction, the states on the opposite edges propagate in opposite directions: $v_y > 0$ at the left edge and $v_y < 0$ at the right edge. To backscatter, electrons must travel to the opposite edge. And since the sample width is usually much larger than the magnetic length l_B, which is about 26 nm at 1 tesla and becomes even smaller at higher magnetic field, backscattering is eliminated and the longitudinal resistivity $\rho_{xx} = 0$. We can see that quantum Hall edge modes are chiral, meaning the forward-movers and backward-movers are spacially separated. Such asymmetry is caused by the magnetic field.

Based on classical Hall effect, Hall voltage V_H is built up across the width of the

sample. Let's say the Fermi energy at the right edge is $\Delta\mu = eV_H$ higher than the left.

Therefore the current along y direction $I_y = -\frac{e}{L_y} \int dk \frac{L_y}{2\pi} v_y(k) = \frac{e}{h} \Delta\mu$, where $\frac{e}{L_y}$ is

linear charge density and $\frac{L_y}{2\pi}$ is one-dimensional density of states of plane wave. Hall

voltage $V_H = \frac{\Delta\mu}{e}$ and $\rho_{xy} = \frac{V_H}{I_y} = \frac{h}{e^2}$. When the vth LL is occupied, $\rho_{xy} = \frac{h}{ve^2}$ thus $\sigma_{xy} =$

$v\frac{e^2}{h}$.

2.1.4 Integer quantum Hall effect in bilayer graphene

We are interested in the LLs near the Fermi level of bilayer graphene so let's use low-

energy approximation and write the Hamiltonian on the basis of non-dimers $\{|\phi_m\rangle\} =$

$\{|\phi_{A_1}\rangle, |\phi_{B_2}\rangle\}^T$ as in section 2.1.2 [95]

$$H_\xi = -\frac{1}{2m^*}\begin{pmatrix} 0 & \left(\xi p_x - ip_y\right)^2 \\ \left(\xi p_x + ip_y\right)^2 & 0 \end{pmatrix} \tag{2-6}$$

where $\xi = \pm 1$ denote K and K' valleys, respectively. Choose Landau gauge $\boldsymbol{A} = xB\hat{y}$ so

$\boldsymbol{B} = B\hat{z}$ and translational symmetry in y direction is preserved. Thus the system has the

same set of eigenfunctions as in equation (2-8). Define $\pi = p_x + ip_y + ieB$ and

$\pi^+ = p_x - ip_y - ieB$, and rewrite the Hamiltonian

$$H_K = -\frac{1}{2m^*}\begin{pmatrix} 0 & \left(\pi^+\right)^2 \\ \left(\pi\right)^2 & 0 \end{pmatrix} \text{ and } H_{K'} = -\frac{1}{2m^*}\begin{pmatrix} 0 & \left(\pi\right)^2 \\ \left(\pi^+\right)^2 & 0 \end{pmatrix}. \tag{2-9}$$

In the K valley, π and π^+ are lowering and raising operators for harmonic oscillator,

respectively:

$$\pi\psi_j = -\frac{\sqrt{2}i\hbar}{l_B}\sqrt{j}\psi_{j-1} \text{ and } \pi^+\psi_j = \frac{\sqrt{2}i\hbar}{l_B}\sqrt{j+1}\psi_{j+1}, \qquad (2\text{-}10)$$

where $j = 0, 1, 2, \ldots$, and ψ_j here is the same as $\psi_{j,k}(x,y)$ in equation (2-8). The subscript k is removed to allow easier reading. The eigenenergies $E_{i,j}$ and associated eigenfunctions $\Psi_{j,\pm}$ of the Hamiltonian at K valley are

$$E_{j,\pm} = \pm\hbar\omega_B\sqrt{j(j-1)} \text{ and } \Psi_{j,\pm} = \frac{1}{\sqrt{2}}\begin{pmatrix} \psi_j \\ \pm\psi_{j-2} \end{pmatrix}, \qquad j \geq 2. \qquad (2\text{-}11)$$

The $\pm$ signs denote electron (+) and hole (-), respectively. For $j = 0$ and 1,

$$E_0 = E_1 = 0 \text{ and } \quad \Psi_0 = \begin{pmatrix} \psi_0 \\ 0 \end{pmatrix}, \ \Psi_1 = \begin{pmatrix} \psi_1 \\ 0 \end{pmatrix}. \qquad (2\text{-}12)$$

Orbitals Ψ_0 and Ψ_1 are degenerate and both sit at the zero energy level.

In the K' valley, the role of A_1 and B_2 sublattices are switched. π becomes raising operator and π^+ is lowering operator for harmonic oscillator:

$$\pi\psi_j = -\frac{\sqrt{2}i\hbar}{l_B}\sqrt{j+1}\psi_{j+1} \text{ and } \pi^+\psi_j = \frac{\sqrt{2}i\hbar}{l_B}\sqrt{j}\psi_{j-1}. \qquad (2\text{-}13)$$

We can derive the eigenenergies and eigenfunctions as following:

$$E_{j,\pm} = \pm\hbar\omega_B\sqrt{j(j-1)} \text{ and } \Psi_{j,\pm} = \frac{1}{\sqrt{2}}\begin{pmatrix} \psi_{j-2} \\ \pm\psi_j \end{pmatrix} \quad \text{for } j \geq 2;$$

$$(2\text{-}14)$$

$$E_0 = E_1 = 0 \text{ and } \Psi_0 = \begin{pmatrix} 0 \\ \psi_0 \end{pmatrix}, \ \Psi_1 = \begin{pmatrix} 0 \\ \psi_1 \end{pmatrix}.$$

Note that the above equations in this section are only valid at low energy when $j\hbar\omega_B \ll \gamma_1$. For non-zero energy levels, each LL has 4-fold degeneracy due to the 2-fold valley degeneracy and 2-fold spin degeneracy. For the zero energy level, there is an

accidental orbital degeneracy from Ψ_0 and Ψ_1, which results in 8-fold degeneracy. It is noteworthy that in orbitals Ψ_0 and Ψ_1 in K valley, electrons and holes only occupy A_1 sublattice, thus only reside on the top graphene layer. In K' valley, electrons and holes only occupy B_2 sublattice, thus bottom graphene layer. Consequently, valley degeneracy in bilayer graphene is equivalent to sublattice degeneracy and layer degeneracy for the 8-fold degenerate $E = 0$ Landau level.

2.1.5 Competing orders of $E=0$ state in bilayer graphene

As mentioned in the previous section, the $E = 0$ state of bilayer graphene has 8-fold degeneracy (two spins, two valleys, and an accidental 0 and 1 orbital degeneracy). A perpendicular displacement field D can open a D-induced band gap in bilayer graphene, which is linear to D-field up to 800 mV/nm [103-105]. When a perpendicular magnetic field is applied, the energy bands evolve into discrete Landau levels [106-108]. By manipulating the electric and magnetic fields, one can play with the eight closely competing states and obtain a rich phase diagram with field dependent filling sequences and gap energies [105, 106, 108-114]. Studies have shown that the control of these different degrees of freedom is essential for the observation of fractional and even-denominator fractional quantum Hall effect in bilayer graphene [113-116].

To capture the intricate ordering of the $E = 0$ octet in bilayer graphene with a conceptual picture, Li et al. developed an effective energy diagram based on a single-particle-like model (shown in Figure 2-4) [105]. In this empirical model, the valley gap between $|+,0\rangle$ (colored in red) and $|-,1\rangle$ (cyan) takes on the form of $\Delta_V (D, B) = \Delta (D) +$

αB. The exchange-enhanced spin gap takes on the form of Δ_S $(B) = \beta B$. The form and value of the energy splitting between $N = 0$ and $N = 1$ orbitals E_{10} (D, B) are determined experimentally. From large D to small D-field, the $\nu = 0$ gap closes twice, at D^*_h and D^*_l.

State	Energy
$|+1\uparrow\rangle$	$\frac{\Delta_V}{2} + \frac{\Delta_S}{2} + E_{10}$
$|+0\uparrow\rangle$	$\frac{\Delta_V}{2} + \frac{\Delta_S}{2}$
$|+1\downarrow\rangle$	$\frac{\Delta_V}{2} - \frac{\Delta_S}{2} + E_{10}$
$|+0\downarrow\rangle$	$\frac{\Delta_V}{2} - \frac{\Delta_S}{2}$
$|-1\uparrow\rangle$	$-\frac{\Delta_V}{2} + \frac{\Delta_S}{2}$
$|-0\uparrow\rangle$	$-\frac{\Delta_V}{2} + \frac{\Delta_S}{2} - E_{10}$
$|-1\downarrow\rangle$	$-\frac{\Delta_V}{2} - \frac{\Delta_S}{2}$
$|-0\downarrow\rangle$	$-\frac{\Delta_V}{2} - \frac{\Delta_S}{2} - E_{10}$
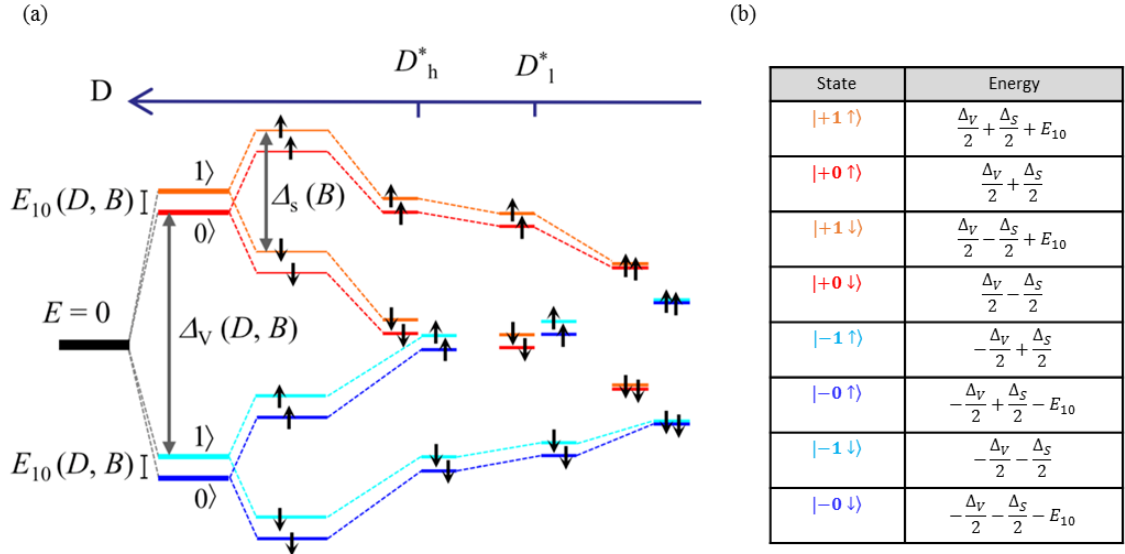
Figure 2-4. Effective Landau level energy diagram for E = 0 octet of bilayer graphene.

(a) An effective Landau level energy diagram for the $E = 0$ octet of bilayer graphene in perpendicular displacement field D and perpendicular magnetic field B [105]. "0/1" denote $N = 0$ and $N = 1$ orbitals, respectively. Arrows, ↑ and ↓, represent the spin polarizations. If we use "+/−" signs to denote states in K/K' valleys, orange, red, cyan, and blue colors denote $|+,1\rangle$, $|+,0\rangle$, $|-,1\rangle$, and $|-,0\rangle$ states, respectively. Δ_V (D, B), Δ_S (B), and E_{10} (D, B) are valley gap, exchange-enhanced spin gap, and energy splitting between $N = 0$ and $N = 1$ orbitals, respectively. D^*_h and D^*_l label the D-field at which the $\nu = 0$ gap closes. (Figure source: Li et al. [105]) (b) Energy levels of the $E = 0$ octet represented in Δ_V (D, B), Δ_S (B), and E_{10} (D, B).
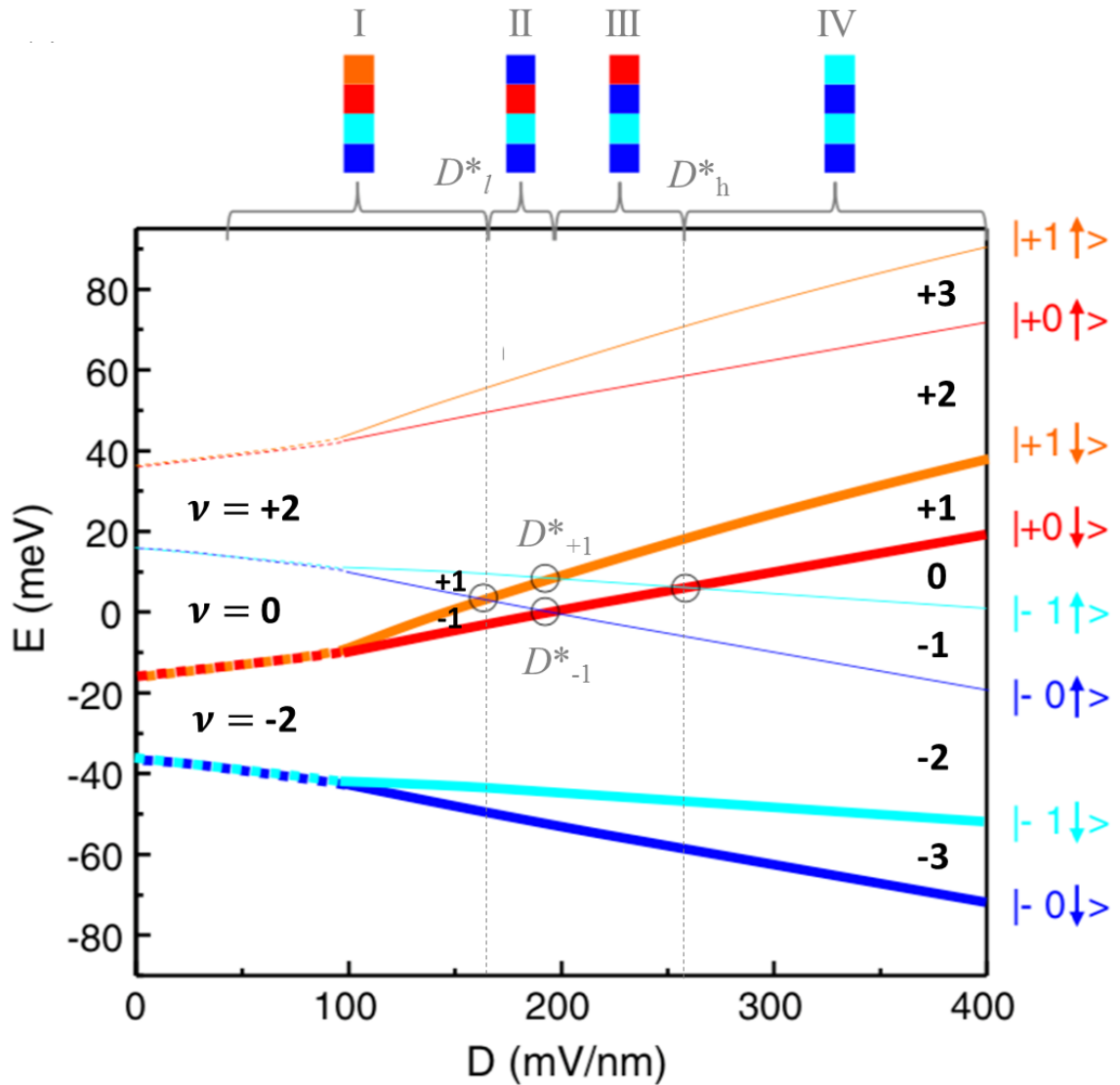
Figure 2-5. D-field dependent effective Landau level energy diagram.
The diagram is calculated for the $E = 0$ octet for magnetic field $B = 31T$. The four coincidence D-fields, D^*_l, D^*_h, D^*_{+1}, and D^*_{-1}, are circled. Black bold numbers denote the corresponding gaps. The color bars indicate the filling sequence from $v = -4$ to $v = 0$ in the four regions I ~ IV. (Figure taken from Li et al. [105])

Figure 2-5 shows how Landau levels evolve with D-field based on the model described before [105]). Gap energies for $v = +1$~$+3$ are the energy difference between

Landau level pairs. Using the energy levels written in the form shown in Figure 2-4(b), gap energies can be represented with the three energy scales: Δ_V, Δ_S, and E_{10} (Table 2-1).

	I: $D^*_{-2} < D < D^*_l$	II: $D^*_l < D < D^*_{\pm1}$	III: $D^*_{\pm1} < D < D^*_h$	IV: $D^*_h < D$
$\nu = +3$	E_{10}	E_{10}	E_{10}	E_{10}
$\nu = +2$	Δ_V	Δ_V	$\Delta_S - E_{10}$	$\Delta_S - E_{10}$
$\nu = +1$	E_{10}	$-(\Delta_V - \Delta_S + E_{10})$	$\Delta_V - \Delta_S + E_{10}$	E_{10}

Table 2-1. Gap energies $\nu = + 1 \sim +3$ of the E = 0 octet represented in Δ_V (D, B), Δ_S (B), and E_{10} (D, B).

2.2 Landau Levels of Bilayer Graphene in a WSe$_2$/Bilayer Graphene van der Waals Heterostructure

2.2.1 Motivation for building a WSe$_2$/bilayer graphene heterostructure

The ability to form close coupling between dissimilar van der Waals materials opens the door to engineer new interactions and device functionalities absent in individual components [11, 117-121]. Through proximity coupling, graphene can become superconducting [122], magnetic [123, 124] or acquire spin orbit coupling (SOC) strength to develop topological band structures or spintronic applications [53-55, 125-129]. Engineering the dielectric environment provides an effective means to control Coulomb interactions and reduce charged impurity scattering [130, 131]. In atomically thin transition metal dichalcogenides, electron-electron interaction-dominated phenomena such as band gap and exciton binding energy are particularly sensitive to dielectric

engineering. There, even the presence of a monolayer graphene capping layer has been shown to cause a significant reduction in the band gap [132, 133].
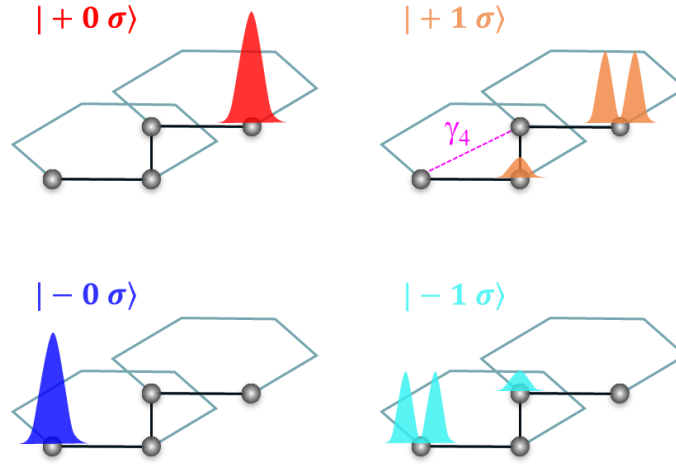
Figure 2-6. Illustration of the wave function $|\xi N\sigma\rangle$ in the E = 0 octet of bilayer graphene. $\xi = +/-$, $N = 0/1$ and $\sigma = \uparrow$ or $\downarrow$ denote the valley (K/K'), orbital and spin indices of the wave function respectively. The interlayer hopping parameter γ_4 connects a dimered site with a non-dimered site.

The $E = 0$ octet ($-4 < \nu < 4$) exhibits a complex Landau level (LL) structure and fascinating quantum Hall ferromagnetism as a result of competing many-body interactions [105, 108, 111-114, 134-139]. A particularly intriguing and challenging aspect of the BLG LLs is E_{10}, the energy splitting between the $N = 0$ and 1 orbital wave functions that are illustrated in Figure 2-6. The $N = 0$ orbitals, labeled as $|\pm 0\rangle$ states occupy the top/bottom layer solely while the $|\pm 1\rangle$ states have a small component occupying the opposite layer. Here, "+/−" signs denote states in K/K' valleys respectively. Each of the four states above has two spin configurations corresponding to $\sigma = \uparrow$ or $\downarrow$. Because of the different wave function distribution of the two orbitals, interlayer potential U [140] and the interlayer Slonczewski-Weiss-McClure (SWM)

hopping parameter γ_4 [141] contribute to E_{10}. Moreover, exchange corrections originating from the filled LLs strongly renormalize the energies of the two levels [108, 134, 142, 143]. The resulting E_{10} is notoriously difficult to calculate but plays an important role in determining the nature of the ground states in the fractional quantum Hall regime [144-146]. Experiments show that E_{10} is small and depends strongly on both the magnetic field B and the perpendicular electric field D but measurements have been incomplete [105, 113, 114, 147]. BLG samples used in these experiments are typically sandwiched between hexagonal Boron Nitride (BN) layers to obtain high quality. Heterostructures incorporating other van der Waals materials have not played a role in studying the LL physics of bilayer graphene.

We have fabricated dual-gated, BN encapsulated WSe_2/BLG heterostructures to explore proximity-induced SOC and the effect of dielectric screening on the LLs of BLG. Remarkably, we found that the presence of even a monolayer WSe_2 sheet has a significant impact on the LL energies of the BLG. The orbital energy splitting $E_{10,}$ which manifests as the LL gap Δ_1 and Δ_3 at filling factors $\nu = 1$ and 3, is significantly enhanced compared to pristine BN encapsulated BLG. Meanwhile, the LL gap Δ_2 at $\nu = 2$ is reduced by approximately two-fold. We performed a systematic study of the D- and B- dependences of $\Delta_{1,2,3}$ and a quantitative comparison to the corresponding energies in pristine BLG. Our results provide fresh experimental insights to understand the interaction-driven LLs in bilayer graphene and offer a potential pathway of tuning quantum Hall physics via van der Waals heterostructures. Extensive measurements on our devices have not uncovered significant proximity-induced SOC. Results are briefly discussed in Section 2.2.4.

2.2.2 Sample preparation and characterization

WSe$_2$/BLG devices are fabricated through a multistep process. BLG flakes are exfoliated from Kish graphite onto a 290 nm SiO$_2$/doped Si wafer coated with poly-propylene carbonate (PPC) and identified optically. The PPC film carrying the BLG flake is then peeled off and placed onto a poly dimethyl siloxane (PDMS) stamp. The standard dry transfer technique [2] is used to transfer the BLG flake to a BN flake already exfoliated onto a SiO$_2$/doped Si wafer. We perform standard e-beam lithography and reactive ion etching to pattern the BLG flake into a Hall bar [7, 148] followed by annealing in Ar/H$_2$ at 450°C for 3 hours to remove the resist residue. A BN/WSe$_2$ stack is then assembled and transferred onto the BLG/BN device to cover half of the Hall bar as shown in Figure 2-7(c). The WSe$_2$ sheet is a monolayer in device #4 and bilayer in devices #2 and #3. Finally, we use e-beam lithography and physical vapor deposition to make Cr/Au top contacts to the exposed BLG terminals and the top gate, which covers the entire rectangular area of the Hall bar. The doped Si serves as the back gate.

A schematic sideview of our devices, a color-enhanced optical micrograph of device #2 and atomic force microscopy images of the central area of two devices are shown in Figure 2-7. In device #2, the area probed in transport measurements (between electrodes 6 and 2) appears mostly flat and bubble-free in the atomic force microscopy image, suggesting a good van der Waals coupling.
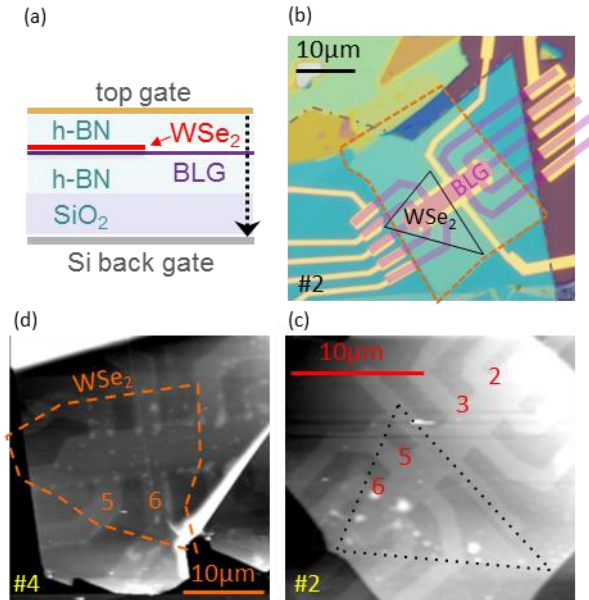
Figure 2-7. Schematic sideview, and images of our BN encapsulated WSe$_2$/BLG devices. (a) Schematic sideview of our BN encapsulated WSe$_2$/BLG devices. The dotted arrow indicates the positive direction of D field. (b) Color-enhanced optical micrograph of device #2. The BLG sheet is shaded in purple. The bilayer WSe$_2$ flake is outlined in black. The orange dashed and gray dash dotted lines trace out the edges of the top and bottom BN sheets respectively. (c) Atomic force microscope image of device #2. The WSe$_2$ sheet is outlined in black dotted lines. R_{xx} measurements use electrodes 5 and 6 on WSe$_2$/BLG and electrodes 2 and 3 on pristine BLG. (d) Atomic force microscope image of device #4, where the BLG is partially covered by a monolayer WSe$_2$ sheet outlined in orange. Compared to device #2, more bubbles formed in the transfer process. R_{xx} measurements use electrodes 5 and 6.
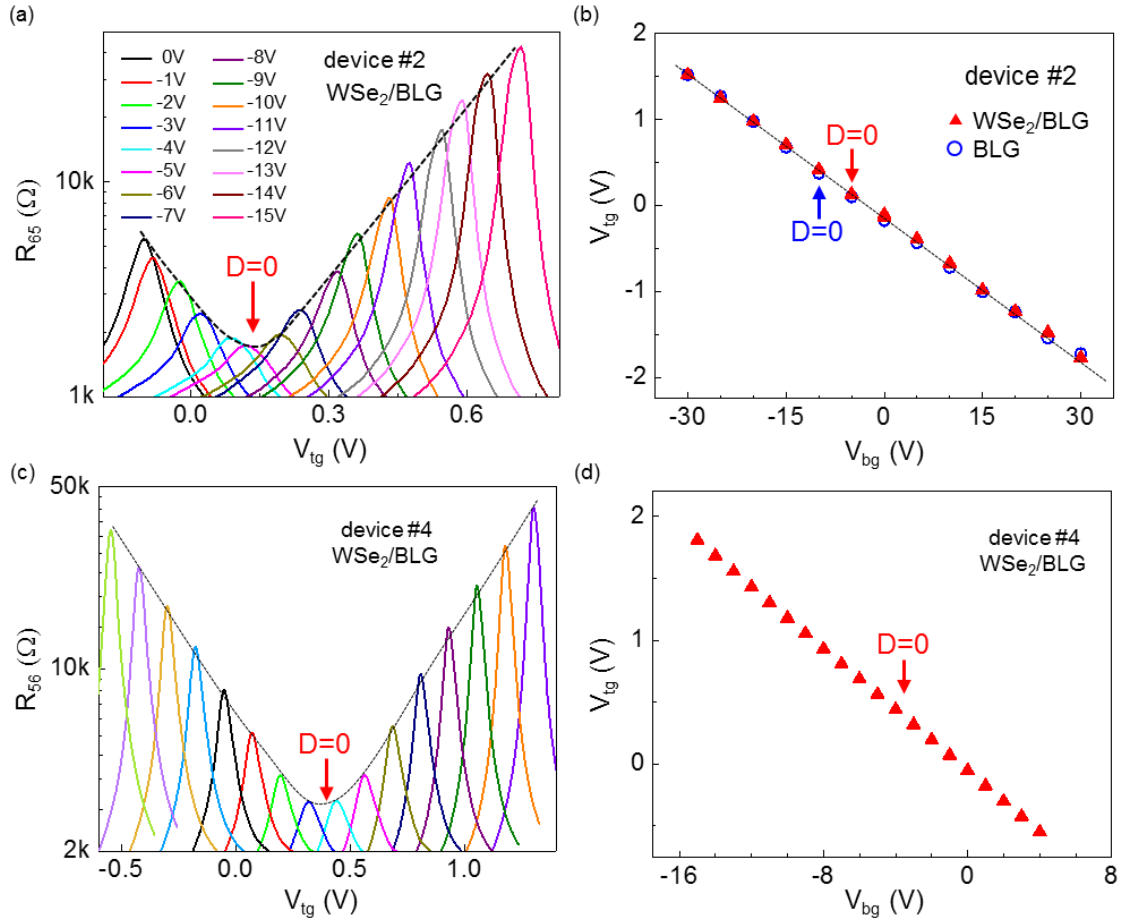
Figure 2-8. Gating characteristics of device #2 and #4.

(a) Resistance vs top gate voltage $R_{65}(V_{tg})$ at fixed Si back gate voltage V_{bg} as labeled in the plot. Data show traces taken on the WSe$_2$/BLG side of device #2. The pristine BLG side looks similar. The black dashed line tracks the CNPs. (b) The V_{tg}-V_{bg} relation of the CNP on both the WSe$_2$/BLG and the pristine BLG sides of device #2 with the $D = 0$ positions marked in the plot. The black dashed line is a guide to the eye. (c) Resistance vs top gate voltage $R_{56}(V_{tg})$ at fixed Si back gate voltage V_{bg}, from 4V (leftmost, lime) to -11V (rightmost, violet) in 1V steps. Traces are taken on the WSe$_2$/BLG side of device #4. The black dashed line tracks the CNP of each curve and the D=0 position. (d) The V_{tg}-V_{bg} relation of the CNP on WSe$_2$/BLG of device #4 with the $D = 0$ positions marked in the plot.

Measurements are performed using standard low-frequency lock-in four-probe configurations on both WSe$_2$-covered (hereby denoted as WSe$_2$/BLG) and uncovered BLG (pristine BLG) regions at varying temperatures down to 20 mK and magnetic fields

up to 18 T. T = 1.6 K unless otherwise mentioned. We use the top and bottom gates to independently control the carrier density n and the electric displacement field D of the BLG [105, 139]. The WSe_2 sheet is not electrically contacted. Figure 2-8(a) plots the resistance vs top gate voltage of the WSe_2/BLG side in device #2 at fixed Si back gate voltages V_{bg} as labeled in the plot. This measurement allows us to track the V_{tg}-V_{bg} gating relation of the charge neutrality point (CNP) and identify the D =0 point as the global minimum of the CNP resistance peak. Figure 2-8(b) plots such gating relation obtained on both the pristine and the WSe_2/BLG side of device #2 and their respective D=0 positions. That fact that both gating relations follow the same slope indicates negligible effect of the WSe_2 on the capacitance of the top gate. This is not surprising given the atomic thickness of the WSe_2 sheets used in our devices. The Fermi level of the system remained inside the band gap of WSe_2 in our experiments. The D = 0 positions on both sides of the device display only a small shift in V_{tg}. This indicates a negligible amount of charge transfer between the WSe_2 and the BLG sheets. The gating characteristics of device #4 are shown in Figure 2-8(c) and (d). Because device #4 does not have pristine BLG side, all data are taken on WSe_2/BLG side, which exhibit similarly high quality as device #2.
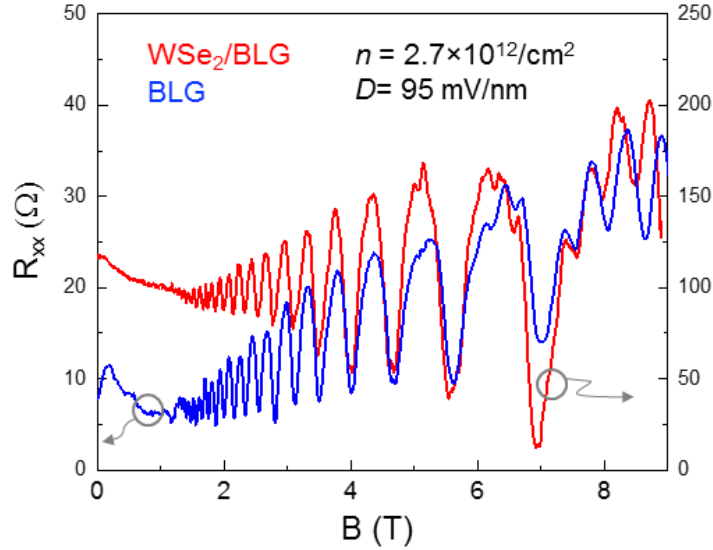
Figure 2-9. Magnetoresistance $R_{xx}(B)$ obtained on the pristine BLG side of device #3 (blue trace, left axis) and the WSe₂/BLG side of device #2 (red trace, right axis). Both devices are set to electron density $n = 2.7 \times 10^{12}$/cm2 and displacement field $D = 95$ mV/nm.

Our WSe₂/BLG devices exhibit field effect mobility of 30,000−50,000 cm²/Vs and well-developed Shubnikov-de Haas oscillations in a magnetic field B. Figure 2-9(a) compares two magnetoresistance traces $R_{xx}(B)$ obtained on the WSe₂/BLG side of device #2 (red trace) and the pristine BLG side of device #3 (blue trace). Both traces are tuned to the same electron density $n = 2.7 \times 10^{12}$/cm² and the same displacement field $D = 95$ mV/nm. Both oscillations start at $B \sim 1.2$ T and are approximately sinusoidal, indicating high, comparable sample quality. A detailed comparison of the $\nu = 2$ gap energy obtained on these two devices is shown in Figure 2-13(a).

2.2.3 A different Landau level energy diagram in WSe₂/bilayer graphene heterostructure

The first prominent effect of the WSe$_2$/BLG heterostructure manifests in the (B, D) phase diagrams of the $\nu = 0$ state, where several phases with different order parameters have been observed in pristine BLG [111, 112, 136, 137, 147, 149]. The blue dashed lines in Figure 2-10(a) plot the phase diagram obtained in Li *et al.* [105] on pristine BN encapsulated devices, where we have labeled the low-*D* canted-antiferromagnetic (CAF) and the high-*D* layer polarized (LP) phases. Phase diagrams obtained by other groups on BN-encapsulated BLG are in excellent agreement with ours [108, 112, 113, 115]. At the phase boundaries labeled as D^*_h and D^*_l (blue dashed lines), the $\nu = 0$ gap closes and $R_{xx}(D)$ exhibits a local minimum. In pristine BLG, an intermediate phase region between D^*_h and D^*_l (gray shaded area in the plot) starts to appear at $B = 12$ T and grows with increasing B and D. As Figure 2-10(c) shows, this phase is expected to be partially polarized in the orbital index N , and its area is directly related to the magnitude of E_{10} [105]. Figure 2-10(b) plots several $R(D)$ traces taken at $\nu = 0$ on the WSe$_2$/BLG side of device #2. Each trace corresponds to a fixed *B*-field. The splitting of D^*_h and D^*_l occurs at $B \sim 4{-}5$ T, much smaller than the onset field in pristine BLG[108, 112, 113, 115]. The resulting phase diagram is plotted in Figure 2-10(a) using red symbols. In this diagram, the intermediate phase occupies an area significantly larger than its counterpart in pristine BLG. Interestingly, the expansion of the intermediate phase comes at purely the expense of the CAF phase while D^*_h, the phase boundary to the LP state, are nearly identical in pristine and WSe$_2$/BLG.
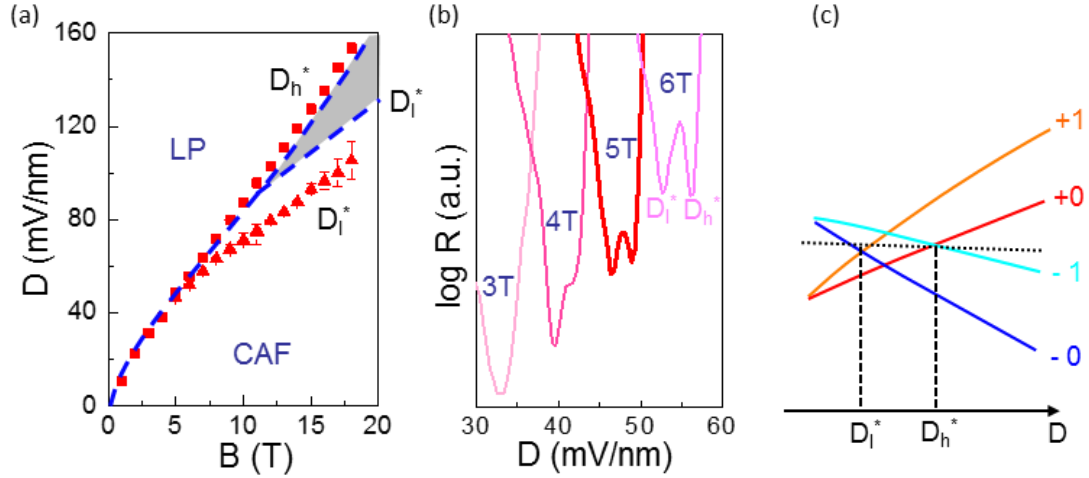
Figure 2-10. The (D, B) phase diagram and $R_{xx}(D)$ plot of the $v = 0$ state.
(a) The (D, B) phase diagram of the $v = 0$ state in BN encapsulated pristine BLG (blue dashed lines, from Li *et al.* [105]), and in WSe$_2$/BLG (red symbols). When D-field and magnetic field are both small, the electron spins from the two different layers of bilayer graphene are anti-aligned and canted to the magnetic field direction (CAF phase). As the D-field increases, there is a phase transition into a layer polarized phase, where both spins occupy one layer. (b) Semi-log $R_{xx}(D)$ of $v = 0$ at selected B-fields from 3 to 6 T as labeled in the plot. D_h^* and D_l^* denote the upper and lower coincidence D-fields respectively. (c) Schematic diagram of the LLs near the coincidence points. The black dotted line represents the Fermi level of $v = 0$. From device #2. $T = 20$ mK.

To further examine the influence of the WSe$_2$ on the LLs of BLG, we measure directly the LL gap energy $\Delta_{1,2,3}$ at $v = 1$, 2 and 3 using the temperature dependence of the magnetoresistance $R_{xx}(T)$. The gaps were measured at a constant D-field unless stated otherwise. The constant D-field is achieved by sweeping the top and Si back gate simultaneously, following the $V_{bg} - V_{tg}$ relation shown in the R_{xx} map (Figure 2-11).
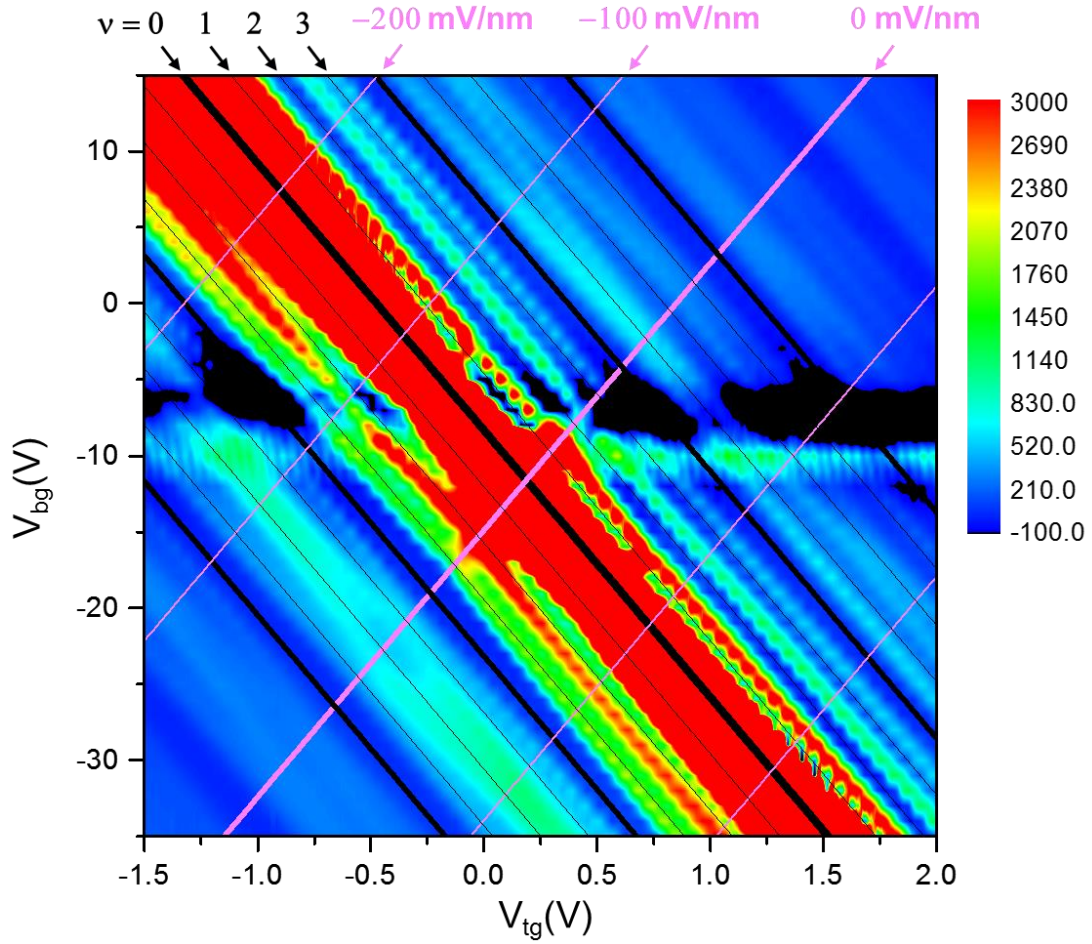
Figure 2-11. R_{xx} map at magnetic field 8.9 T and temperature 1.65 K.
Data are obtained on WSe$_2$/BLG side of device #2. The color scale of resistance (unit: Ω) is shown on the right. To have a larger color contrast near integer filling factors, the minimum resistance of the color scale is chosen to be negative. Solid black lines track constant filling factor $v = -8 \sim 8$ with increment 1, where $v = -8, -4, 0, 4, 8$ are tracked with thicker lines. $v = 0 \sim 3$ are labeled. Solid pink lines follow constant D-field = −200, -100, 0, 100, 200 mV/nm. Device has a bad contact in the region of $V_{bg} = -13 \sim -4$V.

Figure 2-12(a) shows a set of $R_{xx}(n)$ sweeps that span $v = 1$, 2, and 3 at selected temperatures ranging 3−20 K. Here $D = 100$ mV/nm and $B = 8.9$ T. Figure 2-12(b) shows the Arrhenius plots for the three filling factors and the corresponding fits to $R_{xx} \propto \exp(-\frac{\Delta}{2k_BT})$, where $\Delta_{1,2,3} = 1.6$, 4.3 and 1.6 meV respectively from the fits. We chose the temperature range where the background of R_{xx} remains constant (indicated by bundle points on either side of the integer fillings). The fits are well behaved and insensitive to the exact V_{tg} choice of the analysis. Similar measurements are repeated at other magnetic and displacement fields.

(a)

ν=1

10k

ν=2

ν=3

$R_{xx}(\Omega)$

1k

B=8.9 T
D=100 mV/nm

100

0.8   0.9   1.0

$V_{tg}(V)$

—— 3K	—— 6.5K
—— 4K	—— 7K
—— 4.7K	—— 8K
—— 5.5K	—— 10K
—— 6K	—— 20K

(b)

9

8

$\ln R_{xx}$

7

ν=1

6

ν=3

5

ν=2

0.1   0.2   0.3

1/T (1/K)
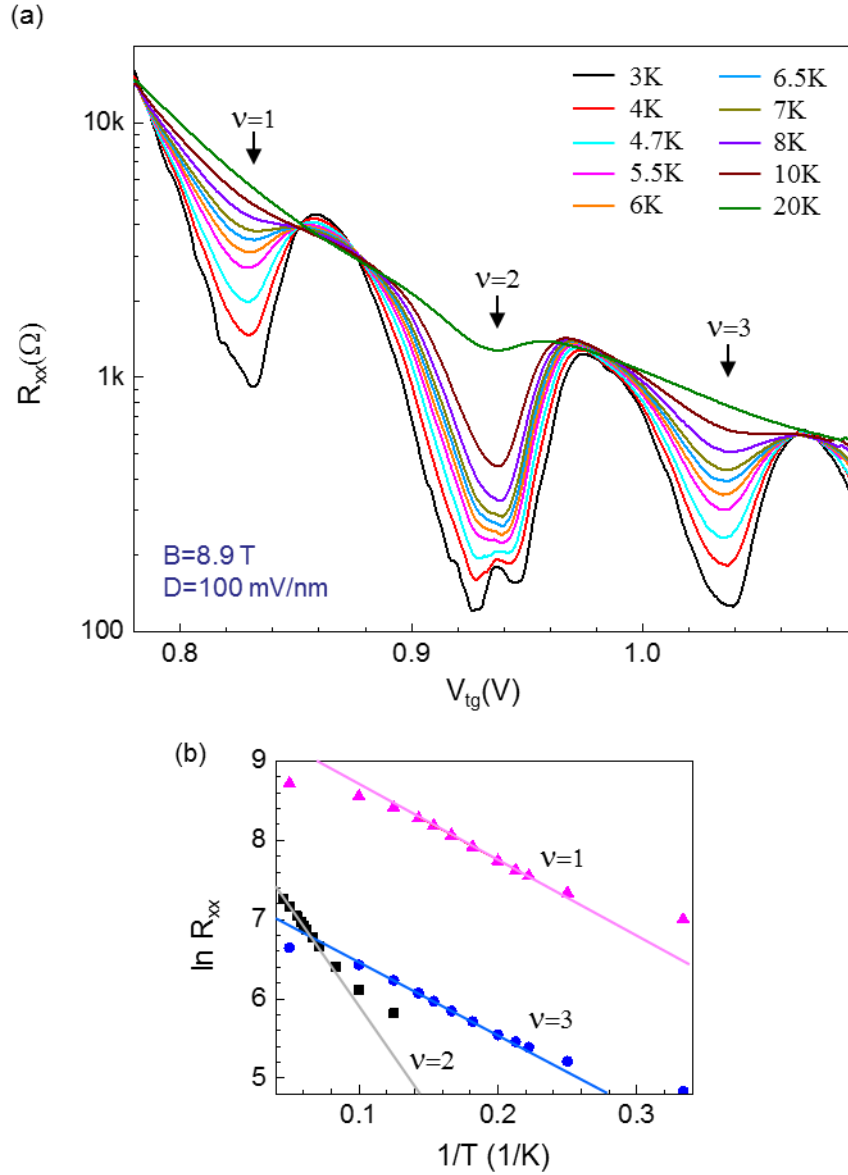
Figure 2-12. $R_{xx}(V_{tg})$ at selected temperatures and Arrhenius plot of $R_{xx}(T)$ at $\nu = 1,2,3$ gaps.

(a) $R_{xx}(V_{tg})$ at selected temperatures as labeled in the plot. V_{bg} was swept simultaneously to follow a line of constant $D = 100$ mV/nm. $B = 8.9$ T. The arrows point to filling factors $\nu = 1, 2,$ and 3 respectively. (b) Arrhenius plot of $R_{xx}(T)$ at $\nu = 1$ (magenta), 2 (black), and 3 (blue). Fits to the data (solid lines) yield gap energies $\Delta_1 = 1.6$ meV, $\Delta_2 = 4.3$ meV and $\Delta_3 = 1.6$ meV respectively. From device #2.

Figure 2-13(a) plots the B-dependence of $\Delta_{1,2,3}$ on the WSe$_2$/BLG side of device #2, together with Δ_2 on the pristine side of device #3 (black stars) and Δ_2 reported in the literature (shaded areas). Our Δ_2 (B) measurements yield a slope of 0.6 meV/Tesla for WSe$_2$/BLG (purple dashed line) and 1.4 meV/Tesla for pristine BLG (black line). This comparison offers strong evidence that the gap of $\nu = 2$ is significantly reduced in WSe$_2$/BLG. Results of Δ_2 (B) reported in the literature exhibit larger spread due to quality variations and the lack of control in the D-field. Nonetheless, they are consistent with the results of our pristine BLG in slope and magnitude and are all significantly larger than Δ_2 of our WSe$_2$/BLG devices. In contrast to the behavior of Δ_2, $\Delta_{1,3}$ in WSe$_2$/BLG (inset of Figure 2-13(a)) becomes measurable at $B \sim 6$ T and are considerably *larger* than values reported for pristine BLG [113, 114, 147]. The increase of $\Delta_{1,3}$ is consistent with the large splitting of D^*_h and D^*_l shown in Figure 2-10(b); both reflect the enhancement of E_{10} in WSe$_2$/BLG samples.
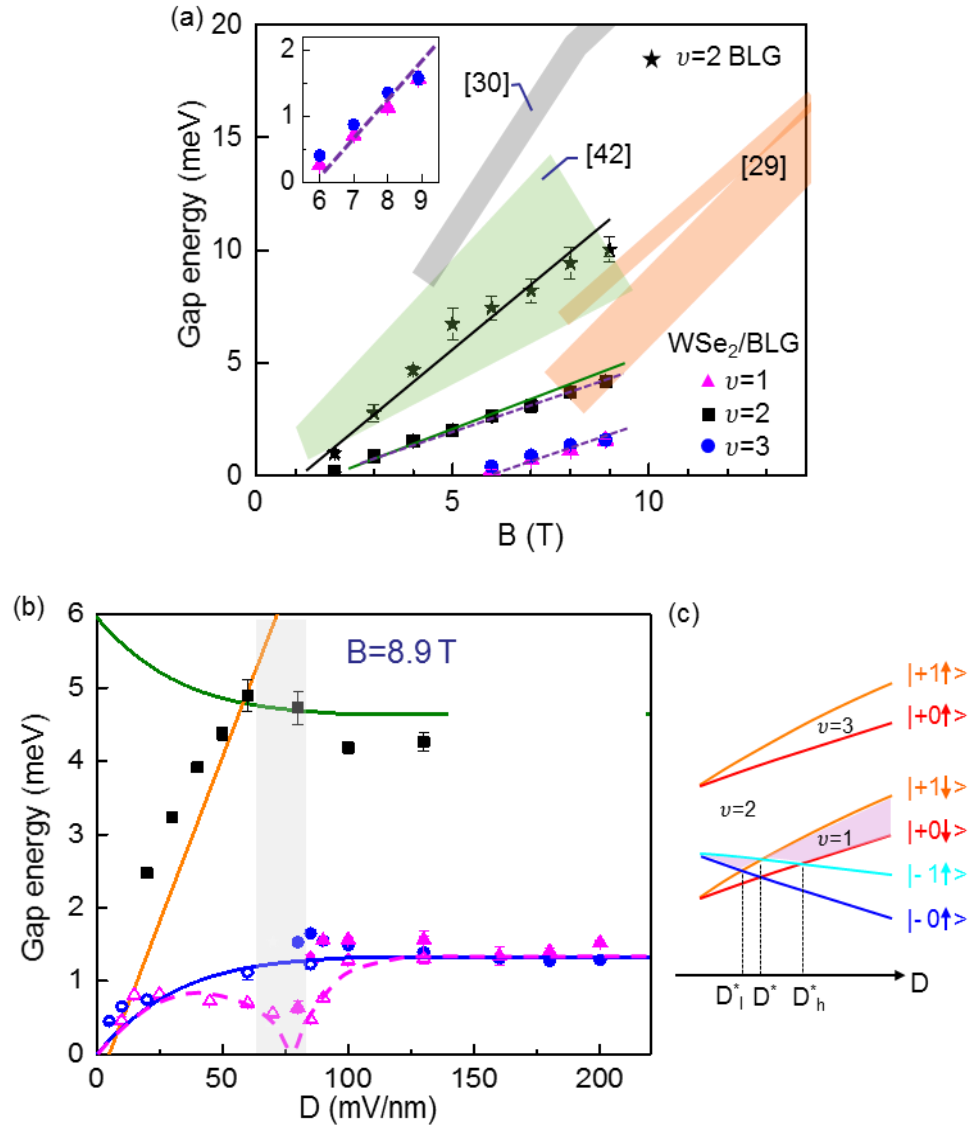
Figure 2-13. The magnetic field and *D*-field dependence of $\Delta_{1,2,3}$.

(a) The magnetic field dependence of $\Delta_{1,2,3}$ at $v = 1$ (magenta triangles), 2 (black squares), and 3 (blue circles) on WSe₂/BLG of device #2 and Δ_2 at $v = 2$ (black stars) on pristine BLG of device #3. The purple dashed lines have the slope of 0.6 meV/Tesla. The black solid line 1.4 meV/Tesla. The dark olive line plots $\Delta_2(B) = 0.67B - 1.32$. Inset: a magnified view of $\Delta_{1,3}$. $D = 100$ mV/nm for all measurements. Shaded areas represent Δ_2 reported in the literature (gray for [114], light green for [147], peach for [113]). (b) The *D*-field dependence of $\Delta_{1,2,3}$. $B = 8.9$ T. Symbols follow (a). Solid/open data points are

obtained from density/D-field sweeps respectively. The solid orange line plots Δ_v (meV) = 0.09D (mV/nm) − 0.05B (Tesla). The solid dark olive line plots 0.67B − $E_{10}(D)$, where B = 8.9 T and $E_{10}(D)$ is given by the blue solid line with an empirical function of $E_{10}(D)$ = $4.1 \times 10^{-2}D - 4.9 \times 10^{-4}D^2 + 2.7 \times 10^{-6}D^3 - 5.6 \times 10^{-9}D^4$ for D < 100 mV/nm and E_{10} = 1.3 meV for D > 100 mV/nm. The magenta dashed line is a guide to the eye for the v = 1 gap. (c) LLs near the coincidence points. The v = 1 gap (shaded in pink) closes at D^*.

Figure 2-13(b) plots the D-dependence of $\Delta_{1,2,3}$ on the WSe$_2$/BLG side of device #2 at a fixed B = 8.9 T. Measurements of this kind are lacking in pristine BLG. Δ_3 (open and solid blue symbols) exhibits a rapid rise with increasing D then saturates at approximately $D^* \sim$ 75 mV/nm to a magnitude of 1.3 meV. In comparison, both Δ_2 (black symbols) and Δ_1 (magenta symbols) are non-monotonic in D, with Δ_2 showing a maximum and Δ_1 showing a significant dip in the vicinity of D^*. These complex trends can in fact be well captured by an effective LL energy diagram Li *et al.* developed for pristine BLG [105]. Figure 2-13(c) illustrates the order and crossings of the LLs in the vicinity of D^*_h, D^*, and D^*_l. Several features of the model, i.e. the simultaneous maxing of Δ_2 and vanishing of Δ_1 at D^*, the equal magnitude of Δ_1 and Δ_3 at $D > D^*_h$, and the monotonic D-dependence of $\Delta_3 = E_{10}$ are validated by our measurements. We conclude that LLs in WSe$_2$/BLG follow the same basic structure as in pristine BLG.

We fit the measurements of $\Delta_{1,2,3}$ obtained here to the effective model described in Li *et al.* [105] to examine the quantitative difference of the two systems. The fitting results are plotted as orange, dark olive and blue solid lines in Figure 2-13(b). The overall agreement with data is very good. The blue line plots a polynomial fit to $E_{10}(D) = \Delta_3(D)$, the salient feature of which is the saturation of Δ_3 at $D > D^*$. The orange line plots Δ_2

(meV) = 0.09D (mV/nm) − 0.05B (Tesla), which represents the gap of $v = 2$ in the regime of $D < D^*$. In this regime, Δ_2 is a valley splitting as Figure 2-13(c) shows and is primarily given by the size of the D-field induced band gap of BLG. The coefficient 0.09 is determined from independent band gap measurements at $B = 0$ in this device using methods similar to that described in the Supplementary material of Ref. [105]. The dark olive line plots Δ_2 (meV) = 0.67B (Tesla) − $E_{10}(D)$, which fits the gap of $v = 2$ in the regime of $D > D^*$. In Figure 2-13(b), $B = 8.9$ T. Using the same expression of Δ_2 and setting $D = 100$ mV/nm, we obtain $\Delta_2(B) = 0.67B − 1.3$. This equation is plotted as a dark olive line in Figure 2-13(a) and also provides an excellent description of the measurements there. Consistency checks such as this show the effective model captures data really well. As Figure 2-13(c) shows, Δ_2 in the regime of $D > D^*$ is mostly an exchange-enhanced Zeeman gap, with the size of the spin splitting given by the linear term $\Delta_s = 0.67B$. Here the coefficient 0.67 is significantly smaller than $\Delta_s = 1.7B$ obtained for pristine BLG in Ref. [105], indicating a much weaker exchange effect at $v = 2$ in WSe$_2$/BLG. This is opposite to the situation of E_{10}, which is significantly enhanced in WSe$_2$/BLG.

Figure 2-14(a)-(c) compare the measured LL gap energies $\Delta_{1,2,3}$ in device #2 and #4 as a function of D- and B-fields. In all three figures, device #4 displays trends similar to device #2 but with consistently smaller gap values. Since the gaps at $v = 1, 2, 3$ are all sensitive to exchange effects, larger density inhomogeneity generated by the bubbles in #4 may have caused a reduction in the gap energies. Despite a stronger disorder, Figure 2-14(d) shows that in device #4 signs of splitting between D^*_h and D^*_l of the $v = 0$ state appear at $B = 6$ T whereas even in very high quality pristine BLG samples, the splitting

does not occur until $B \sim 12$ T [105, 108]. This observation supports the enhancement of E_{10} in device #4 also, which likely comes from modified Coulomb interactions.
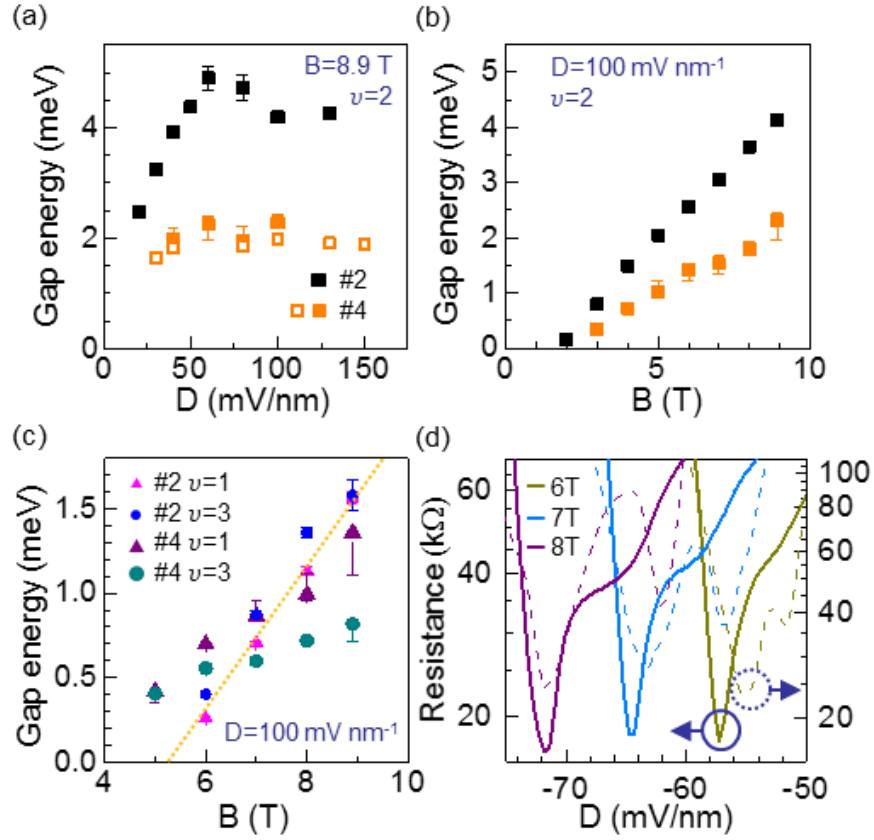
Figure 2-14. The Landau level gap energies $\Delta_{1,2,3}$ measured in devices #2 and 4.
(a) D-field dependence. (b, c) B-field dependence. (d) Comparison of log $R_{xx}(D)$ at $v = 0$ in devices #4 (solid traces, left axis) and #2 (dashed traces, right axis). In device #4, prominent shoulders that suggest the appearance of D^{*}_{l} are observed near places where clear splittings of D^{*}_{h} and D^{*}_{l} are seen in device #2.

2.2.4 Absence of proximity-induced spin orbit coupling signatures

An original goal of our study is to examine the experimental signatures of spin orbit coupling (SOC) in BLG, introduced through proximity coupling to a TMD material with large SOC strength such as WSe_2 or WS_2 [53-55]. Previous experiments have indeed identified the signatures of proximity-induced SOC in the splitting of the bands– manifesting as a beating pattern in the Shubnikov-de Haas (SdH) oscillations– and weak antilocalization [53, 54]. The magnitude of the induced SOC is found to be of order 10 meV. Guided by band structure calculations [55] and previous experiments [53, 54] , We have carefully looked for these signatures in our devices over a wide range of carrier type and density and at varying D-fields, with parallel studies performed on the pristine BLG region of the devices. We have not observed evidence that points to significant proximity-induced SOC. At very low magnetic field, our devices exhibit weak localization signals consistent with BLG behavior in our devices and reported previously [150]. No weak antilocalization was found. No clear beating pattern was present in the SdH oscillations of our devices. Figure 2-15(a) shows a few examples in device #2 at hole carrier density $n_h = 3.5 - 4 \times 10^{12}/cm^2$ and selected D-fields from −200 mV/nm to +200 mV/nm. For comparison, we also show the illustrated band structure evolution calculated by Gmitra *et al.* [55]. The SdH oscillations in all four panels are similar to one another, without clear signs of beating. These observations point to a very small, if any, induced SOC in our devices.
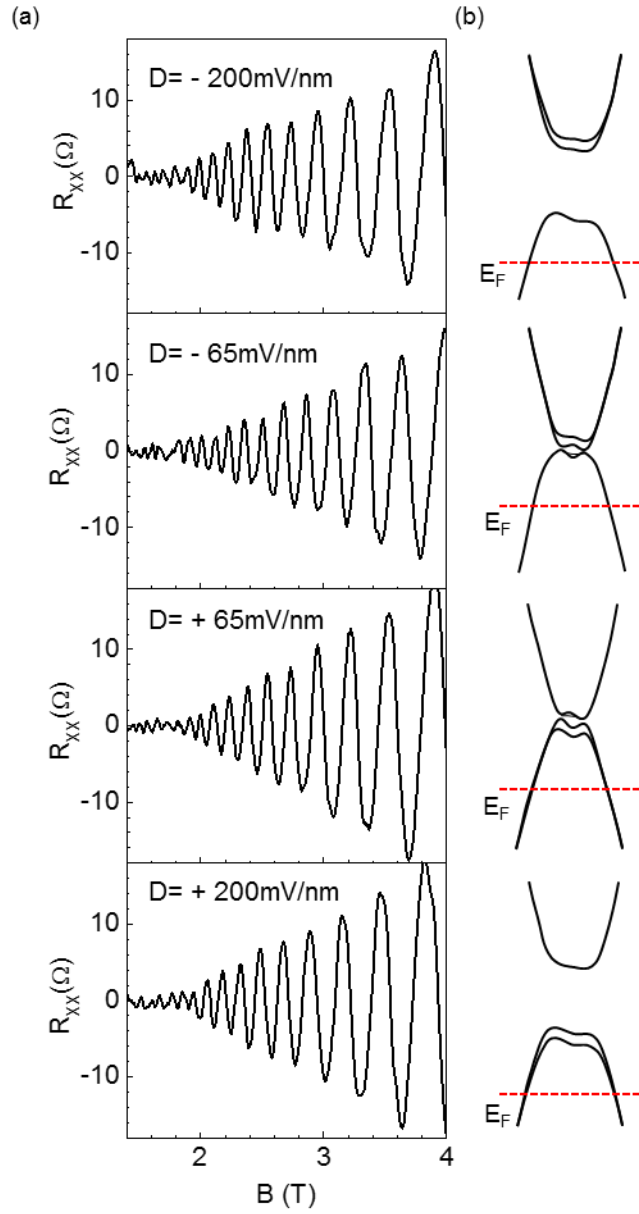
Figure 2-15. Magnetoresistance oscillations and expected evolution of the band structure.

(a) Magnetoresistance oscillations at hole density $3.5 - 4 \times 10^{12}$ /cm^2 and $D = -200$ mV/nm, -65 mV/nm, $+65$ mV/nm, and $+200$ mV/nm as labeled in the plots. A slowly varying background has been removed from each trace. The positive direction of the D-field points from the WSe$_2$ to the BLG to follow the definition used by Gmitra et $al.$ [55]. We calculate D following the convention of the field. (b) illustrates the expected evolution of the band structure. Beating is expected for the bottom two panels band but not for the top two panels because the Fermi level E_F is in the valence band.

We suspect that the discrepancy arises from the different sample preparation processes used. Devices used by Wang *et al.* [53, 54] have the stacking order of graphene/TMD/SiO$_2$. The stack was "ironed" with an atomic force microscope tip scanning in contact mode to remove contaminations [54]. This process could have also pushed graphene closer to the TMD sheet. In our fabrication process, the van der Waals coupling of WSe$_2$ to the BLG is made at the last transfer step, before which the WSe$_2$ and the BLG flakes are coupled to two separate BN sheets. In a recent work, Yang *et al.* [129] showed that the immediate vicinity to a BN sheet draws the graphene slightly away from the TMD and this distance increase, though only a small fraction of an Angstrom, can have a dramatic effect on the proximity-induced SOC strength. The absence of an observable SOC here is perhaps related to a larger WSe$_2$-BLG distance in our devices caused by the fabrication process we used. This is a hypothesis that needs to be further examined.

2.2.5 Discussion and conclusion

It is remarkable that close vicinity to an atomically thin sheet of WSe$_2$ can lead to such large and contrasting changes of the LL gaps in BLG. It is possible that the dielectric screening of the WSe$_2$ sheet plays a role. However, unlike a thick BN dielectric layer used in existing BN encapsulated devices, here the WSe$_2$ sheet is less than 1 nm in thickness so it primarily impacts the short-range components of the Coulomb interaction. Indeed, the physics of the $E = 0$ octet in BLG is well known to be sensitive to interactions at the lattice scale [136, 137], where the presence of the WSe$_2$ sheet may well have an impact. The modified phase diagram of $v = 0$ we obtained in Figure 2-10(b) supports this

hypothesis. At finite fillings, both the enhanced Zeeman gap at $\nu = 2$ and the orbital splitting E_{10} arise from exchange effects. How they are modified in the presence of a thin WSe$_2$ layer requires more in-depth calculations to understand. In addition to screening, we have considered the effect of twist alignment between the two lattices. Because the WSe$_2$ lattice is 34% larger than that of graphene, the Moiré pattern formed between the two has a wavelength of less than 1 nm for any given twist angle [151]. Guided by optical images of the devices, we produced various alignment scenarios between the selenium sublattice of WSe$_2$ and the carbon sublattice of BLG. All show the majority of the Se and C atoms do not directly overlap. Thus, direct on-site interactions could not have been significant in our devices. Further, the magnitude of the interlayer hopping term γ_4 is important to the size of E_{10}. Whether γ_4 is altered by the presence of the WSe$_2$ sheet requires calculations to clarify. We hope that the comprehensive and high-quality data we obtained on the LL energy gaps motivate future calculations and experiments to answer these open questions and by doing so shed more light on the complex many-body effects in BLG and van der Waals heterostructures in general.

In conclusion, we have performed a systematic study of the LL energy gaps at filling factors $\nu = 1$, 2 and 3 in WSe$_2$/bilayer graphene heterostructures. It is remarkable that the presence of an atomically thin WSe$_2$ sheet can give rise to such a significantly enhanced $N = 0$ and 1 orbital splitting E_{10} and a significantly reduced exchange Zeeman gap at $\nu = 2$. These measurements provide fresh input to understand interaction-driven quantum Hall phenomena in bilayer graphene and point to the use of van der Waals heterostructures as an effective knob to tune the strength of the interactions.

Chapter 3

Toward Better Electrical Contact to Few-Layer GaSe

The study of magnetism in 2D layered materials can potentially contribute to both fundamental knowledge and technological applications. 2D magnetism may be able to integrate information processing and storage and thus is a candidate for next-generation electronics. There may be several approaches towards the synthesis of 2D magnetic materials. Before 2D magnetism was firstly realized in CrI_3 and $Cr_2Ge_2Te_6$ [68, 81], Cao et al. predicted that GaSe, a semiconducting 2D material, can have a carrier-density-dependent ferromagnetism originating from Stoner mechanism [18]. Such carrier-density driven phase transition can have significant technological consequences since carrier density in a semiconductor can be controlled by a gate. Therefore GaSe offers another possibility to achieve 2D magnetism and such gate tunability is desirable for easy integration of magnetism into electronic devices. In this chapter, we will begin with lattice and electronic structures of GaSe and what unique electronic band structure it has to possibly achieve such gate-tunable magnetism. Then I will talk about our approaches of fabricating GaSe devices, including passivation of GaSe flake and our efforts in making electrical contact to few-layer GaSe.

3.1 Introduction to GaSe and Stoner Mechanism of Magnetic Instability

Bulk GaSe is a semiconductor with van der Waals bondings between layers [19]. Figure 3-1 shows the crystal structure of GaSe and its bonding type. Each layer is composed of a Se-Ga-Ga-Se tetralayer, in which the bondings are mainly covalent with

some ionic contribution [14]. There are several polytypes of GaSe. β, ε and γ polytypes are studied most (shown in Figure 3-2). Both β and ε polytypes have a 2H stacking sequence (hexagonal symmetry) [152]. They have a similar band structure due to the fact that they have similar lattice constants: a=3.755Å and c=15.94Å for β polytype, and a=3.755Å and c=15.95Å for ε polytype [152]. γ polytype has a 3R stacking sequence (rhombohedral symmetry) with lattice constant h = 23.92 Å [19].

Micron to tens of micron large few-layer GaSe can be grown by several growth methods on different substrates. For example, it can be synthesized by chemical vapor deposition on SiO_2/Si substrate [17], by molecular beam epitaxy on GaAs(111)B [153], and by van der Waals epitaxy on graphene [154] and mica [20].
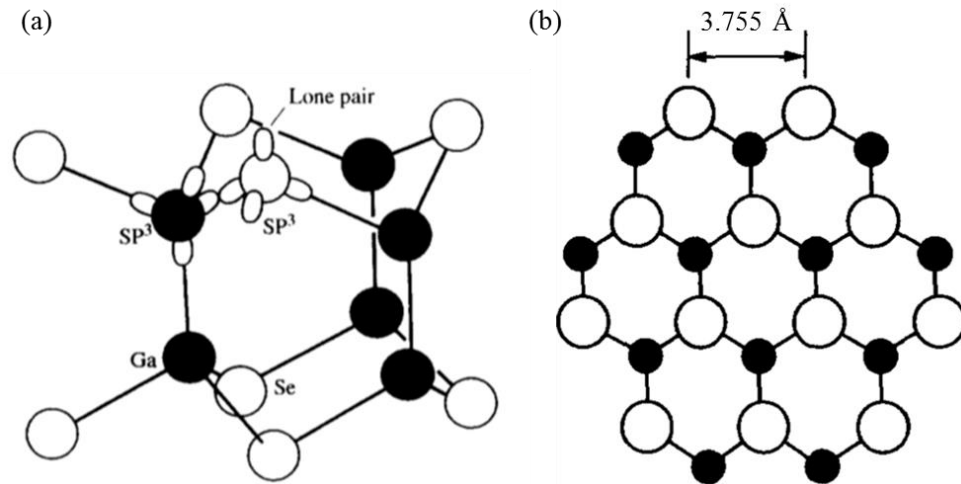
Figure 3-1. Atomic configuration of monolayer GaSe.
Solid and open circles are Ga and Se atoms, respectively. (a) Each Ga atom bonds with 3 Se atoms and 1 Ga atom. Each Se atom bonds with 3 Ga atoms. GaSe has 9 valence electrons: 4 electrons are accommodated by 4 sp^3 hybrid orbitals of a Ga atom, 3 electrons are in 3 sp^3 hybrid orbitals of a Se atom, and 2 electrons are in 1 sp^3 hybrid orbital of a Se atom as a lone pair [155]. (Image taken from Tambo et al. [156]). (b) Top view of monolayer GaSe. The lattice constant a is 3.755 Å. (Image taken from K. Ueno et al. [157]).
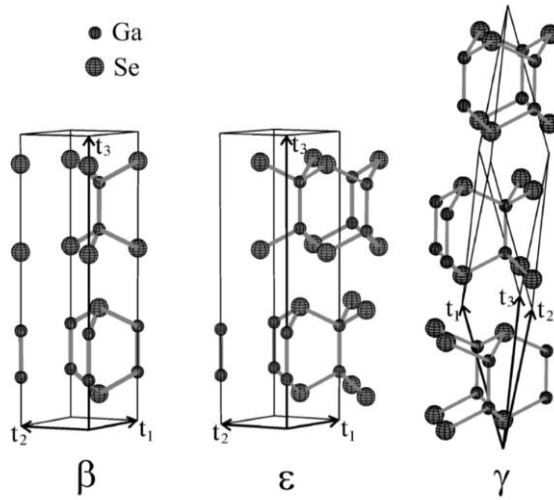
Figure 3-2. Crystal structures of three polytypes of GaSe that are most studied.

t_1, t_2, and t_3 are primitive vectors. Both β and ε polytypes have a hexagonal structure and their band structures are very similar [152]. The γ polytype has a rhombohedral structure. All of the three GaSe structures have a lattice spacing of a = 3.755 Å. Image taken from L. Plucinski et al. [152].

Band structure of GaSe

Bulk GaSe has a direct band gap at Γ point. As the number of layers decreases below 7 layers (7L), the conduction band minimum remains at the Brillouin zone center (Γ), but the energy of highest occupied states at Γ is suppressed and the valence band maximum (VBM) shifts progressively away from Γ symmetrically [17] (see Figure 3-3). Such unique VBM is confirmed in GaSe monolayer by angle-resolved photoemission spectroscopy (ARPES) [21] and in bilayer by photoemission electron momentum microscopy (k-PEEM) [153]. Thus there is a direct-to-indirect band gap transition at 7L and a Mexican-hat-like valence band landscape forms. At the monolayer limit, the energy difference between VBM and the highest occupied states at Γ is largest and the Mexican-

hat-like landscape extends across a large fraction of the Brillouin zone [17, 18]. Figure 3-3(c) shows the thickness dependence of band gap energy calculated by Li et al. [17], which is confirmed experimentally [21].

In the first-principle calculations carried out by Cao et al., hole doping induces ferromagnetic phase transition and half-metallicity in monolayer GaSe (shown in Figure 3-4 [18]). The origin of the predicted ferromagnetic phase transition is Stoner instability facilitated by the unique band structure of few-layer GaSe.
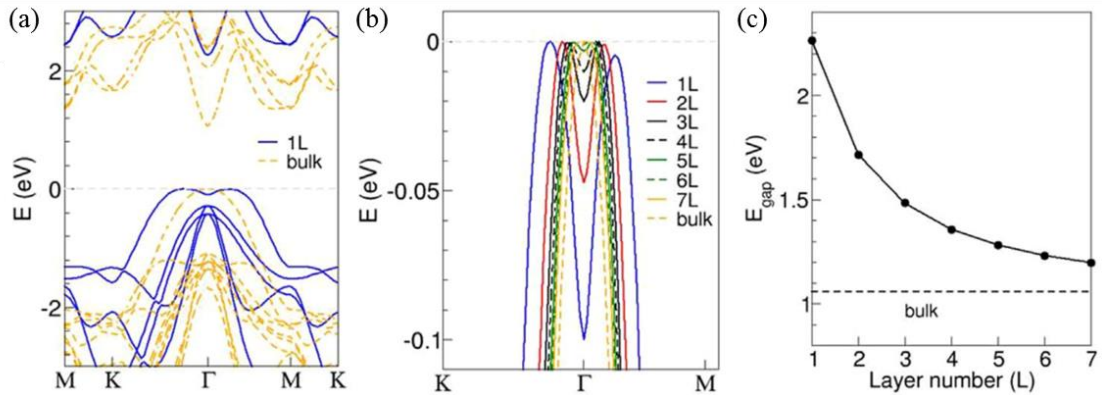
Figure 3-3. Electronic band structures of ε-type GaSe from first-principle calculation. (a) Energy bands of monolayer (blue solid line) and bulk (yellow dashed line) GaSe. (b) Energy bands near the valence band maximum at different layer numbers. (c) Layer number dependence of band gap energy. The dashed line marks the band gap energy of bulk GaSe. The band gap increases by more than 1 eV from bulk material to monolayer limit. Note that the theoretically calculated band gap is about 1 eV smaller than the experimentally determined band gap [21]. (Figures taken from Li et al. [17].)
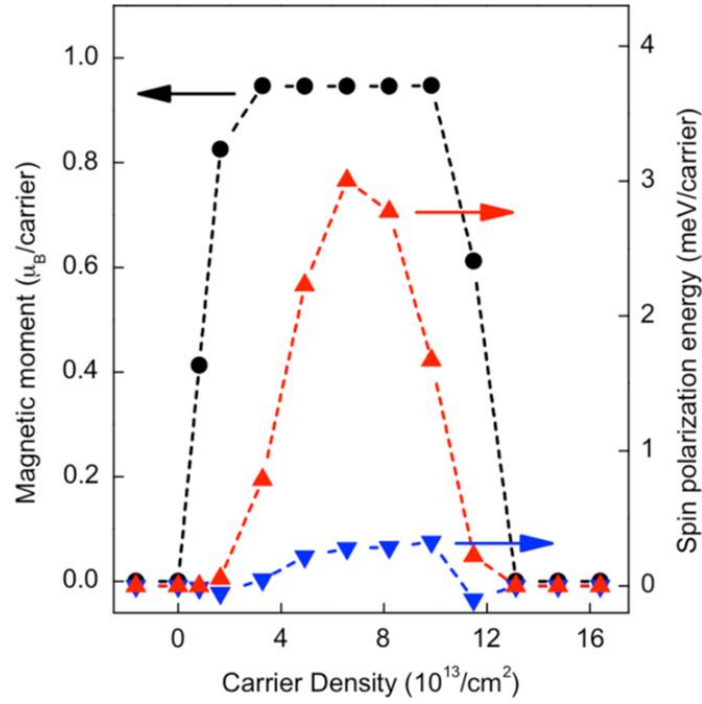
Figure 3-4. Calculated carrier density dependence of ferromagnetism in GaSe.
Black circles and red triangles denote the magnetic moment per carrier and spin polarization energy per carrier, respectively. Both are calculated for the out-of–plane spin-polarized ferromagnetic state. Blue inverted triangles denote the magnetic anisotropy energy, defined as the difference between the states with out-of-plane and in-plane spin polarization. Positive carrier density denotes the density of holes. (Figure taken from Cao et al. [18].)

Stoner theory states that a large density of state near Fermi level can lead to Stoner instability and possible ferromagnetism. Let's do a short derivation of such result with a mean-field method [158]. Consider the case that electrons are not localized (itinerant electrons). For simplicity, consider the limit of good screening, in which electron interactions can be approximated by an on-site interaction between opposite spins. The starting Hamiltonian would be

$$H = \sum_{k\sigma} \epsilon_k a_{k\sigma}^\dagger a_{k\sigma} + \frac{U}{2} \int d^3 r a_\sigma^\dagger(r) a_{\sigma'}^\dagger(r) a_{\sigma'}(r) a_\sigma(r), \qquad (3\text{-}1)$$

where k and σ denote momentum and spin, respectively. The first term is kinetic energy and the second term is potential energy. Because the on-site interaction only happens between opposite spins, the second term of the above Hamiltonian becomes [158]

$$H_{int} = U \int d^3r n_\uparrow(r) n_\downarrow(r)$$

(3-2)

$$= \frac{U}{4} \int d^3r [(n_\uparrow(r) + n_\downarrow(r))^2 - (n_\uparrow(r) - n_\downarrow(r))^2].$$

where $n_\uparrow$ and $n_\downarrow$ are the density of spin-up and spin-down electrons at position r, respectively [158]. Making use of mean-field theory and assuming an order parameter m (magnetization): $m = \frac{1}{2}\langle n_\uparrow - n_\downarrow \rangle = \frac{1}{2V} \int d^3r (n_\uparrow(r) - n_\downarrow(r))$, where V is the volume of the system. The Hamiltonian can then be rewritten as

$$H = \sum_{k\sigma} (\epsilon_k - \sigma m U) a_{k\sigma}^\dagger a_{k\sigma} + VUm^2.$$

(3-3)

In order to have m to be non-zero, the chemical potential difference δ between spin up and down needs to be non-zero. m and δ can be related by the following self-consistent equation

$$m = \rho(\epsilon_F)\delta.$$

(3-4)

The total energy of the system per unit volume can be shown to have the form [158]

$$\frac{E}{V} \cong 2 \int_0^{\epsilon_F} d\epsilon \, \epsilon \rho(\epsilon) + \frac{m^2}{\rho(\epsilon_F)} - Um^2.$$

(3-5)

The first term of the above equation is a constant. The last two terms are competing: $\frac{m^2}{\rho(\epsilon_F)}$ favors smaller m^2 while $-Um^2$ favors larger m^2. The condition for spontaneous development of magnetism, in which the $m = 0$ state becomes unstable and is replaced by

the $m \neq 0$ state, is that $U\rho(\epsilon_F) > 1$. The instability is called Stoner instability. In other words, a large density of state near Fermi level can result in Stoner instability and possible ferromagnetism.

First-principle calculations show that monolayer GaSe has an inverted-Mexican-hat-like valence band top (shown in Figure 3-3 and (a)). Such valence band top leads to a one-dimensional-like singularities in the density of states, i.e. van Hove singularities. Figure 3-5(b) plots the total and partial density of states (DOS) near VBM. A Mexican-hat-like dispersion in two dimensions should lead to the divergence of DOS at VBM, which resembles the band edge of one dimension (illustrated in Figure 3-5(c) and (d)). However, because the anisotropic dispersion and the spin-orbit splitting break the cylindrical symmetry of the bands, the DOS is modified and peaks around 0.013 eV below the VBM instead [18]. Such inverted-Mexican-hat-shape VBM was also predicted in γ-InSe when the ambient pressure increases above 3 GPa [159] and in β-GaS thinner than 8 layers [160]. The layer-number dependence of band gap is also observed in other III-VI semiconductors [161].
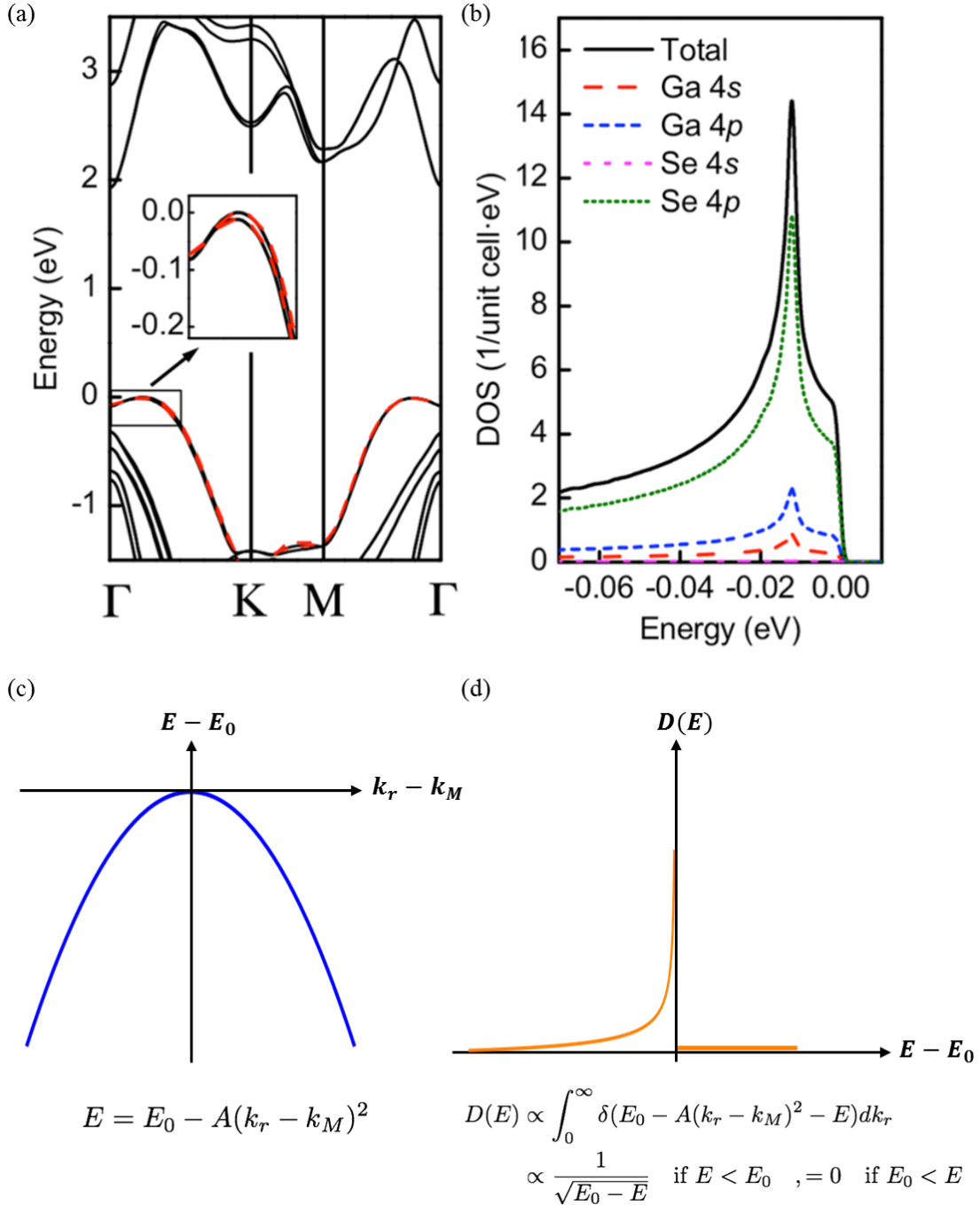
Figure 3-5. (a) and (b) are electronic band structures of undoped monolayer GaSe based on first-principle calculations. (c) and (d) are 1D parabolic dispersion and its density of state.

(a) Fully relativistic band structure. The black solid lines are calculated with the local density approximation (LDA) functional. The red dashed lines are calculated with the GW method. An undoped monolayer GaSe has an indirect band gap about 2 eV, which is roughly 1 eV smaller than the experimentally determined band gap [162]. The inset is a magnified view near the Γ point. The energy maxima is almost degenerate along different

directions. For example, the energy maximum along Γ–K and Γ–M directions only differ by 0.01 eV. (B) Total and partial density of states (DOS) near valence band maximum, which is set as 0 eV. The DOS from Se 4p orbital contributes most of the total DOS in this energy region. Because the Gaussian broadening of 0.001 eV is used, the DOS is finite. (c) Parabolic dispersion in one dimension with energy maximum E_0 at wave vector k_M. (d) Density of state (DOS) calculated from (c). DOS has a singularity at E_0. (Figure (a) and (b) are taken from Cao et al. [18].)

3.2 Oxidation and Passivation of GaSe

We exfoliate few-layer GaSe sheets from bulk crystals grown by Dr. Thomas Mallouk's group using the technique of chemical vapor transport. The material consists of β and ε polytypes.

There are two major difficulties that need to be overcome when constructing GaSe devices: quick oxidation [163, 164] and how to make electrical contact to GaSe. Figure 3-6 compares the oxidation situation when GaSe is stored in a humid place and in a desiccator. When GaSe stays in a humid environment for one day, islands form on the material and flake thickness changes, which we think is an indication of oxidation. Previous study also reported that GaSe is sensitive to water absorption, which changes the resistance of devices over time [15]. There are signs of oxidation can be seen optically: appearance of islands on thick flakes and flake color changes indicating the change of flake thickness and composition (Figure 3-6(b)). Islands on thin flakes can be detected with atomic force microscopy (Figure 3-6(d)). GaSe flakes oxidize much more slowly when they are stored in a desiccator (Figure 3-6(e) and (f)). To prevent GaSe from oxidizing, exfoliated GaSe sheets are stored in vacuum. In fabrication of some devices, exfoliation and dry transfer are done inside a plastic bag with continuous nitrogen flow

and the GaSe flakes are passivated with hexagonal boron nitride (BN) flakes.
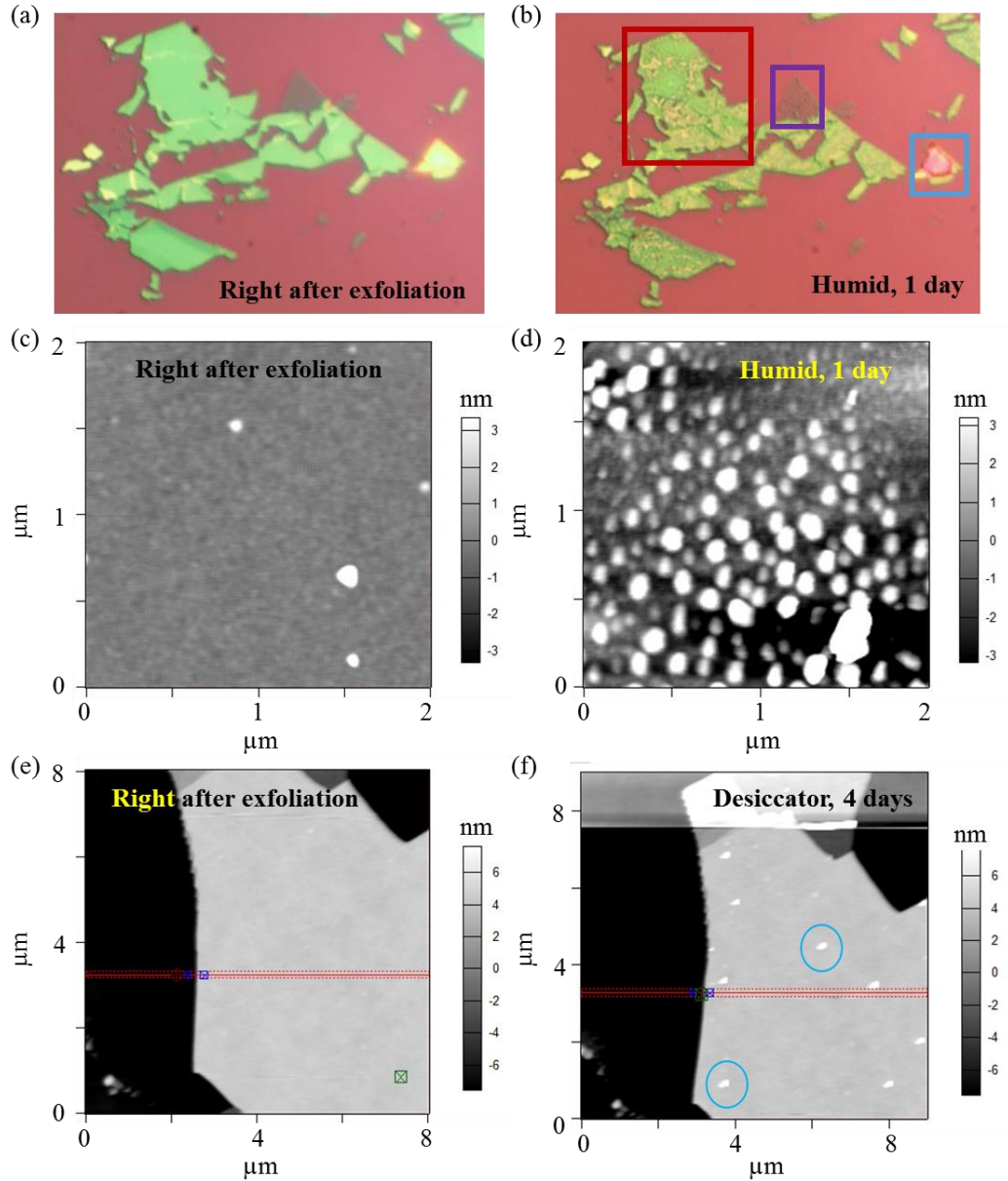
Figure 3-6. Oxidation of GaSe flakes in humid and dry environments.
(a) and (c) are optical and atomic force microscopy images of flakes taken right after exfoliation, respectively. (b) and (d) are images of the same flakes taken after being stored in a closed box with water for one day, which show signs of oxidation. In (b), we can see that islands form and flakes become uneven (boxed in red). Some thin flakes appear more transparent (boxed in purple). Some flakes change color (boxed in cyan). In (d), several-nanometer tall islands form densely on the flake. (e) and (f) are atomic force

microscopy images taken right after exfoliation and after being stored in a Secador desiccator for four days. The height and morphology of most part of the flake remains the same after the four-day storage. Some islands form (cyan circles indicate two islands), which signals some oxidation.

In order to make electrical contact to the GaSe sheet underneath the BN, we need to pattern windows on the BN. We tried two methods. The first is using a focused ion beam (FIB). There are two major benefits of this method. If we make a BN/GaSe heterostructure first and can control the milling rate well, we can mill through BN and immediately deposit metal at the same tool, which reduces the time GaSe exposed to air. The other benefit is that FIB can do the milling and deposition faster in comparison to e-beam lithography. But there are a couple challenges. Firstly it is impossible not to mill away the material beneath BN but ensure BN is etched through. So we decided to mill BN on a separate SiO_2/Si substrate and try to pick up the BN. We could not pick up the BN milled by FIB in the first couple shots. We thought the failure might be caused by the piling up of material around the windows (shown in Figure 3-7(b)). Thus before picking the BN flakes up, we exposed BN briefly to a CHF_3/O_2 plasma, following the procedure in the paper of Handschin et al. [165]. According to atomic force microscopy scans before and after the plasma etching, the BN surface around the windows became smoother and about 6 nm BN was etched away. Then we tried two methods to pick the BN up: (1) picking up with a PPC/tape/PDMS stamp [2], (2) spin-coating PPC on the wafer with BN and peeling it off, but neither of them worked. Both methods could be used to pick up pristine BN successfully; however, not any portion of the drilled BN flakes was picked up. Later we tried patterning the windows with e-beam lithography and reactive ion etching (Figure 3-7(d)-(f)) [51]. Without the problem of material pileup

faced in FIB process (Figure 3-7(a)-(c)), the prepatterned BN can be successfully picked up with a PPC/tape/PDMS stamp.
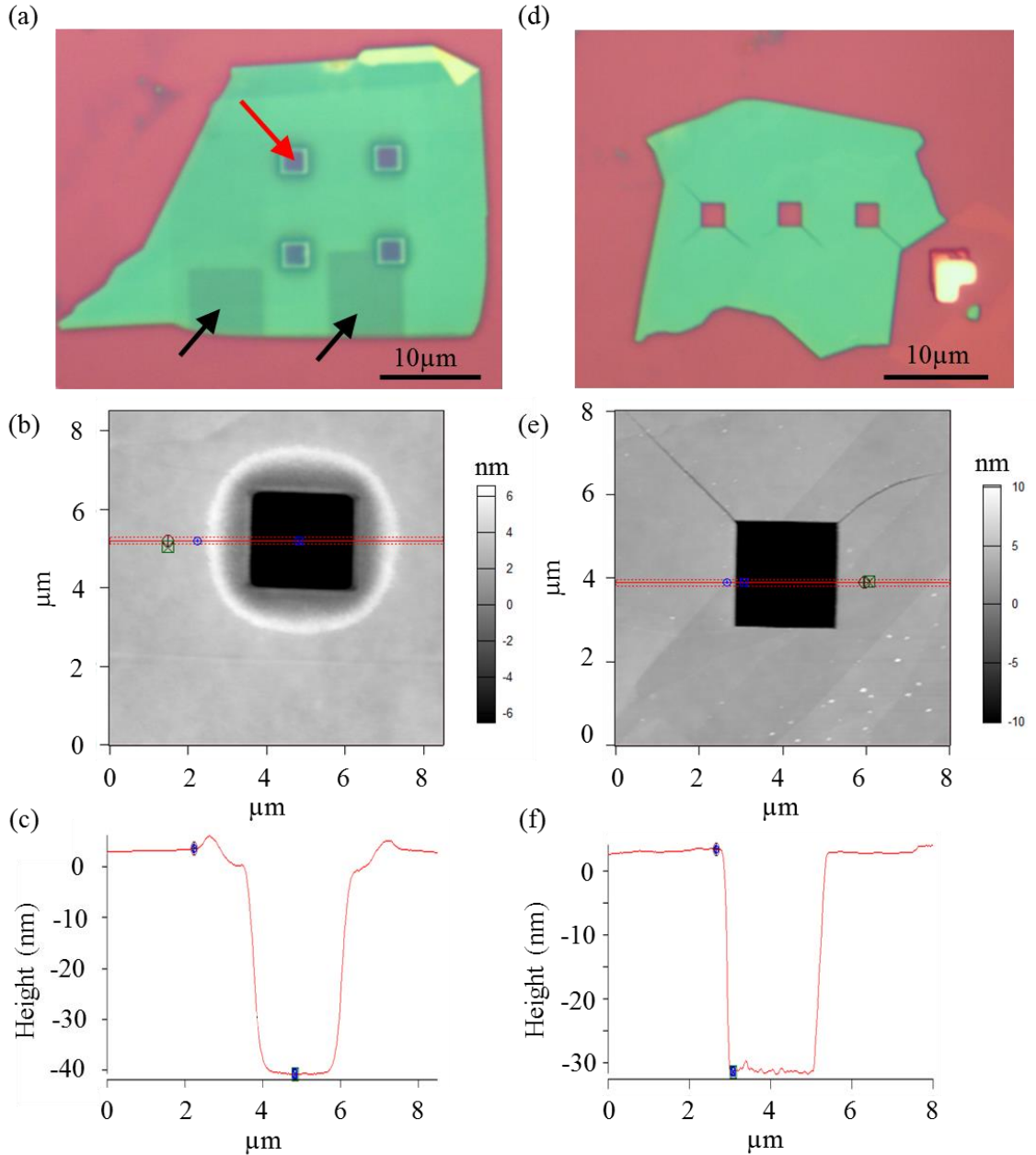
Figure 3-7. Prepatterned windows on 30 ~ 40 nm thick BNs.
(a)-(c) Optical image, atomic force microscopy image, and height profile of windows drilled by a gallium focused ion beam, respectively. (a) Four 2.5 μm × 2.5 μm windows are drilled through a BN flake (indicated by the red arrow). The two black arrows point to two boxes where gallium deposits during ion beam focusing. (b) Atomic force microscopy image of one window shown in (a). Material removed away from the window

piles up around the window (the white circle surrounding the black window). (c) Height profile along the red line in (b). The two blue dots correspond to the height of the two blue dots in (b). The height of the "white circle" in (b) is about 2 nm. The depth of the holes is the thickness of BN plus about 15 nm; in other words, about 15 nm SiO_2 below the BN is drilled away. (d)-(f) Optical image, atomic force microscopy image, and height profile of windows defined by e-beam lithography and etched by reactive ion etching. (e) Image of one window in (d), showing that the surface around the window is clean and flat. (f) Height profile along the red line in (e). The wall of the hole is straight and there is nothing piling up on the surface of BN.

3.3 Toward Better Electrical Contact to Few-Layer GaSe

3.3.1 GaO/Ti/Au electrodes

The band gap of GaSe increases with decreasing layer number (see Figure 3-3(b)) [17, 21, 166]. Due to the large band gap and quick oxidation, it is challenging to make electrical contact to few-layer GaSe. To probe the predicted magnetism, we need an inverted-Mexican-hat-like band structure, which means that we might need the layer number of GaSe to be fewer than 4 layers. Ohmic contact to large-area p-type bulk GaSe can be achieved by indium [167, 168]. Contact metal with a high work function has been used in a recent study of GaSe transistors [15]. They successfully made electrical contact to GaSe valence band with Ti/Au contacts, where gold has a high work function of 5.1 eV [169]. We fabricated a device with Au electrodes contacting GaSe of 7~10 layer, but the two-probe resistance of the device is about the order of 100 GΩ.

Though the onset of a p-type conduction is observed in the study of Late et al. [15], the performance of the contacts is poor and the reported mobility is 0.6 cm^2 $V^{-1}s^{-1}$. Inspired by the success in contacting p-type GaN, MoS_2 and WSe_2 with oxide contacts [170-172], we attempted to grow a thin layer of gallium oxide on top of GaSe (shown in

Figure 3-8), which could serve as a tunnel barrier between the metal contact and GaSe to depin the Fermi level.
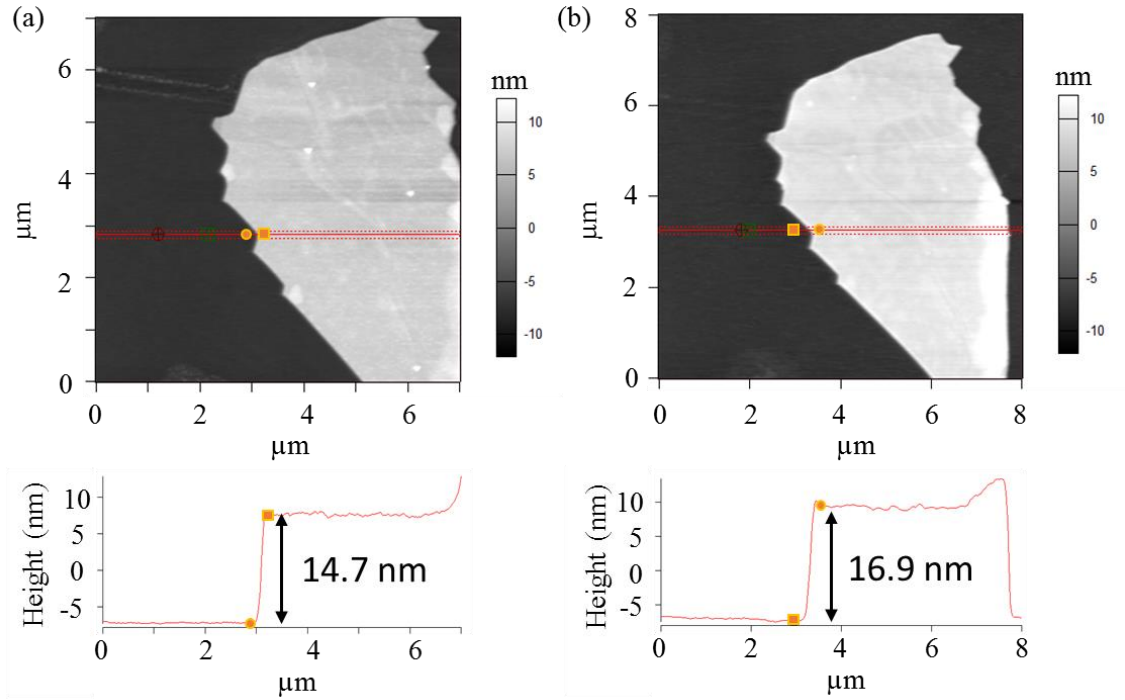
Figure 3-8. Atomic force microscopic images of GaSe flake after UV-ozone treatment. (a) is a pristine GaSe flake and (b) is the same flake after UV-ozone treatment with O_2 flow 0.1 L/min for 1 minute at 50C (b). The lower panel of each figure is the average height profile along the red lines of the atomic force microscopy images in the upper panel. After the UV-ozone treatment, there is a smooth amorphous gallium oxide film grown on top of the flake, which increases the flake thickness by approximately 2.2 nm. We noticed that the oxidation of GaSe is not self-limiting. Within the first 4 minutes' UV-ozone treatment, the oxide becomes thicker and rougher when the treatment gets longer.

Figure 3-9(a) shows the scheme of a bottom gated few-layer GaSe device. To fabricate this structure, we first exfoliate thin GaSe sheets onto a polydimethylsiloxane (PDMS) stamp. A desired flake is identified with optical microscope. Then a prepatterned

BN flake is used to pick up GaSe using a dry transfer technique developed for BN/graphene/BN stacks [51]. The BN/GaSe stack is then deposited onto a prefabricated HfO$_2$ /Au gate stack. We choose HfO$_2$, a high κ dielectric, as the gate material [173] in order to achieve the doping level needed to observe the predicted magnetism. Afterward, the BN/GaSe stack is UV-ozone treated to grow a 2~3 nm Gallium oxide on top of the GaSe exposed through the BN windows. Ti/Au contact is then deposited. An optical image of a finished device is shown in Figure 3-9(b). Unfortunately we could not make contact to GaSe with gallium oxide and Ti/Au.
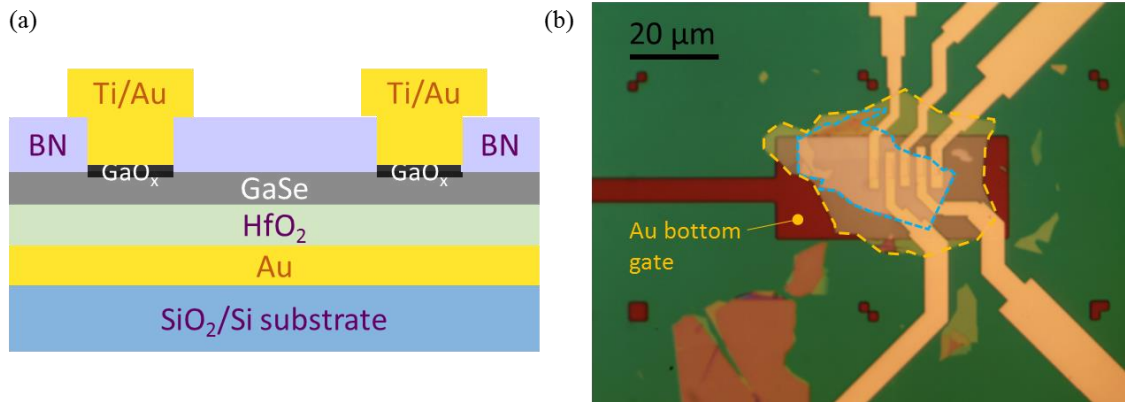
Figure 3-9. Schematic side view and optical image of BN encapsulated GaSe devices. (a) The schematic side view of BN encapsulated GaSe devices. (b) Optical image of BN encapsulated GaSe devices. BN/GaSe stack is transferred onto a prefabricated HfO$_2$ /Au substrate. GaSe and BN are outlined with cyan and yellow dashed lines, respectively. GaSe in this image is 15~20 layers thick.

3.3.2 NiO/Au electrodes

In comparison with gallium oxide, we thought NiO might be a better tunnel barrier to contact the valence band of GaSe because NiO is naturally p-type while the amorphous gallium oxide might be n-doped, like the case in Ga$_2$O$_3$ [174]. Oxidized Ni/Au has been

commonly used in contacting p-type GaN [170, 175-177]. Different mechanisms were proposed. Ho et al. attributed the low contact resistivity to the formation of NiO semiconductor on top of p-GaN [170]. According to their band alignment studies, holes are trapped at the NiO/GaN interface because the valence band of NiO bends upward and exceeds the Fermi level near the interface. They also mentioned the possible contribution from the amorphous Ni-Ga-O phase. Koide et al. attributed the ohmic contact characteristics to the removal of hydrogen that passivates Mg acceptors used for p-type doping [175]. They thought that hydrogen might be removed by forming H_2O during the annealing in an oxygen. Maeda et al. investigated various Ni/Au based contact with NiO layer, where NiO was sputtered before Au deposition, and found that these contacts were nonohmic [178]. From the previous researches on annealed Ni/Au contact to p-GaN, we learned that the annealing process is critical to make Ni/Au an Ohmic contact with a low contact resistivity. Though the details of the mechanism are still open to debate, we think the diffusion and reaction nature of Ni and its high work function make Ni/Au a possible candidate for achieving a good Ohmic contact to GaSe.

Figure 3-10 shows one device with annealed Ni/Au electrodes. GaSe flakes are exfoliated on a SiO_2/Si wafer, Au/Ni electrodes are then deposited on them, and the wafer is treated with rapid thermal annealing (RTA) at 500 ˚C for 10 minutes in air to oxidize Ni. It turns out that the devices do not conduct. We suspect that the RTA process also oxidizes a large portion of GaSe, which is not as stable as GaN. Based on the transparency and color of the optical images, we think at least 6~15 nm of GaSe is oxidized (shown in Figure 3-10). The color of some GaSe in optical images become red, which we have never seen on pristine GaSe flakes.
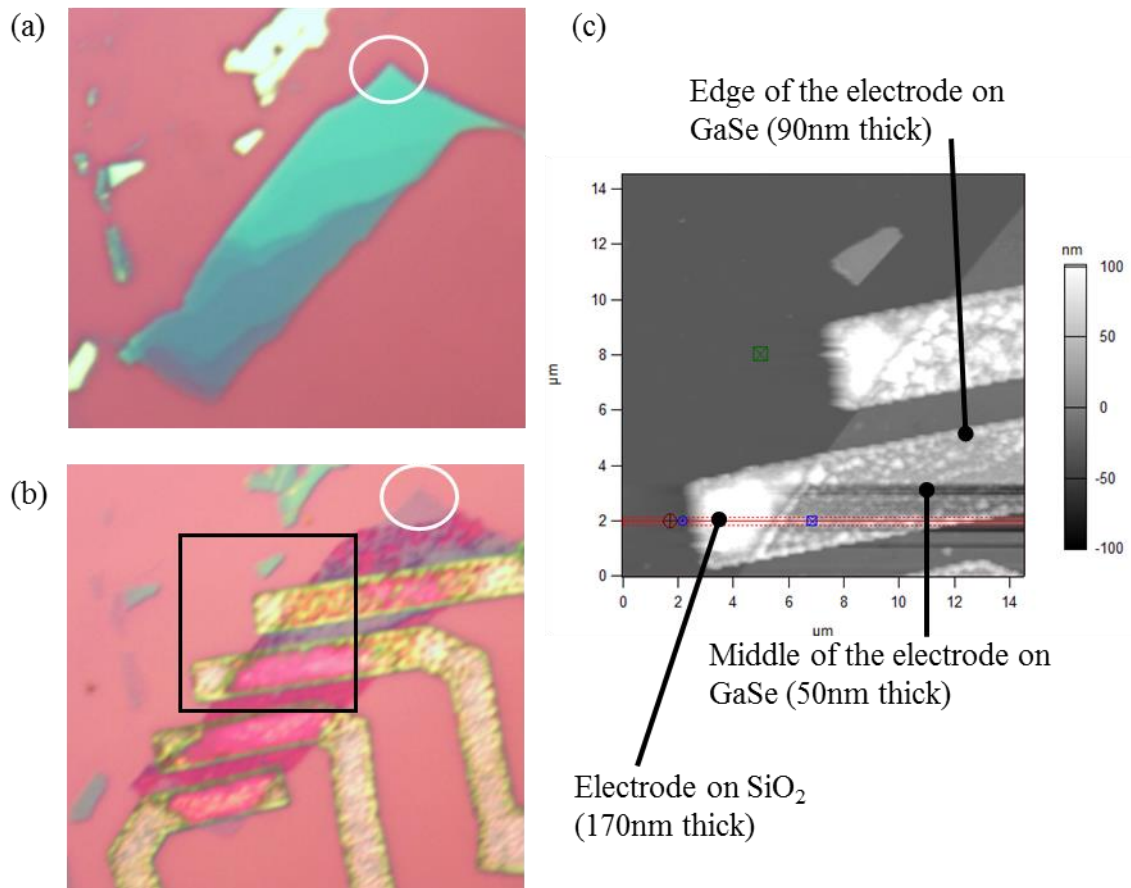
Figure 3-10. Images of a flake with Ni/Au electrodes before and after RTA in air. (a) Optical image of a pristine GaSe flake on SiO_2 substrate. The flake has various thickness, which we estimate to be 6 nm ~ 12 nm (circled in white) based on its color. (b) Optical image of the flake in (a) with Ni/Au electrodes after RTA in air at 500 ˚C for 10 minutes. Most part of the flake appears red, which is not a typical color of GaSe. The part in white circle appears to be about 3~4 nm thick based on its color, which indicates that at least 8 nm of GaSe has oxidized. (c) Atomic force microscopy image of the region boxed in black in (b). The thickness of different parts of the electrodes are labeled, which we find is very different from their as-deposited thickness: 20 nm Ni plus 20 nm Au. We suspect that the dramatic height change is due to the formation of voids [179].

3.3.3 Ni/Au electrodes

To prevent GaSe from oxidizing, we thought we could try annealing the device in an inert N_2 ambient. This way we can still use the diffusion of Ni to make a better contact to

GaSe. Another advantage Ni has is that it has a high work function around 5.15 eV [169]. Au-Ge-Ni layers have been widely used as Ohmic contact to n-GaAs. Nickel is found to improve the wetting of Au/Ge layer and thus produce a more uniform contact surface [180]. After annealing at 450~550 ˚C, Ni reacts with GaAs and forms NiAs, which acts as a transport medium for Ge to migrate deeper into GaAs, form Ge_2GeAs phase, and thus reduces the contact resistivity [181, 182]. Ni deposited on GaAs is found to diffuse through the native oxide-hydrocarbon layer on the surface of GaAs and react with GaAs [183]. Similar diffusion behavior of Ni is also seen in Ni or Ni/Au contacts on p-GaN [176, 184]. Ni/Au contacts generally produce a specific contact resistivity of $\sim 10^{-2}$ $\Omega \cdot cm^2$ when contacting p-GaN [177]. Though the reduction in contact resistance is not as prominent when Ni/Au contact is annealed in N_2 as in O_2, annealing in N_2 can reduce the specific contact resistivity to $\sim 10^{-3}$ $\Omega \cdot cm^2$ after annealing at 400~500 ˚C [176].

We thus made another batch of devices with the following fabrication steps. GaSe flakes were exfoliated on SiO_2/Si substrate. Each desired flake was then passivated by a BN flake. To contact GaSe, we etched windows through BN with CHF_3/O_2 (40/4 sccm under pressure 75mTorr). To ensure BN was etched through, we inevitably might have etched GaSe underneath BN so this time we worked with thicker GaSe flakes (~30 nm thick). Nickel of 13 nm was then deposited covering the windows, which was followed by deposition of 37 nm Au to protect Ni from quick oxidation in air. We measured the resistance of the devices for reference before they were treated with RTA at 220 ˚C in 10 slpm N_2 for 10 minutes. Figure 3-11 shows the optical images of the devices.
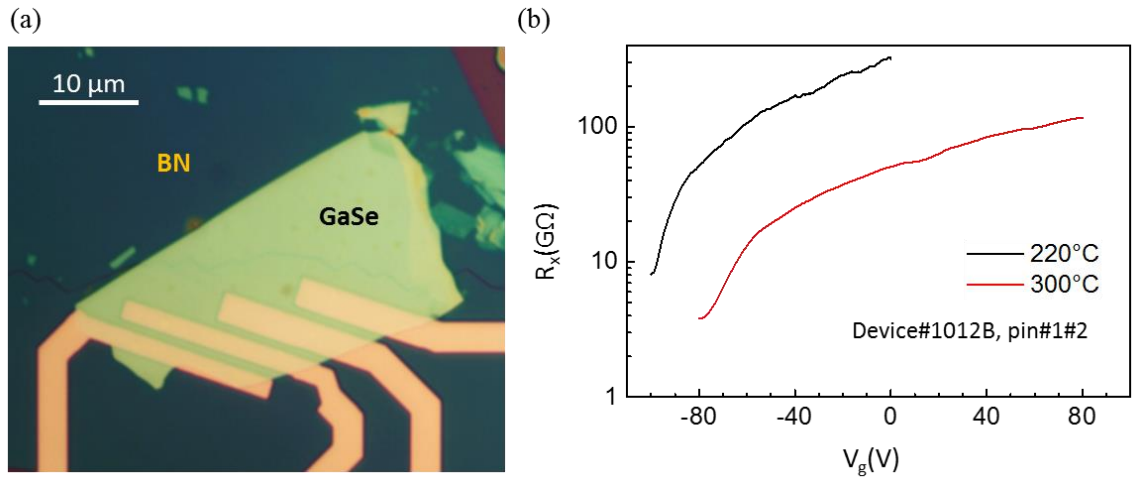
Figure 3-11. Optical image and electrical performance of GaSe device with Ni/Au electrodes annealed at 220 ˚C and 300 ˚C in N2.
(a) Optical image of a GaSe device encapsulated with a large BN. After the desired GaSe flake is identified, a BN flake is transferred on top of it, windows are etched through BN in order to contact GaSe, Ni/Au electrodes are deposited covering the windows, and then the device is annealed at 220 ˚C in N_2 for 10 minutes. (b) Gate voltage dependence of two-probe resistance of the device shown in (a). The gate voltage is applied across 300 nm thick SiO_2 layer. Black curve is the data taken after the annealing at 220 ˚C. Then the device is annealed at 300 ˚C for 5 minutes, which can reduce the resistance by up to a factor of 10 (red curve).

From two-probe resistance measurements, each device became one order more conductive after the RTA treatment at 220 ˚C. However the two-probe resistance was still high, from 40 MΩ to 10 GΩ. We then treated one device with RTA in N_2 at 300 ˚C for 5 minutes to see if the treatment could decrease the contact resistance. The treatment indeed decreased the two-probe resistance by one order (shown in Figure 3-11(b)).

A different temperature or duration of RTA treatment can make a difference. One device was treated with RTA in N_2 at 400 ˚C for 10 minutes and this treatment led to another problem: most neighboring electrodes became short with each other. In the optical image (Figure 3-12(c)), we saw some "brown fluid" flowing out from the electrodes near the edge of GaSe. We suspect that it was Ni flowing through the space between GaSe and BN and it caused most electrodes to become short. We think BN does not contact GaSe well near the edge of GaSe, where BN has to go from a higher place (GaSe) to a lower one (SiO_2). There is no sign of "brown fluid" near the edge of BN because BN contacts SiO_2 well, where BN stays on the same level.
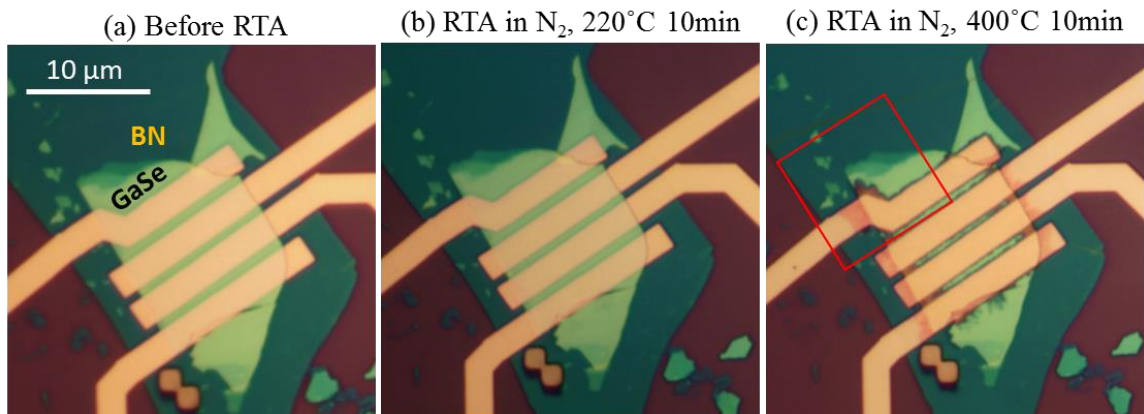
Figure 3-12. Optical images of GaSe device with Ni/Au electrodes at 3 consecutive steps. (a) Image of the device right after Ni/Au electrode deposition (before annealing). (b) After annealing at 220 ˚C in N_2 for 10 minutes. No obvious change in the appearance of the device. (c) After annealing at 400 ˚C in N_2 for 10 minutes. There is "brown fluid" flowing out from the electrodes, especially near the edge of GaSe. We suspect that this fluid causes neighboring electrodes short with each other.
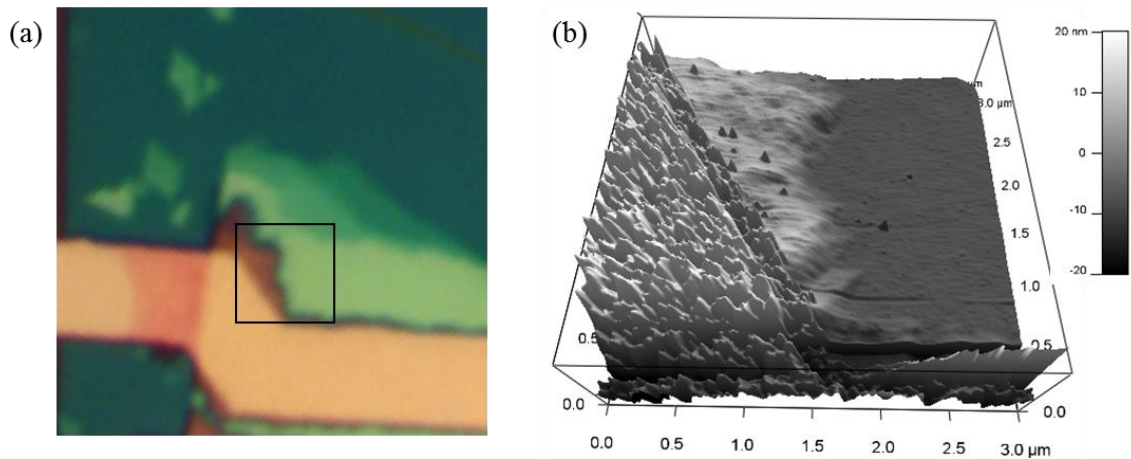
Figure 3-13. Magnified images near GaSe edge after RTA at 400˚C in N_2 for 10 minutes. (a) Magnified optical image near edge of GaSe flake in Figure 3-12(c), which is boxed in red. (b) Atomic force microscopy image of the region boxed in black in (a).

3.4 Conclusion

We have implemented and investigated several ideas toward fabricating higher-quality GaSe devices. To prevent GaSe from quick oxidation, we developed a method to protect GaSe with pre-patterned BN using e-beam lithography and dry transfer technique. We also find that among the three kinds of contacts to GaSe: GaO/Ti/Au, NiO/Au, and Ni/Au electrodes, Ni/Au electrodes annealed in N_2 at 220 ˚C then 300 ˚C have the lowest contact resistance, which might be attributed to the diffusion of Ni. Our work suggests a way to passivate GaSe and the possibility to make a better contact to GaSe with annealed Ni/Au electrodes.

Chapter 4

Ferromagnetism in van der Waals Compound $MnSb_{1.8}Bi_{0.2}Te_4$

4.1 Motivation and Introduction to $Mn(Bi, Sb)_2Te_4$ System

A central theme of contemporary condensed matter research explores the notion of topology and symmetry to generate novel quantum phenomena [185]. A good example is the quantum anomalous Hall effect (QAHE) found in magnetic topological insulators (TI) $Cr_{0.15}(Bi, Sb)_{1.85}Te_3$, where magnetism introduced by Cr doping breaks the time reversal symmetry and gives rise to robust chiral edge states that can carry current ballistically without the need of an external magnetic field [186, 187]. Chiral magnetic textures such as skyrmions are another good example [188-190]. The generation of spin chirality requires the breaking of crystalline inversion symmetry, which can be achieved in bulk materials [191-193] or in heterostructures that combine ferromagnetism (FM) with strong spin orbit coupling [194-198]. Magnetism and heterostructures in the van der Waals (vdW) geometry provides another powerful natural platform to explore magnetic anisotropy and interface effect, with the added benefit of electric field control for potential device applications [68, 77, 80, 81, 199, 200].

Recent research activities have identified $Mn(Bi, Sb)_2Te_4$, a vdW magnetic family with strong spin orbit coupling, to be promising candidates in realizing the QAHE above dilution refrigerator temperatures [83-94]. $Mn(Bi, Sb)_2Te_4$ can be regarded as consisting of a Mn-Te layer inserted into the quintuple layer of $(Bi, Sb)_2Te_3$ Figure 4-1. Here moments carried by an ordered Mn layers can create an internal magnetic field without introducing random disorder. In the most studied compound $MnBi_2Te_4$, the interlayer Mn coupling was found to be A-type antiferromagnetic (AFM) [83-85, 92, 93, 201-203]. The

AFM ground state was also favored in other compositions of the compound family [93] with the exception of a recent report of ferrimagnetism in polycrystalline $MnSb_2Te_4$ [204].
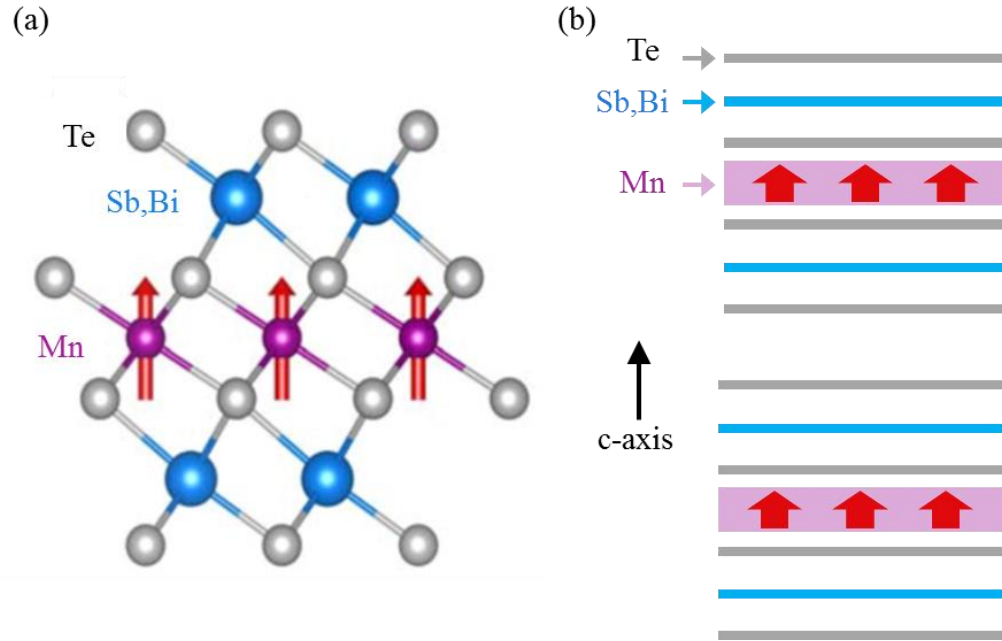
Figure 4-1. Schematic crystal structure of $Mn(Sb,Bi)_2Te_4$.
(a) Schematic crystal structure of monolayer $Mn(Sb,Bi)_2Te_4$, where silver, blue, and magenta circles represent Te, Sb/Bi, and Mn atoms, respectively. One monolayer consists of a Te−Sb/Bi−Te−Mn−Te−Sb/Bi−Te septuple layer. The red arrows depict the magnetic moment of each Mn atom, whose easy axis is out-of-plane. (Figure adapted from Li et al [90].) (b) Schematic sideview of stacking order of $Mn(Sb,Bi)_2Te_4$.

In an antiferromagnetic topological insulator like $MnBi_2Te_4$, QAHE can only be achieved in those with odd numbers of layers. In such case, the magnetization at top and bottom surfaces are parallel and the Hall conductance from the top and bottom surfaces have the same signs and can result in a nonzero Hall conductance $\pm e^2/h$ [187]. Quantized conductance in $MnBi_2Te_4$ with odd numbers of septuple layers has been observed experimentally at zero magnetic field [86]. When the layer number is even, the magnetization at top and bottom surfaces of $MnBi_2Te_4$ are antiparallel and the Hall

conductance from the top and bottom surfaces cancel each other, resulting in a zero Hall conductance [87, 187]. Thus a topological material with a ferromagnetic bulk would offer a new platform for the realization of the QAHE without imposing the odd-layer-number requirement. Furthermore, ferromagnetic order was reported to be able to stabilize QAHE against thermal fluctuations and realize QAHE at a higher temperature [86]. Ferromagnetism in topological materials can open the door to other interesting possibilities such as time reversal symmetry breaking type -II Weyl semimetal [204, 205].

In this chapter, we show that under certain synthetic conditions, single-crystalline $MnSb_{1.8}Bi_{0.2}Te_4$ can be stabilized into a phase with a net ferromagnetic moment and a Curie temperature of $T_C = 26$ K. We present transport, magnetometry and neutron diffraction measurements that illustrate the properties of this state, which we denote as the "FM" state. Refinements of x-ray and neutron diffraction data reveal considerable Mn-Sb site mixing, which supports a recent Mn layer-to-Mn Layer ferromagnetic coupling mechanism discussed in Ref. [204]. Interestingly, our sample also exhibits a sizable unconventional anomalous Hall effect that signals the possibility of additional magnetic structures at very low temperatures. Further understanding of the rich magnetic orders the $Mn(Bi, Sb)_2Te_4$ family exhibits and their correlation with local chemistry opens up new possibilities of engineering magnetic and topological phenomena in this vdW family with potential prospect in device applications.

4.2 Synthesis and Characterization of MnSb$_{1.8}$Bi$_{0.2}$Te$_4$ and MnSb$_2$Te$_4$

MnSb$_{1.8}$Bi$_{0.2}$Te$_4$ single crystals exhibiting the FM state were synthesized using a flux method by our collaborators Seng Huat Lee et al. from Dr. Zhiqiang Mao's group [206]. A mixture of high purity Mn powder (99.95%), Bi shot (99.999%), antimony shot (99.9999%) and Te ingot (99.9999+%) with the molar ratio of Mn:Sb:Bi:Te = 1:9:1:16 was loaded into an Al$_2$O$_3$ crucible and sealed in an evacuated quartz tube. The mixture was heated up to 900°C for 12 hours to promote homogeneous melting and then slowly cooled down to 595 °C at a rate of 2°C/h and dwelled at this temperature for 24 h. It is then further cooled down to 400°C within 3 hours and then immediately heated back to 625°C in 1 hour and dwelled at this temperature for another 2 hours. The final step is quenching and centrifuging at 625°C. The treatment of cooling down the melt from 900°C to 400 °C before quenching is critical to the synthesis of the FM state in MnSb$_{1.8}$Bi$_{0.2}$Te$_4$. Cooling the melt directly to 625°C leads to an AFM ground state similar to prior results[93]. Our collaborators Lee et al. also attempted synthesizing MnSb$_2$Te$_4$ crystals using the same method, but obtained only MnSb$_2$Te$_4$ crystals exhibiting the AFM ground state. MnSb$_2$Te$_4$ crystals used in this study were prepared using a flux-method similar to that used by Yan *et al* [93]. They performed X-ray diffraction (XRD) and scanning transmission electron microscopy (STEM) measurements, which confirms the septuple layer rhombohedral structural phase in both materials. Measurements presented in the rest of this chapter are obtained on crystals and exfoliated flakes with greater than 95% purity in the primary Mn(Sb, Bi)$_2$Te$_4$ phase. Powdered polycrystalline samples of both MnSb$_{1.8}$Bi$_{0.2}$Te$_4$ and MnSb$_2$Te$_4$ are grown with the same methodologies and are verified to have the same magnetic ground states as their single crystal counterparts. They

are used for neutron powder diffraction (NPD) studies. Reitveld analysis on the NPD was performed using a combination of the FullProf and GSAS-II programs.

4.3 Experimental Methods

A scheme of a typical device is shown in Figure 4-1. Micrometer-sized flakes are exfoliated from selected crystals and transferred using a polypropylene carbonate stamp to pre-patterned Ti/Pt electrodes inside a glovebox filled with argon gas. The finished device is covered with a droplet of Poly(Methyl MethAcrylate) before transferred to a pumped ^{4}He cryostat. Figure 4-2(b) shows an optical image of a typical Hall bar device. Flakes of similar color tone measure 100-300 nm in thickness in an atomic force microscope. Transport measurements are performed in a pumped ^{4}He cryostat with a magnetic field up to 9 T using standard low-frequency techniques. Magnetometry measurements are performed in a SQUID magnetometer from 2-300 K. Single crystal elastic neutron scattering measurements are performed using the BT-4 triple-axis spectrometer (TAS) and NPD measurements were made on the BT-1 powder diffractometers at the NIST Center for Neutron Research (NCNR). The BT-1 measurements were made using 60' collimation with both Cu(311) and Ge(311) monochrometers. TAS measurements were taken with an instrument configuration of open-pg-pg-40'-s-pg-40'-100' where pg refers to pyrolytic graphite.
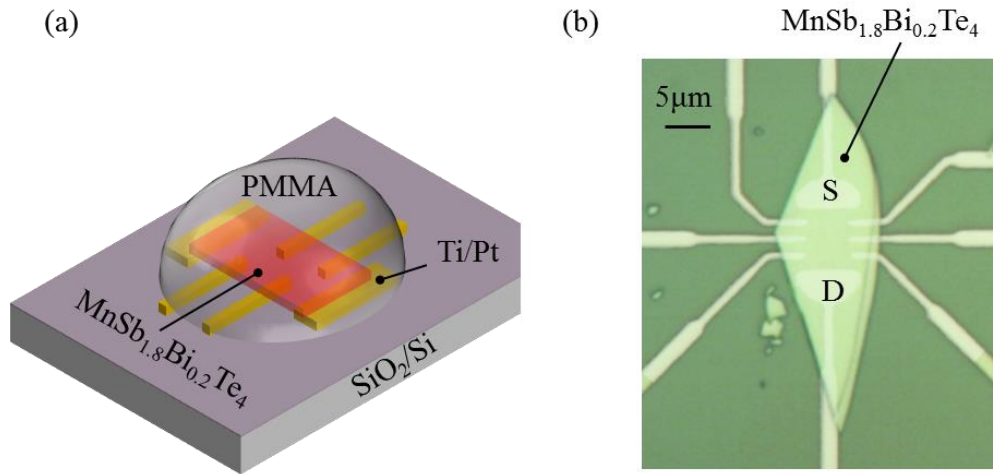
Figure 4-2. Images of a typical MnSb$_{1.8}$Bi$_{0.2}$Te$_4$ device in a Hall bar geometry. (a) The scheme illustrates that a thin MnSb$_{1.8}$Bi$_{0.2}$Te$_4$ flake (colored in red) is transferred onto a pre-patterned Ti/Pt electrodes and then covered by a droplet of Poly(Methyl MethAcrylate) (PMMA). (b) The optical image shows the top view of a MnSb$_{1.8}$Bi$_{0.2}$Te$_4$ device. The electrodes underneath the flake are added on top of the optical image and shaded in white.

4.4 Demonstration of Ferromagnetism in Magnetoresistance

Figure 4-3 plots the Hall resistance $R_{xy}(H)$ obtained on a MnSb$_{1.8}$Bi$_{0.2}$Te$_4$ device. A small R_{xx} component is removed from the data though an asymmetrization step that averages the upsweep of $R_{xy}(H)$ and the downsweep of $-R_{xy}(-H)$. Measurements were taken at a series of fixed temperatures ranging from 2 to 60 K. Traces plotted here represent the typical behavior in different temperature ranges. As the $T = 60$ K trace shows, $R_{xy}(H)$ is a straight line from -9 T to 9 T at high temperatures. An anomalous Hall effect starts to develop at $T < 46$ K, where the slope dR_{xy}/dH taken at $R_{xy} = 0$ becomes

larger than the slope taken at high field. The difference of the two originates from a non-zero magnetization (M) of the sample since $R_{xy}(H) = R_0H + R_sM$ [207].
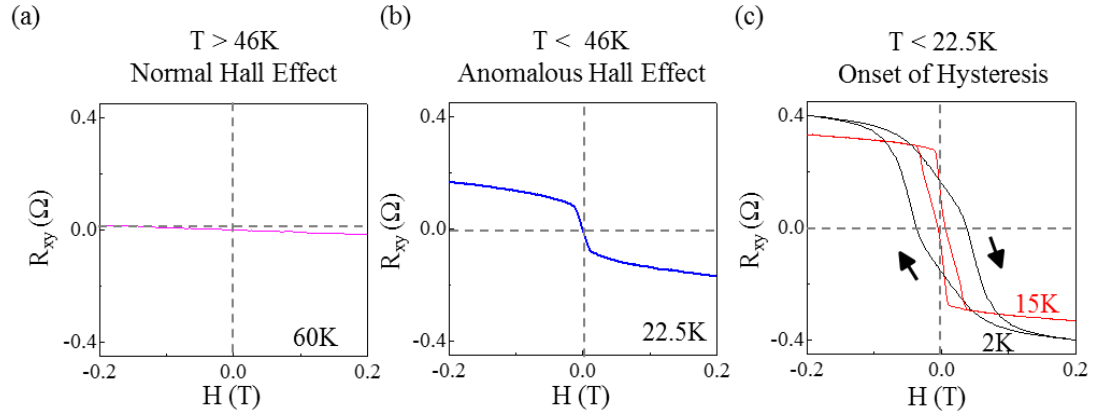
Figure 4-3. The Hall resistance R_{xy} (H) on a MnSb$_{1.8}$Bi$_{0.2}$Te$_4$ device device in low magnetic field at selected temperatures as labeled in the plot.

The three plots represent the typical behavior in different temperature ranges (a) At T > 46 K: normal Hall effect. (b) At T < 46 K: anomalous Hall effect. (c) At T < 22.5 K: onset of hysteresis. Arrows indicate the field sweep direction.
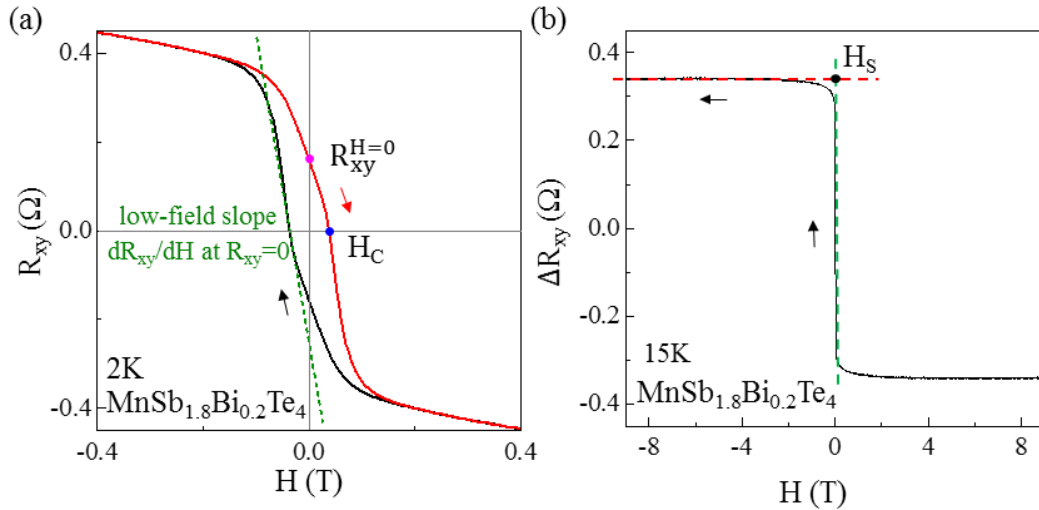
Figure 4-4. Definition of low-field slope, coercive field, remnant $R_{xy}^{H=0}$ and saturation field. The Hall resistance $R_{xy}(H)$ (a) and anomalous Hall component $\Delta R_{xy}(H)$ (b) on a MnSb$_{1.8}$Bi$_{0.2}$Te$_4$ device at 2 K, where black (red) curves indicate the downward (upward) sweeps. In (a), the green dotted line illustrates the slope at $R_{xy} = 0$, which we named as low-field slope dR_{xy}/dH. Coercive field H_C is defined by the blue dot and the remnant

Hall resistance $R_{xy}^{H=0}$ is defined by the magenta dot. In (b), $\Delta R_{xy}(H)$ is obtained by subtracting the normal Hall contribution $R_0 H$ from the measured $R_{xy}(H)$. The red dashed line traces out where ΔR_{xy} saturates and the green dashed line is the low-field slope. The intersection of the green and red dashed lines yields the saturation field H_s for the $T = 15$ K.

In addition to the anomalous Hall effect, $R_{xy}(H)$ becomes hysteretic at temperatures below ~ 22.5 K. Data at 2 K and 15 K are plotted to show the two different shapes of the hysteresis loop in Figure 4-3(c). Hysteresis is also observed in bulk magnetization measurements of the parent $MnSb_{1.8}Bi_{0.2}Te_4$ crystal. Our collaborators performed magnetometry measurements and extracted a remnant magnetization of $M_0 = 0.6$ μ_B/Mn, a coercive field of $H_c = 310$ Oe and a saturated M of 1.8 μ_B/Mn [206]. Both the H_c and $R_{xy}^{H=0}$ decrease with increasing temperature and vanish at $T > 23$ K, supporting the establishment of the FM state in this temperature vicinity (see Figure 4-5).
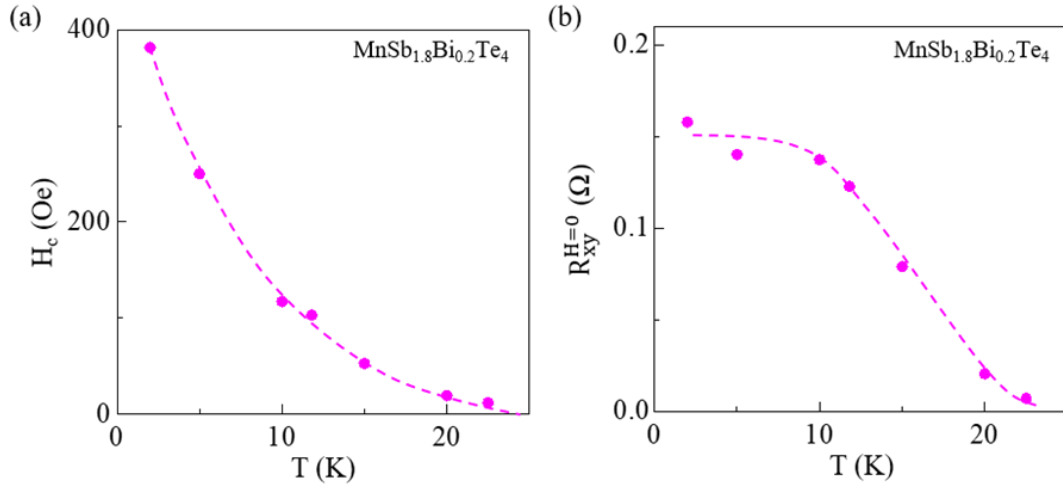
Figure 4-5. Temperature dependence of the coercive field and the remnant Hall resistance. The coercive field H_c (a) and the remnant Hall resistance $R_{xy}^{H=0}$ (b) as a function of temperature extracted from the R_{xy} data shown in Figure 4-3. Both support the onset of a ferromagnetic order at $T_C > 20$ K. Dashed lines are guide to the eye.

To understand the meaning of high (low)-field slope in magnetic field dependence of the Hall resistance, we can start with the paramagnetic model assuming $M = \chi H$. Then we have $R_{xy} = \frac{B}{ne} = \frac{\mu_0 H (1+\chi)}{ne}$. At sufficiently high field where M saturates and susceptibility χ is very small, the slope dR_{xy}/dH yields the normal Hall coefficient $R_0 = 1/ne$. At field near zero, $\chi \gg 1$ so the slope dR_{xy}/dH is dominated by the second term and linear to χ.

We determine the carrier density in our multi-layer devices using the slope of the Hall resistance near $H = 8 \sim 9$ T. The results are presented in Figure 4-6(a) for a MnSb$_{1.8}$Bi$_{0.2}$Te$_4$ and a MnSb$_2$Te$_4$ device as a function of temperature. The carrier doping is p-type in both materials and is roughly independent of temperature in the range we probed. From these measurements, we estimate a hole density of a few $\times$ 10^{13}/cm^2/septuple layer. This means the Fermi level is in the bulk valence band of the materials [93]. Though many layers are present in our devices, R_0 follows a cos θ dependence as the external field tilts away from the c-axis of the crystal (Figure 4-6(b)), which shows that the electronic transport of the carriers are two dimensional in nature.

In contrast, the slope dR_{xy}/dH taken at $R_{xy} = 0$, called the low-field slope from now on, increases rapidly with decreasing temperature and reaches a broad maximum around 12−20 K. Its T-dependence is plotted in Figure 4-7(a) as magenta circles. Similar measurements are performed on a MnSb$_2$Te$_4$ device and the results are plotted as blue squares.
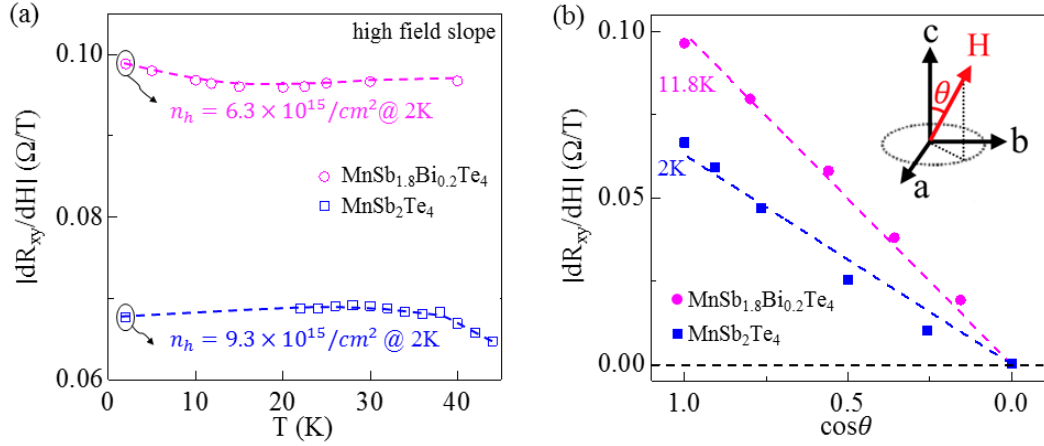
Figure 4-6. High-field slope $R_0 = dR_{xy}/dH$ in $MnSb_{1.8}Bi_{0.2}Te_4$ and $MnSb_2Te_4$.
(a) Temperature dependence of high-field slope. $R_0 = 1/ne$ yields the 2D carrier density.
(b) The angle θ dependence of R_0. The inset illustrates the definition of θ. The linear relation between dR_{xy}/dH and $\cos\theta$ indicates the 2D nature of the mobile carriers.
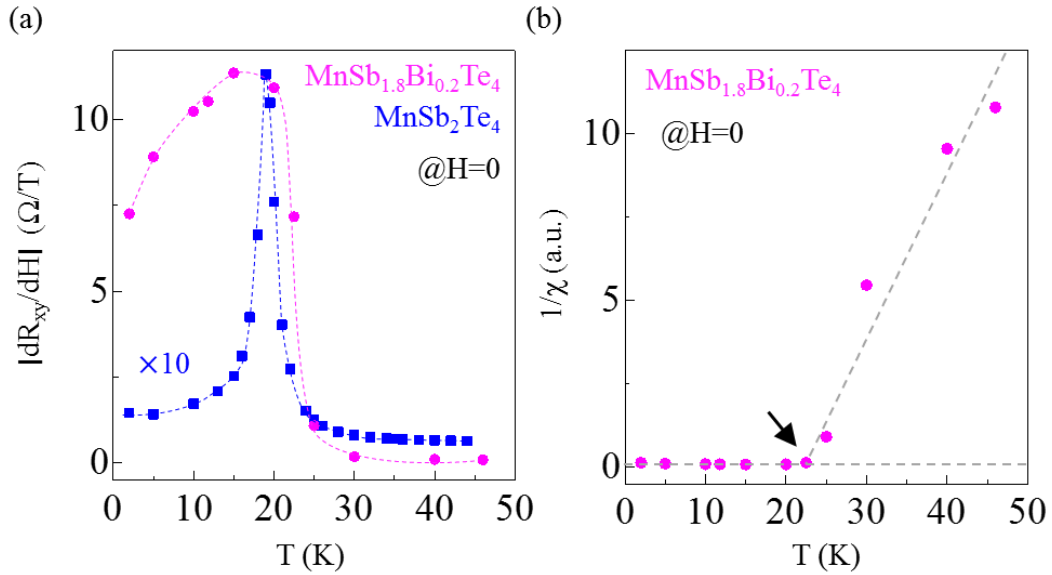
Figure 4-7. Low-field slope dR_{xy}/dH and $1/\chi$ in $MnSb_{1.8}Bi_{0.2}Te_4$ and $MnSb_2Te_4$.
(a) The temperature dependence of the low-field slope in $MnSb_{1.8}Bi_{0.2}Te_4$ (magenta circles) and $MnSb_2Te_4$ (blue squares).. The dashed lines are guide to the eye. (b) The temperature dependence of $1/\chi$ extracted from the reciprocal of low-field slope dR_{xy}/dH in $MnSb_{1.8}Bi_{0.2}Te_4$. The arrow indicates the transition temperature, which is around 22.5K.

To further explore the magnetic properties of $MnSb_{1.8}Bi_{0.2}Te_4$, we plot in Figure 4-7(a) the T-dependent magnetic susceptibility $\chi(T)$, extracted from the low-field slope of the Hall resistance dR_{xy}/dH. In a magnetic system, the low-field slope dR_{xy}/dH includes the contribution from the out-of-plane magnetic susceptibility $\chi = dM/dH$. In Figure 4-7(a), dR_{xy}/dH ascends rapidly at $T \sim 25$ K, reaches a maximum value of 11 Ω/T around 12 - 20 K, which is more than 100 times larger than the normal Hall coefficient $R_0 = 0.1$ Ω/T of this device, before dropping again at lower temperatures. In another words, the low-field dR_{xy}/dH is dominated by the magnetic response of the system and effectively measures the $\chi(T)$ of the microscope device. To identify the Curie temperature, we plot the temperature dependence of the reciprocal of dR_{xy}/dH, which is proportional to $1/\chi$ (Figure 4-7(b)). From the figure, we find that the transition temperature is around 22.5K.

The magnetometry studies conducted on bulk crystals by our collaborators from Dr. Zhiqiang Mao's group tell a similar story [206]. The 50 Oe ZFC data strongly resemble the low-field dR_{xy}/dH shown in Figure 4-7(a), suggesting that our samples behave homogeneously from the μm to the mm length scale. Both Hall resistance and DC magnetometry measurements support the onset of a FM order at a Curie temperature of $T_c \sim 26$ K. At $T < 12$ K, the dR_{xy}/dH data show a pronounced drop that deviates from a conventional FM. More complex magnetic phases may emerge in this temperature range [202, 208-210]. We aim to understand its nature with additional measurements and analyses [211].

4.5 H_s - T Phase Diagram in MnSb$_{1.8}$Bi$_{0.2}$Te$_4$

The sensitivity of R_{xy} to the magnitude of M enables us to determine the saturation field H_s in MnSb$_{1.8}$Bi$_{0.2}$Te$_4$ and construct a H_s - T phase diagram. To do this we first determine the anomalous Hall signal $\Delta R_{xy}(H) = R_{xy}(H) - R_0 H$ for the device shown in Figure 4-2(b). The results at several temperatures are shown in Figure 4-8(a). The saturation field H_s is defined as the field at which the extension of the low-field slope reaches the saturated value of ΔR_{xy}, as illustrated in Figure 4-4.
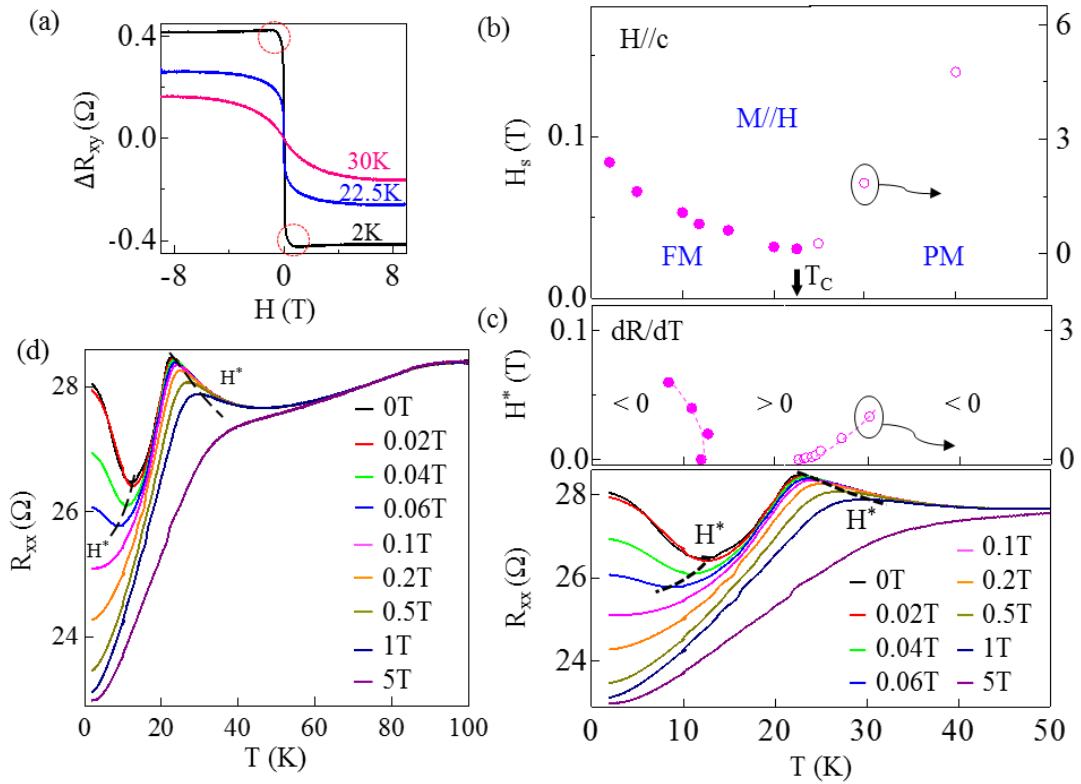
Figure 4-8. $\Delta R_{xy}(H)$ at different temperatures and $R_{xx}(T)$ at different magnetic fields. (a) The anomalous Hall component $\Delta R_{xy}(H)$ for the device shown in Figure 4-2(b) at selected temperatures. $\Delta R_{xy}(H)$ is obtained by subtracting the normal Hall contribution $R_0 H$ from the measured $R_{xy}(H)$. (b) Moment saturation field H_s versus T in MnSb$_{1.8}$Bi$_{0.2}$Te$_4$ obtained from $\Delta R_{xy}(H)$ data shown in (a). Solid symbols are data below T_C. Open symbols are data above T_C and use the right axis. (c) Lower panel: Temperature-dependent magnetoresistance $R_{xx}(T)$ taken at fixed magnetic field as labeled

in the plot. The black dashed lines divide the curves into three regions according to the sign of dR/dT. The boundary points are plotted in the upper panel of (c). The symbols follow the notation of (b). (d) Dataset shown in (c) expanded to 100 K. R_{xx} exhibits metallic temperature dependence above T ~ 50 K, which also becomes magnetic field independent.

Figure 4-8(b) plots the resulting H_s - T diagram. H_s reaches a minimum of 0.016 T near T_C. The onset of a hysteresis loop leads to a small increase of H_s with decreasing temperature at T < T_C. Remarkably, at low temperature, H_s is only 0.043 T in MnSb$_{1.8}$Bi$_{0.2}$Te$_4$, in comparison to 0.42 T in MnSb$_2$Te$_4$ (Figure 4-9) and more than 7 T in MnBi$_2$Te$_4$ (Figure 4-10), despite similar ordering temperatures of ~ 20 K in all three materials. This observation strongly attests to the FM order in MnSb$_{1.8}$Bi$_{0.2}$Te$_4$. The small H_s here is associated with the alignment of the FM domains in an external field, rather than the spin-flop transition of individual Mn moment. In addition, we see that the anomalous Hall effect extends into the paramagnetic phase (open circles in Figure 4-8(a)), indicating FM fluctuations are already important at $T \geq T_C$.

Next, we demonstrate the impact of magnetic order on the transport characteristics of MnSb$_{1.8}$Bi$_{0.2}$Te$_4$. Figure 4-8(c) plots $R_{xx}(T)$ traces taken at a series of fixed magnetic fields. We track the sign change of dR/dT as a function of T and H and plot the results on a H - T map, similar to the H_s - T diagram shown in Figure 4-8(b). At temperatures above ~50 K, $R_{xx}(T)$ exhibits the expected metallic T-dependence, i.e. $dR/dT > 0$, without H-dependence. An expanded $R_{xx}(T)$ from 2 K to 100 K is given in Figure 4-8(d). As T approaches T_C , strong spin fluctuations lead to a slightly insulating T-dependence, i.e. $dR/dT < 0$, similar to the situation in MnBi$_2$Te$_4$ [92]. A positive dR/dT is found again when the moments align spontaneously or under a sufficiently large external field, likely

due to the reduction of magnetic scatterings that involve a spin-flip/flop. The onset of another insulator-like regime at $T < 12$ K coincides with the drop of χ in Figure 4-7, and the onset of an excess anomalous Hall signal in Figure 4-12. We are working to understand its origin.
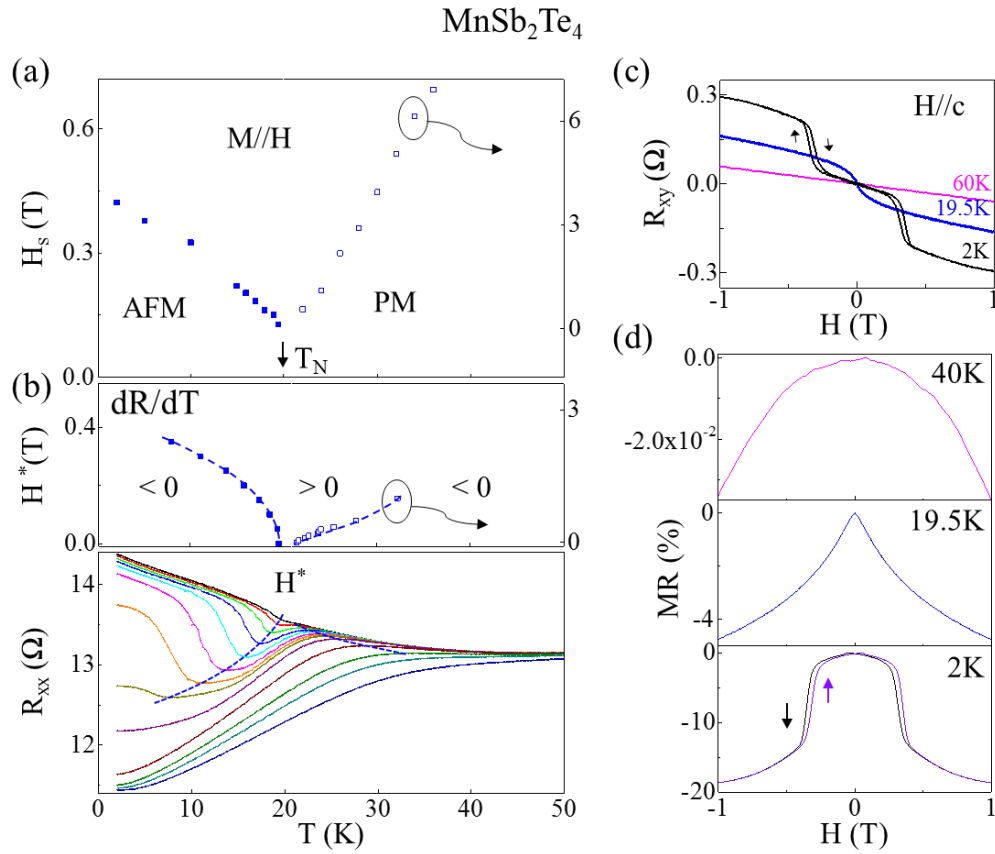
Figure 4-9. Characteristics of a MnSb$_2$Te$_4$ device.
The notations of the figures follow Figure 4-8 of MnSb$_{1.8}$Bi$_{0.2}$Te$_4$. As the H_s - T diagram in (a) shows, the saturation field is 0.42 T in MnSb$_2$Te$_4$, compared to 0.04 T in MnSb$_{1.8}$Bi$_{0.2}$Te$_4$ (Figure 4-8) and more than 7 T in MnBi$_2$Te$_4$ (Figure 4-10). The two orders of magnitude variation in H_s point to very different magnetic order in these three materials.
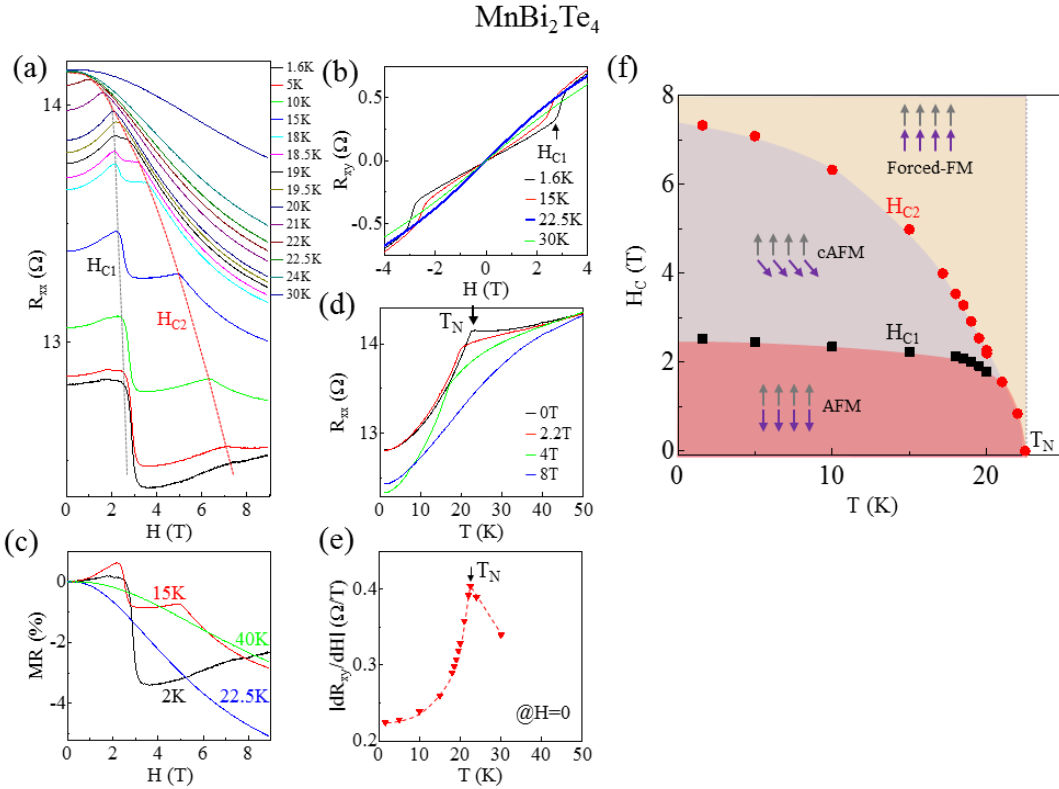
MnBi$_2$Te$_4$

Figure 4-10. Characteristics of a MnBi$_2$Te$_4$ device.

Data obtained on our MnBi$_2$Te$_4$ devices exfoliated from crystals grown in Ref. [92]. Our data are in very good agreement with results obtained by other groups on this material [83, 85, 92]. Magnetoresistance R_{xx} (H) (a) and Hall resistance R_{xy} (H) (b) at selected temperatures as labeled in the plots. A spin-flop transition is seen at H_{C1}, where both R_{xx} and R_{xy} undergo an abrupt jump. A second kink is seen at H_{C2}, which initiates a rapid drop of R_{xx}. (c) Normalized MR at selected temperatures. (d) The T-dependent R_{xx} at selected fields. A cusp is visible in the black, red and green traces when the system is in an AFM or canted AFM phase. It disappears after the moments are aligned with the external field. (e) plots the low-field slope dR_{xy}/dH obtained from the Hall resistance data. It strongly resembles magnetic susceptibility measured on bulk crystals by us and others. A cusp is seen at the Neel temperature T_N =22.5 K. (f) plots the phase diagram extracted from the data in (a). H//c in all measurements.

Figure 4-11 plots the normalized magnetoresistance (MR) of a MnSb$_{1.8}$Bi$_{0.2}$Te$_4$ device at selected temperatures. In MnSb$_{1.8}$Bi$_{0.2}$Te$_4$, MR is always negative. Its

magnitude increases with decreasing temperature and becomes hysteretic with the onset of the FM order. Alignment of all moments in an external field results in a large reduction of nearly 20% at low temperature. Comparing to similar measurements on $MnSb_2Te_4$ and $MnBi_2Te_4$ (Figure 4-4 and Figure 4-5), we see that electrical transport in Sb-rich compositions are much more influenced by the magnetic order, likely because the Mn orbitals are located in the valence band and couple more closely to the hole carriers in $MnSb_{1.8}Bi_{0.2}Te_4$ and $MnSb_2Te_4$ [93, 201].
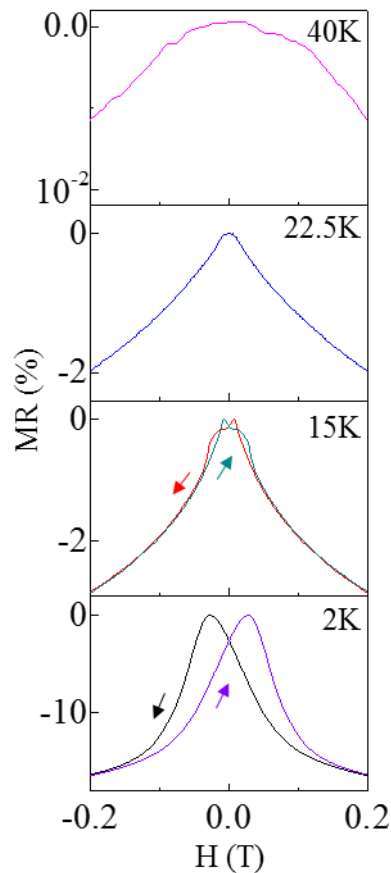
Figure 4-11. Normalized magnetoresistance at selected temperatures.
Normalized magnetoresistance MR = $[R_{xx}(H) - R_{xx}(0)]/R_{xx}(0) \times 100\%$. Arrows indicate field sweep direction. Note the change of the y-scale in different panels.

4.6 Excess Anomalous Hall Effect

Finally, we report on the appearance of an excess anomalous Hall signal in $MnSb_{1.8}Bi_{0.2}Te_4$ that is beyond the conventional AHE. This signal concentrates in the circled areas in the $\Delta R_{xy}(H)$ plot shown in Figure 4-8(a). Following the literature [195, 197, 198], we fit the conventional AHE component R_{xy}^{A} with a Langevin function (magenta dashed line in Figure 4-12(a)) and use R_{xy}^{T} to denote the excess signal (green shaded area). Figure 4-12(b) and (c) plot $R_{xy}^{T}(H)$ obtained at several temperatures and different tilt angles of the external field respectively. The raw $\Delta R_{xy}(H)$ plots are given in Figure 4-12(e). The magnitude of $R_{xy}^{T}(H)$ decreases rapidly with increasing temperature and vanishes at $T > 10$ K. The signal peaks at $H \sim \pm 0.7$ T and persists to several Tesla. Figure 4-12(d) plots the angle dependence of the peak value R_{peak}^{T}. $R_{peak}^{T}(\theta)$ is non-monotonic and reaches a maximum of 0.1 Ω around $\theta \sim 60°$. The value corresponds to a fictitious field of $H_{eff} = R_{peak}^{T} \cdot ne \sim 1$ Tesla, i.e. the excess anomalous Hall signal in our $MnSb_{1.8}Bi_{0.2}Te_4$ sample has considerable strength.

This intriguing excess anomalous Hall signal points to excess Berry curvature of the material, which disappears with increasing magnetic field. The room temperature crystal structure of $Mn(Sb, Bi)_2Te_4$ is centrosymmetric, which does not allow for a Dzyaloshinskii-Moria interaction (DMI) term in the Hall effect [188-193]. We have not identified a clear symmetry-lowering structural transition at low temperatures though this possibility cannot be ruled out. Excess Berry curvature can also occur in systems with non-colinear, frustrated, or spatially modulated magnetic textures such as clustered spin glass, frustrated magnets or non-colinear AFMs [212-214]. Our refinement analysis has

revealed considerable Mn-Sb site mixing. The second magnetic sublattice produced by Mn occupying the Sb sites could conceivably play a role in generating a non-colinear magnetic structure. Our ongoing work seeks to further examine this possibility.
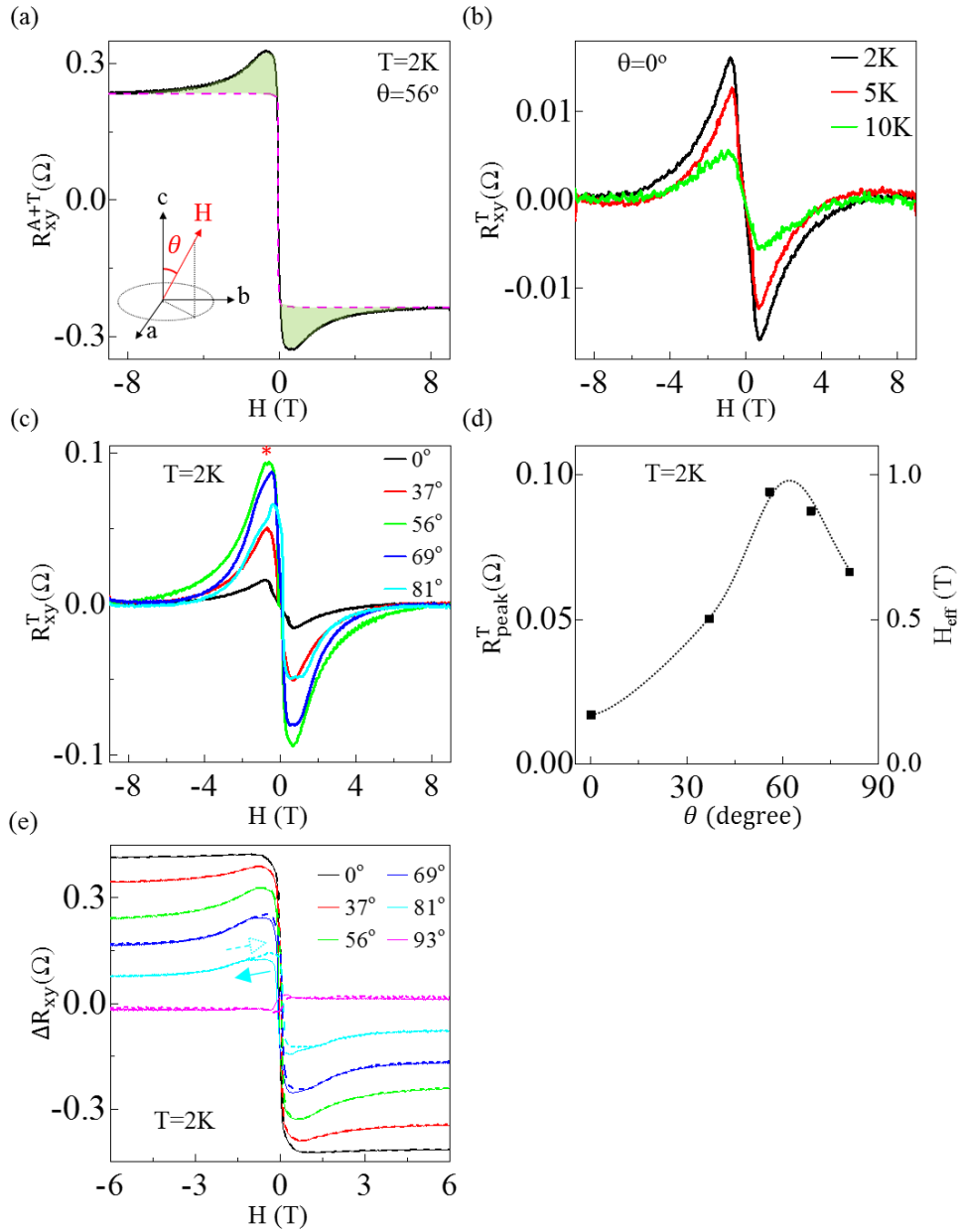
Figure 4-12. The Excess anomalous Hall effect in MnSb$_{1.8}$Bi$_{0.2}$Te$_4$.

(a) $R_{xy}^{A+T}(H)$, which is the same as $\Delta R_{xy}(H)$ in Figure 4-8(a) at $T = 2$ K and with a tilt angle $\theta = 56°$ as illustrated in the inset. The magenta dashed line is a Langevin fit to the anomalous Hall effect with an uncertainty of 0.9 mΩ. The area shaded in green indicates the excess Hall effect contribution R_{xy}^{T}. (b) $R_{xy}^{T}(H)$ at $\theta = 0°$ and $T = 2, 5,$ and 10 K. Data obtained from up and down sweeps are shifted horizontally to coincide at $H = 0$. (c) $R_{xy}^{T}(H)$ at $T = 2$ K and selected tilt angle θ. R_{peak}^{T} is marked by the * symbol. (d) The angular dependence of R_{peak}^{T} at $T = 2$ K. The right axis labels the effective magnetic field $H_{eff} = R_{peak}^{T}/R_0$. (e) Raw data $\Delta R_{xy}(H)$ of the MnSb$_{1.8}$Bi$_{0.2}$Te$_4$ device shown in (c). Solid and dashed lines correspond to down and upsweeps respectively. $T = 2$ K.

4.7 Evidence of Ferromagnetism in Neutron Scattering Data

Figure 4-13 compare neutron scattering results obtained on our MnSb$_{1.8}$Bi$_{0.2}$Te$_4$ and MnSb$_2$Te$_4$ single crystals. Upon cooling, the (*1 0 1*) and (*1 0 4*) nuclear reflection peaks in MnSb$_{1.8}$Bi$_{0.2}$Te$_4$ gained intensity with no peak appearing at the (*1 0 2.5*) position (Figure 4-13(c)). In contrast, the (*1 0 2.5*) peak appeared at low temperatures in our MnSb$_2$Te$_4$ sample while the amplitude of the nuclear reflections remained unchanged (Figure 4-13(d)). The (*1 0 2.5*) peak is associated with the development of the A-type AFM phase in MnBi$_2$Te$_4$ in previous reports [92, 94]. The neutron data clearly indicate a different magnetic order in our samples, that is, AFM in MnSb$_2$Te$_4$ and FM in MnSb$_{1.8}$Bi$_{0.2}$Te$_4$. Mean-field fits to the temperature-dependent scattering amplitude at the (*1 0 1*) and (*1 0 2.5*) positions yield a Curie temperature of $T_C \sim 26$ K and a Néel temperature of $T_N \sim 20$ K for the MnSb$_{1.8}$Bi$_{0.2}$Te$_4$ and MnSb$_2$Te$_4$ samples respectively. Further, we show in Figure 4-7 the low-field slope dR_{xy}/dH we obtained on a MnSb$_2$Te$_4$ device (solid blue squares). It is consistent with an AFM phase with $T_N \sim 19.5$ K, and is in excellent agreement with previous susceptibility measurements of this material [93].
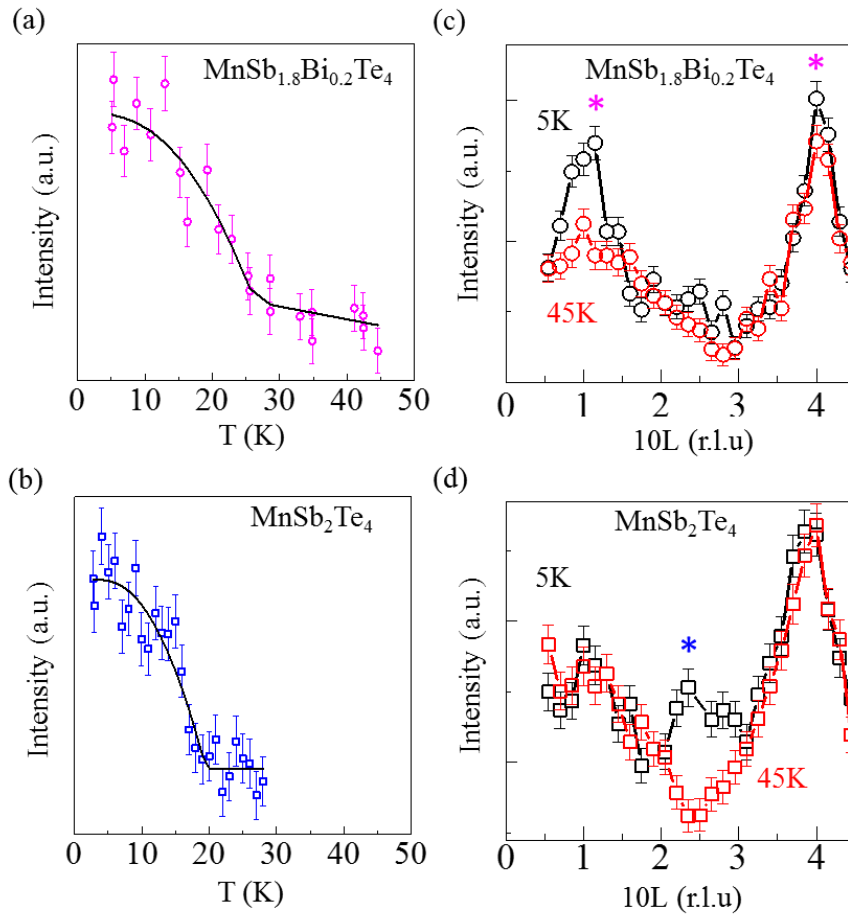
Figure 4-13. Elastic neutron scattering in $MnSb_{1.8}Bi_{0.2}Te_4$ and $MnSb_2Te_4$.
(a) and (b) show the temperature-dependent elastic neutron scattering centered at the (*1 0 1*) reflection in $MnSb_{1.8}Bi_{0.2}Te_4$ (a) and the (*1 0 2.5*) reflection in $MnSb_2Te_4$ (b). Mean-field fits (solid lines) yield T_c = 26.3 K in (a) and T_N = 19.5 K in (b). (c) and (d) show scans along the (*1 0 L*) direction at 5 K and 45 K in the two materials with the * symbol marking the (*1 0 1*), (*1 0 4*) reflections in (c) and the (*1 0 2.5*) reflection in (d). Error bars in (a) ~ (d) represent one standard deviation. Data and figures are from our collaborators Heikes et al. at NIST [206].

4.8 Discussion about the Origin of Ferromagnetism in our

$MnSb_{1.8}Bi_{0.2}Te_4$ Samples

The FM and AFM order we identified in our $MnSb_{1.8}Bi_{0.2}Te_4$ and $MnSb_2Te_4$ crystals respectively, the literature results of mostly AFM order in the majority of the Mn(Bi, Sb)$_2$Te$_4$ crystals synthesized[83, 85, 92, 93, 201], and a very recent report of a ferrimagnetic ground state with Tc ~ 25 K in polycrystalline $MnSb_2Te_4$ by Murakami et al [204], all together paint a much more nuanced picture than anticipated from initial calculations of this compound family. The intrinsic AFM or FM coupling between adjacent Mn layers compete closely in energy in Sb-rich compositions [93, 201]. In their work, Murakami et al showed that site mixing between Mn and Sb sites can alter the interlayer Mn-Mn exchange coupling from AFM to FM via a ferrimagnetic configuration that aligns Mn moment occupying the Sb site in the opposite direction. Through the x-ray and NPD data, we have also found a considerable amount of anti-site defects in our $MnSb_{1.8}Bi_{0.2}Te_4$ and $MnSb_2Te_4$ samples, with approximately 41(1) % and 26(1) % of Mn occupying nominal (Bi,Sb) sites in $MnSb_2Te_4$ and $MnSb_{1.8}Bi_{0.2}Te_4$ respectively. The small amount of Bi seems to suppress the presence of the anti-site defects, consistent with their absence and the universal AFM ground state found in the end compound $MnBi_2Te_4$[94].

In the literature, Mn-doped Bi_2Te_3 is known to have a FM ground state [215-217]. Samples studied here are screened by XRD to have less than 5% intergrowth of the (Sb,Bi)$_2$Te$_3$ phase. In addition, we have explicitly tested the behavior of a flake exfoliated from a crystal with significant secondary Bi_2Te_3 intergrowth. The results are presented in Figure 4-14. This device exhibits a Curie temperature of Tc ~ 11 K and its transport and

magneto-transport behavior closely resembles that of Mn-doped Bi_2Te_3 [215-217], but are very different from that of the $MnSb_{1.8}Bi_{0.2}Te_4$ and $MnSb_2Te_4$ devices. No excess anomalous Hall signal was observed (Excess anomalous Hall signal is discussed in Figure 4-12). These results indicate that the possibility of a FM state originating solely from ferromagnetic coupling of Mn occupying the Sb site can be ruled out.
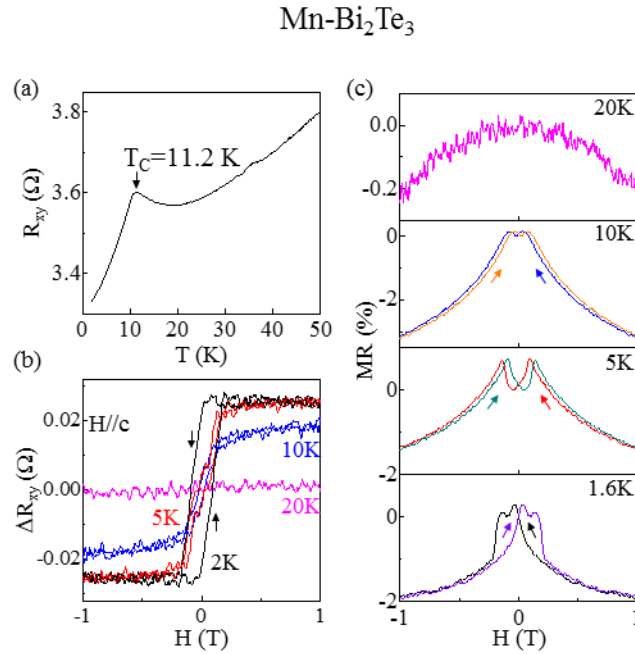
Figure 4-14. Characteristics of a Mn-doped Bi_2Te_3 device.
(a) The temperature dependence of R_{xx} at H=0. (b) ΔR_{xy} (H) at selected temperatures as labeled in the plot. Arrows indicate the field sweep direction. The presence of hysteresis loops supports a FM phase at T < T_c, consistent with literature results. No excessive anomalous Hall signal was observed in this device. Carriers are electrons. (c) Normalized magnetoresistance (MR) at selected temperatures. At low magnetic field and low temperature, the MR exhibits weak anti-localization effect characteristic of Bi_2Te_3. The magnitude of the MR is roughly ten times smaller than that of $MnSb_{1.8}Bi_{0.2}Te_4$ and $MnSb_2Te_4$.

The different magnetic orders exhibited by our samples and others' highlight the sensitivity of the magnetic interactions of the system to the details of the local defect chemistry. As described in the methods section, we are able to grow $MnSb_{1.8}Bi_{0.2}Te_4$ crystals that are either FM or AFM using different thermal treatments before quenching, which could conceivably lead to different local defect chemistry that supports different magnetic orders. Further understanding of this process and the identification of synthesis conditions that lead to FM order in a wide range of alloy compositions will be an important goal of future studies.

4.9 Conclusion

In summary, we combine electrical transport, bulk magnetometry and neutron diffraction studies to show evidence of a ferromagnetic ground state with a Curie temperature of 26 K in $MnSb_{1.8}Bi_{0.2}Te_4$. Our work is an encouraging step towards realizing a ferromagnetic topological insulator. Based on a recent work [86], ferromagnetism is preferable because ferromagnetic order can stabilize QAHE against thermal fluctuations and realize QAHE at a higher temperature. The vdW geometry of $Mn(Sb, Bi)_2Te_4$ family opens up possibilities of forming heterostructures and gating tuning. Studies that illuminate the synthesis conditions of different magnetic phases in the $Mn(Sb, Bi)_2Te_4$ family will greatly facilitate future explorations of their topological and magnetic properties.

Chapter 5

Piezoelectric Substrate for 2D Materials

Strain is a powerful tool to tune properties sensitive to the lattice constants, including electronic, optical, and magnetic properties [35-42, 218, 219]. External strain can be applied through various methods such as nanoindentation [44, 45], mechanical stretching [27], change of pressure around suspended material [220], and nanopillars [221]. But to incorporate strain tuning ability with our cryostat and experimental setup, we choose using piezoelectric substrate as the strain tuning method. Strain can be applied to 2D materials in a convenient and precise way through an electric field. This is also a time-saving method to apply strain as the substrate can be fabricated with a large wafer, say 4" wafer, and then be cleaved into the size we need.

This chapter will start by introducing mathematical description of strain and lead zirconate titanate, a widely used ferroelectric material. Then we will talk about the fabrication and calibration of our piezoelectric substrate.

5.1 Introduction to Strain, Piezoelectricity, and Lead Zirconate Titanate

5.1.1 Strain tensor and piezoelectric coefficients

Figure 5-1(a) shows the geometry of deformation. The mathematical expression of the reference location x, displacement vector u(x), and deformed location y(x) is as following [222]:

$$x = x_1 e_1 + x_2 e_2 + x_3 e_3 \tag{5-1}$$

$$\boldsymbol{u}(\boldsymbol{x}) = u_1\boldsymbol{e_1} + u_2\boldsymbol{e_2} + u_3\boldsymbol{e_3}$$

$$\boldsymbol{y}(\boldsymbol{x}) = \boldsymbol{x} + \boldsymbol{u}(\boldsymbol{x}) = (x_1 + u_1)\boldsymbol{e_1} + (x_2 + u_2)\boldsymbol{e_2} + (x_3 + u_3)\boldsymbol{e_3}$$
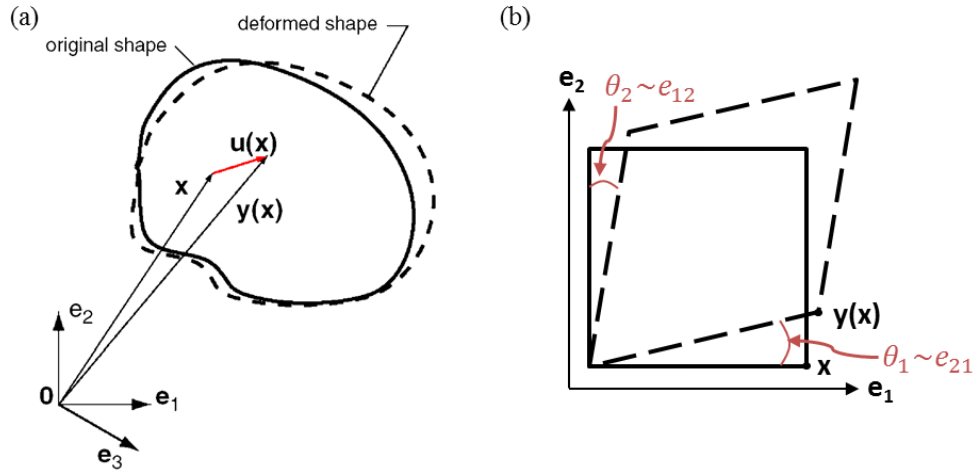
Figure 5-1. Geometry of deformation from original shape (solid line) to deformed shape (dashed line). x and y(x) are the position vectors of reference location in original shape and deformed location, respectively. u(x) is the displacement vector.
(Figure in (a) is taken from David Parks's lecture note [222]. Figure in (b) is adapted from Ref. [223].)

When we look at the displacement of nearby points and do Tyler expansion, we get

$$u_i(\boldsymbol{x} + \Delta\boldsymbol{x}) = u_i(\boldsymbol{x}) + \sum_{j=1}^{3} \frac{\partial u_i}{\partial x_j}\Delta x_j$$

(5-2)

$$\Delta u_i = u_i(\boldsymbol{x} + \Delta\boldsymbol{x}) - u_i(\boldsymbol{x}) = \sum_{j=1}^{3} \frac{\partial u_i}{\partial x_j}\Delta x_j$$

The displacement gradient tensor e_{ij} is defined as following:

$$e_{ij} \equiv \left[\frac{\partial u_i}{\partial x_j}\right] = \begin{bmatrix} \dfrac{\partial u_1}{\partial x_1} & \dfrac{\partial u_1}{\partial x_2} & \dfrac{\partial u_1}{\partial x_3} \\[2mm] \dfrac{\partial u_2}{\partial x_1} & \dfrac{\partial u_2}{\partial x_2} & \dfrac{\partial u_2}{\partial x_3} \\[2mm] \dfrac{\partial u_3}{\partial x_1} & \dfrac{\partial u_3}{\partial x_2} & \dfrac{\partial u_3}{\partial x_3} \end{bmatrix} \tag{5-3}$$

The diagonal components of the tensor, $\frac{\partial u_i}{\partial x_i}$, is the fractional change in length along x_i direction, which is also called extensional strain. To understand $\frac{\partial u_i}{\partial x_j}$, it is easier to start from a classic example plotted in Figure 5-1(b): a square deformed into a parallelogram. When Δu is small, $\frac{\partial u_2}{\partial x_1} = tan\theta_1 \sim \theta_1$ and $\frac{\partial u_1}{\partial x_2} = tan\theta_2 \sim \theta_2$. $\theta_1 + \theta_2 = \frac{\partial u_2}{\partial x_1} + \frac{\partial u_1}{\partial x_2}$ are the total reduction in the angle between the originally perpendicular line segments. Similar result applies to any pair of axes. Cartesian components of the (small) strain tensor is defined as

$$\varepsilon_{ij} \equiv \frac{1}{2}\left(\frac{\partial u_i}{\partial x_j} + \frac{\partial u_j}{\partial x_i}\right) \tag{5-4}$$

Strain tensor is symmetric. The diagonal components $\varepsilon_{ii} = \frac{\partial u_i}{\partial x_i}$ are extensional strains along x_i direction. The off-diagonal components ε_{ij} are half of the total reduction in the angle between a line segment pair originally parallel to x_i and x_j axes.

The relation between strain ε_{ij} and external electric field E_k in piezoelectric materials can be described by

$$\varepsilon_{ij} = d_{kij}E_k \tag{5-5}$$

where d_{kij} (CN^{-1}) is a third-rank tensor of piezoelectric coefficients. It is common to call a piezoelectric coefficient measured along the direction of applied field the longitudinal coefficient, and that measured in a direction perpendicular to applied field the transverse coefficient. The other piezoelectric coefficients are shear coefficients. Whether a crystal can have piezoelectricity depends on its crystal symmetry. For example, piezoelectric coefficients are zero and piezoelectric effect is absent in all 11 centrosymmetric point groups.

Because strain and stress are symmetric tensors, piezoelectric coefficients with the same first index are the same: $d_{kij} = d_{kji}$ [224]. To simplify notation, piezoelectric coefficients can be written in the Voigt convention as the following. A pair of indices ii = 11, 22, 33 is replaced with the single index m = 1, 2, 3, respectively. A pair of mixed indices ij = 23 or 32, 13 or 31, 12 or 21 is represented with m = 4, 5, 6, respectively. And equation (5-5) becomes

$$\varepsilon_m = d_{im}E_i \qquad (5\text{-}6)$$

where i = 1, 2, 3 and m = 1, 2, …, 6. Note that the matrices in reduced form do not transform as tensors because the coordinate system is changed.
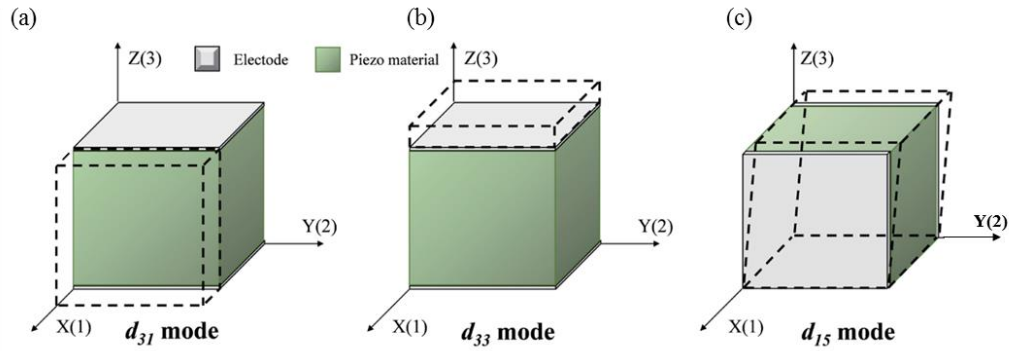
Figure 5-2. The three operating modes of piezoelectric materials.
The dashed lines illustrate how the material deform in the corresponding modes. In both (a) and (b), external electric field is applied along Z direction. d_{31} and d_{33} modes represent the deformation along X and Z axes, respectively. (c) d_{15} shear mode. The external electric field is applied along X direction. (Figure adpated from Y-C Chen et al. [225].)

The transverse, longitudinal and shear modes are characterized by piezoelectric coefficients d_{31}, d_{33} and d_{15}, respectively (Figure 5-2). Polarization is either parallel or anti-parallel to electric field in d_{31} and d_{33} modes, pointing in Z direction. Polarization (Z direction) is perpendicular to the electric field (X direction) in d_{15} mode [226].

5.1.2 Piezoelectric, pyroelectric, and ferroelectric crystals

Piezoelectricity is the ability to develop an electric charge proportional to external stress, which is also called *direct* piezoelectric effect [224, 227]. Piezoelectric materials must also have the *converse* piezoelectric effect: when being applied an external electric field, crystal deforms and the strain is linear to the applied field.

Some piezoelectric crystals, called pyroelectric, can have electric dipole moment without an external electric field. Such dipole moment is associated with a spontaneous polarization, which can only occur in materials with a unique polar axis.

Ferroelectric crystals are pyroelectric crystals whose electric polarization can be switched by an external electric field. Figure 5-3(a) illustrates the relation between ferroelectric, pyroelectric and piezoelectric materials. Most ferroelectric materials undergo a phase transition from a high-temperature non-ferroelectric phase to a low-temperature ferroelectric phase. The phase transition temperature into a ferroelectric phase is called Curie point or Curie temperature.

The interest in ferroelectric crystals starts from the fact that many ferroelectric crystals have high piezoelectric coefficients and they may be prepared in a polycrystalline form. The benefit of polycrystalline preparation is that its composition may be easier to adjust than when preparing single crystals, so materials with a wide range of properties may be obtained. Lead zirconate titanate ($Pb(Zr_xTi_{1-x})O_3$ or PZT) is an example. It is a solid solution of lead zirconate ($PbZrO_3$ or PZ) and lead titanate ($PbTiO_3$ or PT), which are soluble in all proportions.
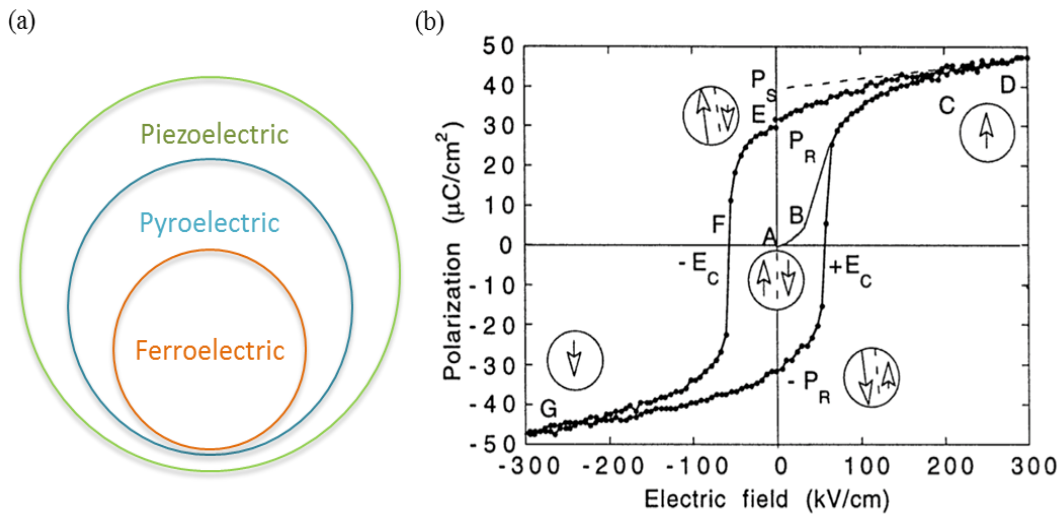
Figure 5-3. Relation between ferroelectric, pyroelectric, piezoelectric crystals, and P-E loop. (a) Relation between ferroelectric, pyroelectric and piezoelectric crystals. All ferroelectric crystals are pyroelectric, but only part of pyroelectric crystals are

ferroelectric. Similarly all pyroelectric crystals are piezoelectric, but only part of piezoelectric crystals are pyroelectric. (b) Typical P-E hysteresis loop of a ferroelectric crystal. This plot shows the hysteresis loop of a (111)-oriented 1.3 μm thick sol-gel $Pb(Zr_{0.45}Ti_{0.55})O_3$ film. P_S ,P_R, and E_C are saturation polarization, remnant polarization, and coercive field, respectively. Arrows in each circle represent the polarization status at the indicated fields. (Figure adapted from Damjanovic et al. [224].)

One key property of a ferroelectric crystal is that its polarization can be switched by an external electric field, which manifests in the polarization versus electric field (P-E) hysteresis loop. Figure 5-3(b) shows the P-E loop of a PZT film. The loop starts from the origin and sweeps to positive field. In segment AB, the field is not strong enough to switch the unfavorable polarization and the polarization increases linearly with the field. As the field increases, domains with unfavorable polarization starts to switch and the polarization grows nonlinearly with the field (segment BC). Once all the domains are switched, the polarization increases linearly with electric field (segment CD). The field is then swept downward and the polarization starts to back-switch. At zero field, there is a nonzero polarization, which is called remnant polarization P_R. The field needed to bring electric field back to zero is called coercive field E_C. As the field continues to increase in the negative direction, the domains are back-switched completely and the polarization saturates (point G). The field is then reduced and go back up to complete the loop. In polycrystalline materials, spontaneous polarization in single crystals cannot be achieved. So it is more correct to call P_S the "saturation" polarization instead of spontaneous polarization. P_S is usually obtained by the intercept of extrapolated linear segment CD. It should be mentioned that the coercive field is not an absolute threshold field to flip the

polarizations. If a low electric field is applied to the ferroelectric material for a (very) long time, the polarizations will be switched eventually [224, 228].

5.1.3 Introduction to lead zirconate titanate (PZT)

PZT is a ferroelectric / pyroelectric / piezoelectric polycrystalline ceramic. It has most of the properties of ceramics, namely a high elastic modulus, high brittleness, and low tensile strength [229]. PZT is a widely used piezoelectric ceramic material with a large piezoelectric effect, high strength, and wide temperature stability [227]. It has a perovskite crystal structure, which is shown in Figure 5-4.
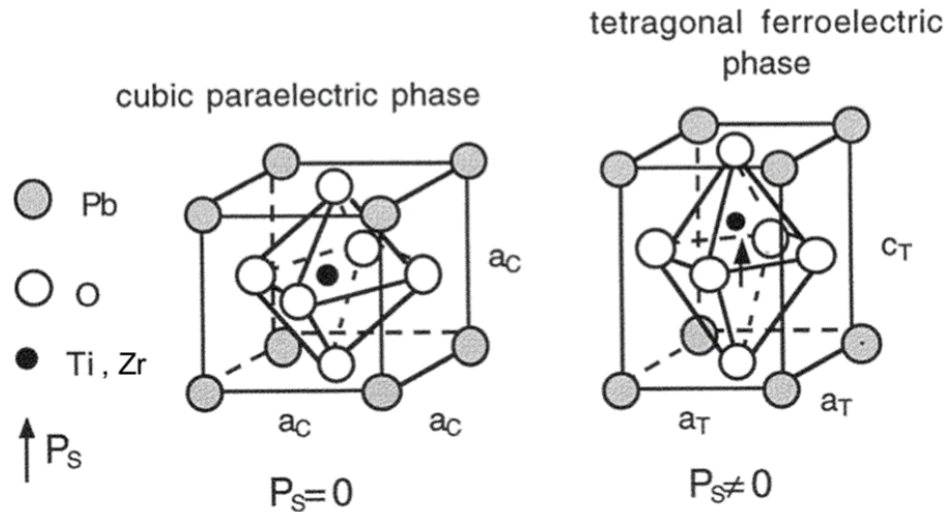
Figure 5-4. The perovskite structure ABO_3, shown here for PZT.
PZT has a cubic structure in paraelectric phase and tetragonal structure in ferroelectric phase. a_C denotes the lattice constant of the cubic structure. a_T and c_T are the lattice constants of the tetragonal structure. P_S is the spontaneous polarization. (Figure adapted from Damjanovic et al. [224].)
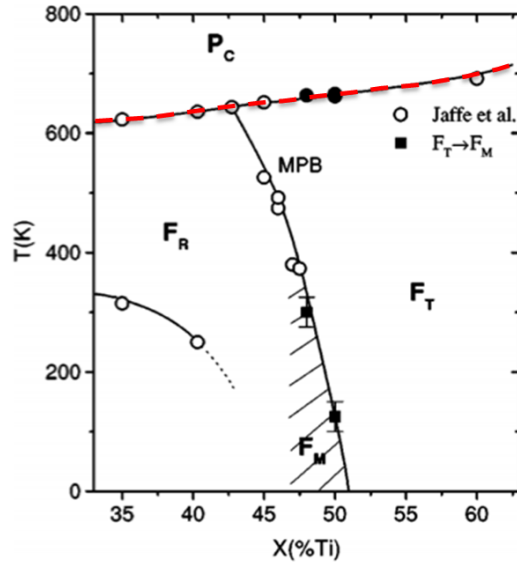
Figure 5-5. Phase diagram of $PbZrO_3$-$PbTiO_3$ system.
The X axis is the percentage of Zr^{4+} replaced by Ti^{4+} in $PbZrO_3$. P_C: paraelectric cubic, F_R: ferroelectric rhombohedral, F_T: ferroelectric tetragonal, and F_M: ferroelectric monoclinic. Red dashed line denotes the Curie temperature T_C below which ferroelectric phase occurs. MPB is the morphotropic phase boundary. (Figure adapted from Jaffe et al. [230] and Noheda et al. [231].)

Figure 5-5 plots the phase diagram of $PbZrO_3$-$PbTiO_3$ system. Zr and Ti are randomly distributed in the B sites of ABO_3 structure shown in Figure 5-4 [224]. Titanium-rich compositions transform into rhombohedral perovskite structure below Curie temperature T_C. Zirconium-rich compositions have more complex phases, but below T_C most compositions are ferroelectric. The morphotropic phase boundary (MPB) is where PZT transforms from tetragonal to rhombohedral or monoclinic structure, and two phases coexist at the boundary.

Composition of PZT which is widely used in high performance actuator is near MPB. At MPB, there are more polarization states available from the two energy equivalent states, tetragonal and rhombohedral. Due to enhanced polarizability brought from two energy equivalent states, tetragonal and rhombohedral, the anisotropy energy is reduced,

domain wall energy decreases and thus domain wall mobility increases [232]. There are 6

energy-equivalent polar axes in tetragonal structure and 8 polar axes in rhombohedral

structure [224, 233]. At MPB, PZT has 6+8 available directions along which polarization

can be reoriented by the poling field. Thus PZT near MPB has its largest piezoelectric

effects, largest remnant polarization and lowest coercive field (can be easily poled) [230,

234, 235]. One thing worth noticing is that the MPB in PZT is almost vertical in the

diagram, which means a strong composition dependence and little dependence at

temperature. The ratio of Zr/Ti on MPB at room temperature is around 52/48.

Unpoled   During poling   After poling
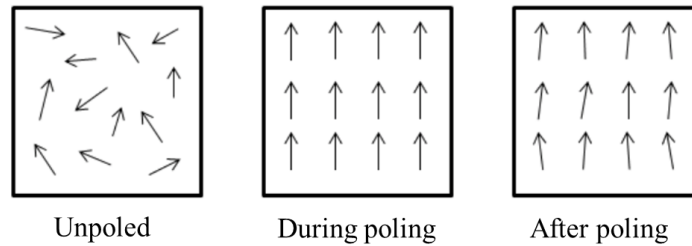
Figure 5-6. Schematic diagram of the poling process in piezoelectric ceramics.
An unpoled piezoelectric has random orientation of polarization. During poling, a high
electric field orients all dipole moments in the field direction. After the field is swept to
zero, most dipoles still more-or-less point to the field direction due to the pinning
produced by defects. (Figure taken from reference [236].)

Poling is to apply a DC electric field to orient ferroelectric domains and induce

piezoelectricity [227]. As one can see in the P-E hysteresis loop, PZT can sustain a non-

zero polarization even when the field is back to zero. But the polarization of PZT will not

stay there but relax. To sustain the polarization for long enough, the DC electric field

needs to be large enough and apply to the film for long enough. Before poling,

polycrystalline PZT has random grain orientation thus does not have any piezoelectric

effects (Figure 5-6). After poling, the film has a net polarization pointing to the applied field direction. It is noteworthy that a poled film can be de-poled if it is subjected to a strong electric field pointing to the direction opposite to its polarization or is exposed to a temperature higher than the Curie temperature [236]. If the film is poled along the z direction, it is isotropic in the xy plane as far as the piezoelectric coefficients are concerned. Therefore, $d_{31} = d_{32}$ and $d_{15} = d_{24}$ [229]. For bulk PZT(52/48), the piezoelectric coefficients are: d_{33} = 330 to 675 pm/V, d_{31} = -165 to -310 pm/V, and d_{15} = 850 to 920 pm/V [237, 238]. Piezoelectric coefficient d_{31} is most relevant to our experiment setup. The negative sign says that PZT shrinks in xy plane when being applied with an electric field pointing to the same direction as its poled direction along z axis.

5.2 Fabrication and Characterization of Piezoelectric Substrate

5.2.1 Preparation and characterization of PZT film

There are many methods to prepare PZT film, such as electron-beam evaporation [239], rf magnetron sputtering [240], and sol-gel processing [241]. In our work, we use sol-gel method because it is a well-established method in the lab of our collaborator, Dr. Susan Trolier-McKinstry's group. It has the advantage of better thin-film homogeneity, simpler composition control, lower synthesis temperature, and lower cost [242].

Our (100)-oriented PZT film is prepared with chemical solution spin-on process described in the paper of Welsh et al. [243]. The preparation of PZT solutions was described in detail by Wolf and Trolier-McKinstry [241]. The spin-on process starts from

a PbTiO$_3$ seed layer spin coating with 0.15M PbTiO$_3$ solution, which is followed by a 1-minute RTA at 550°C in oxygen. Then the repetition of PZT spin coating starts. 0.4M PZT 52/48 solution with 10 % excess Pb is spun at 3000rpm, which is followed by a two-step pyrolysis: 225°C for 2 minutes and 400°C for 2 minutes. The film is then crystalized at 700°C for 1 minute in oxygen in a Modular Process Technology Corporation (San Jose, CA) RTP-600S Rapid Thermal Annealing Furnace. The process is repeated until the desired film thickness is reached. Finally 0.08M PbO solution is spun on the PZT film for lead replenishment.

Figure 5-7 shows the characterization of our PZT 52/48 film on a PbTiO$_3$ seed layer and SiO$_2$/Si substrate. Our PZT film is 1.78 μm thick. Figure 5-7(a) shows that the film is (100) oriented. Figure 5-7(b) plots the P-E hysteresis loop of the PZT film. To contact the bottom electrode, part of PZT is etched with hydrochloric acid and hydrofluoric acid. Figure 5-7(c) plots the leakage current through the PZT film versus a vertical DC electric field. The leakage current starts to spike above ~50 kV/cm, which indicates that cracking starts. Cracking happens due to the stress caused by the piezoelectric deformation [244]. As the field increases, the spike shows up more frequently and the thermal breakdown happens around 210 kV/cm. In comparison to a good PZT film, our PZT film breaks down at a lower field. A good film can be poled at 3 times coercive field, which is about 150 kV/cm [237] and sustain field as high as 284 kV/cm for 20 hours at 150 ˚C [245]. We don't know what causes the low breakdown field in the fabrication process yet.

(a)

(b)

(c)
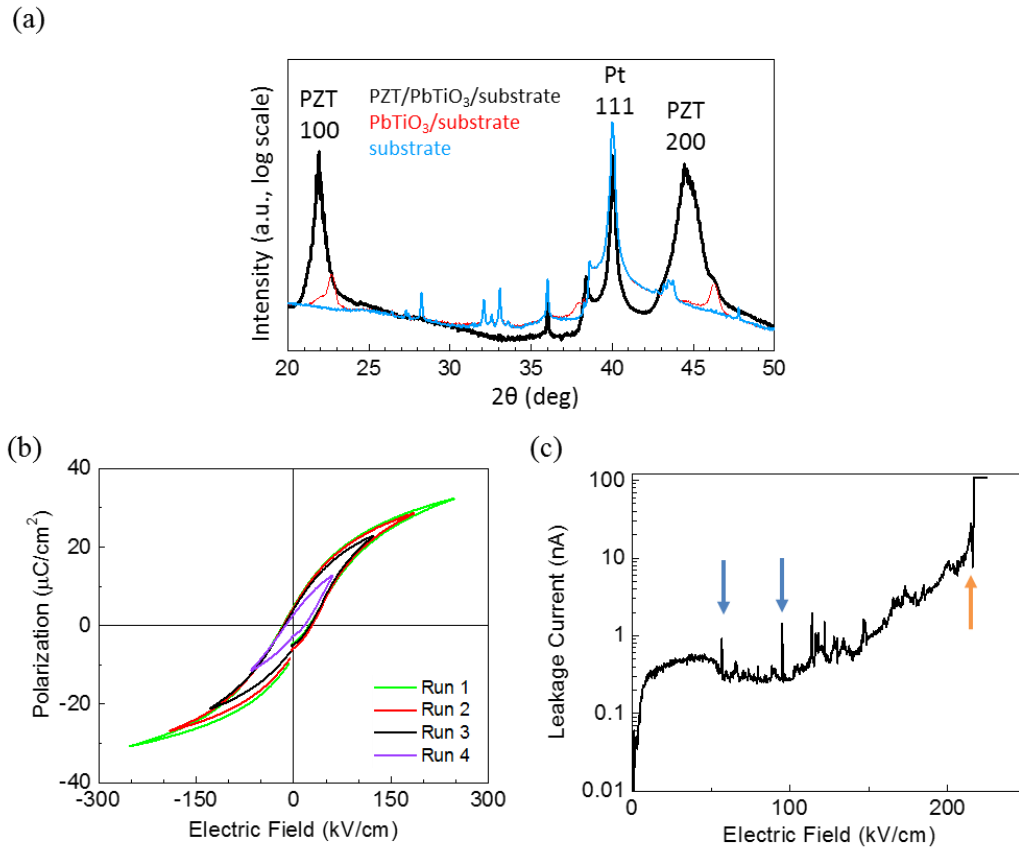
Figure 5-7. Characterization of our (100)-oriented PZT 52/48 film.
(a) XRD patterns of PZT film on PbTiO₃/substrate (black), PbTiO₃ on substrate (red), and substrate (blue). (b)P-E hysteresis loops of our unpoled PZT film. Each loop is measured within 10 ms and the loops are taken from run 1 (higher maximum electric field) to run 4 (lower maximum electric field). The film breaks down above ~250 kV/cm. (c) Leakage current through PZT film versus DC electric field applied across it. The film starts to crack above ~50 kV/cm and leakage current starts to spike (indicated by blue arrows). This film breaks down around 210 kV/cm (indicated by orange arrow).

5.2.2 Fabrication of a piezoelectric substrate
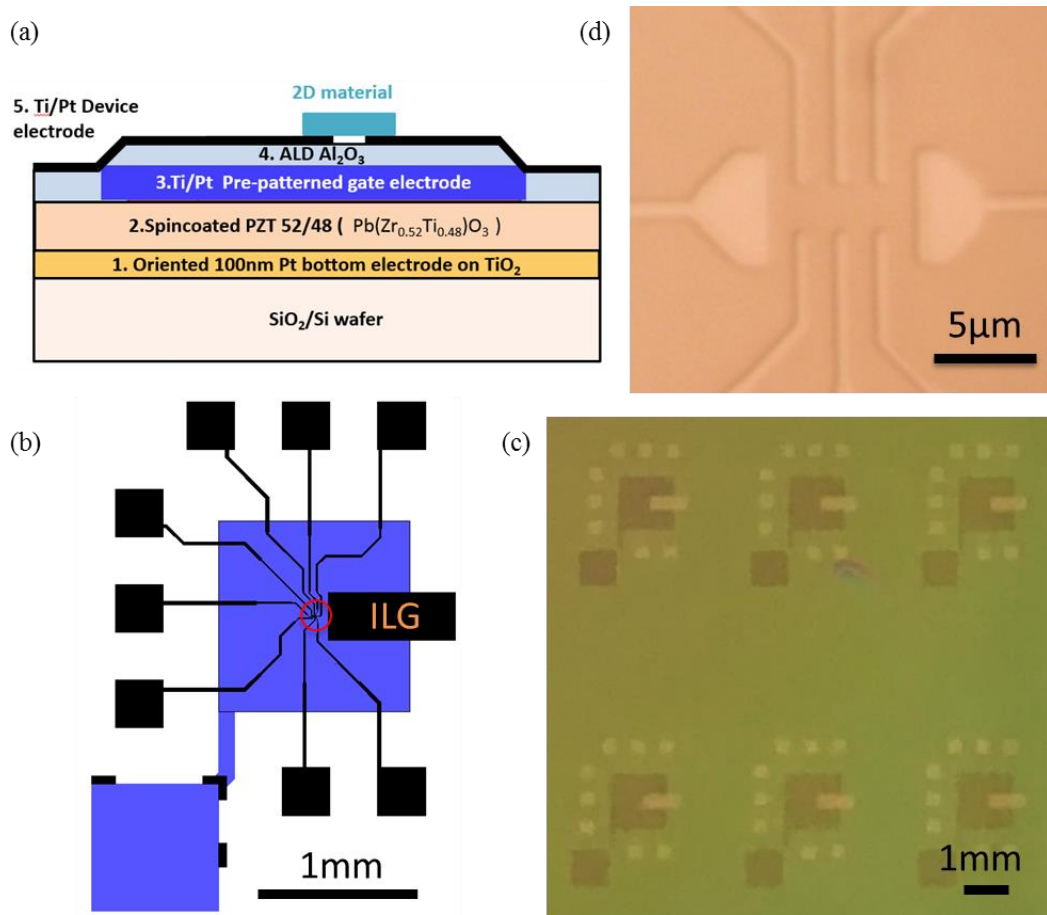
Figure 5-8. Schematics and optical images of our piezoelectric substrate.
(a) Schematics of our piezoelectric substrate. (b) Top view schematics of pre-patterned gate electrode (blue) and device electrodes (black). The red circle indicates where a 2D material flake would be placed. The rectangular pad labeled ILG is for ionic liquid gating. (c) Optical image of the piezoelectric substrate. Pre-patterned gate electrode and device electrodes appear red and gold, respectively. There are six sets of electrodes shown in this image. Each set of electrodes is one unit so this part of substrate can be cleaved into six substrates for six devices. (d) Magnified optical image of device electrodes, which corresponds to the circled area in (b).

Figure 5-8 shows the schematics and optical images of our piezoelectric substrate.

The fabrication method for our piezoelectric substrate is as the following:

1. (1) Firstly sputter 30 nm Ti on a 4" SiO_2/Si wafer from NOVA Electronic Materials. Then treat the wafer with RTA at 700 °C in oxygen for 15 minutes, after which Ti oxidizes. The TiO_2 layer helps orient the platinum sputtered on top.

   (2) Sputter 100 nm Pt at 600 °C. This is a layer of oriented platinum Pt(111), which helps orient the PZT spin coated on top.

2. Sol-gel process for PZT preparation: Spin coat ~2μm thick of 52/48 PZT following the method described in section 5.2.1

3. Pre-patterned gate electrodes are defined by optical lithography using LOR2A/3012 bilayer resist. Afterward develop the resist with CD26 and sputter 5 nm Ti / 15 nm Pt at room temperature.

4. Grow 30 nm Al_2O_3 with atomic layer deposition (ALD) at 200 °C.

5. Spin coat PMGI SF2/3012 bilayer resist. Then device electrodes are defined and aligned with gate electrodes by optical lithography. Afterward develop the resist with CD26. Treat the wafer with 10mW deep UV. Then deposit 2 nm Ti / 15 nm Pt with ebeam evaporation.

6. Cleave and etch: Cleave the wafer into small dices. Each dice with one pre-patterned gate electrode and one set of device electrodes can be made into one device. To make contact to the gate electrode and bottom electrode (layer 3 and 1 in Figure 5-8(a)), layers on top need to be removed. For contacting the gate electrode, 30nm Al_2O_3 above can be easily removed during soldering. On the other hand, hydrochloric acid and hydrofluoric acid are used in order to remove PZT and Al_2O_3 and expose the bottom electrode.

There was a problem we encountered at early stage of the substrate fabrication. In the fabrication method step 3, we used to deposit Ti/Pt by ebeam evaporation and then treat the substrate with RTA after the deposition. This process introduced islands (about 500 nm wide and 100 nm tall) on each gate electrode every 1~5 μm and 2D materials could not lie flat on such substrate (Figure 5-9). We suspect that these islands are formed by evaporated Pt during the RTA process. The substrate is free from the islands once we remove the RTA process from our substrate fabrication and sputter the gate electrodes instead of evaporation. The modified fabrication method is in section 5.2.1.
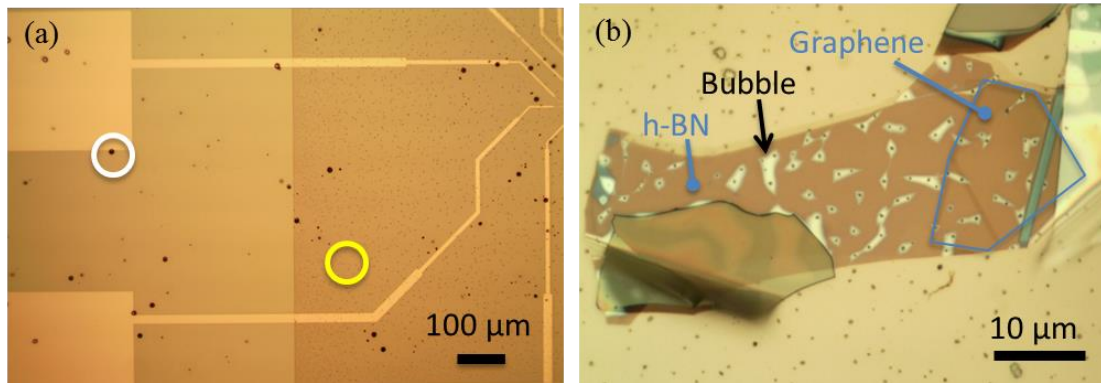
Figure 5-9. Optical images of piezoelectric substrate with islands.
(a) White and yellow circles indicate large islands on PZT (appear as large black dots) and small islands on pre-patterned gate electrodes (little grey dots). The large islands are in or on the PZT film and produced in the PZT spin coating process. They are about 10 μm wide and 1 μm tall. The small islands, which are about 500 nm wide and 100 nm tall, only form in the gate electrodes. We think the small islands are bulged evaporated platinum after rapid thermal annealing. (b) A stack of h-BN/graphene on the substrate with islands. Bubbles form between the stack and the substrate around the islands.
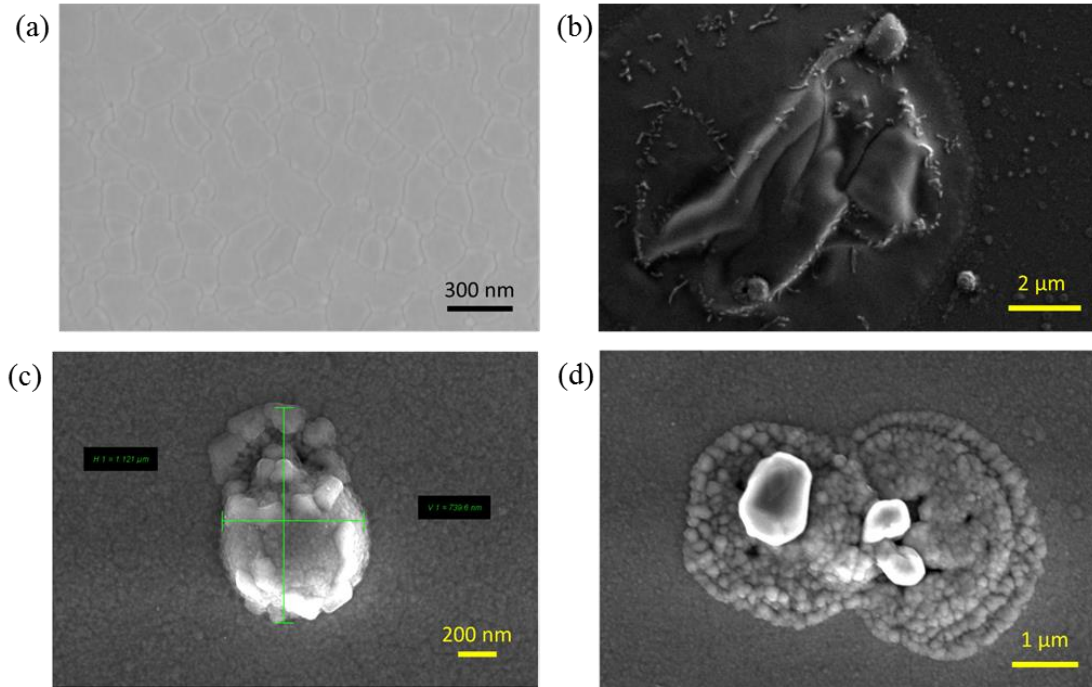
Figure 5-10. Scanning tunneling microscope images of piezoelectric substrates and islands. (a) PZT surface. (b) Large islands on PZT. (c) and (d) are small islands on annealed evaporated gate electrodes.

5.2.3 How a strain gauge works

To know the relation between strain applied on the 2D material flake and the electric field applied across PZT, we decide to fabricate strain gauges (which are also called strain gages) near the flake. Firstly we have to know how a strain gauge works.

Each strain gauge is associated with a quantity called gauge factor (GF), which relates its relative resistance change to the strain it experiences:

$$\text{Gauge factor (GF)} = \frac{\Delta R/R}{\varepsilon} = \frac{\Delta R/R}{\Delta L/L} \tag{5-7}$$

where R is resistance of the strain gauge before strain applied and ε is strain. Usually a strain gauge for direction x_i has a much longer dimension along x_i and the extensional

110

strain along x_i is $\Delta L/L$ (Figure 5-11). The gauge factor depends on material type and temperature, and ideally it is independent of the geometry of the gauge. Some research shows that gauge factor depends on thickness [246, 247]. But gauge factor does not depend on the material's length and width, which is supported in our data shown in Figure 5-15.
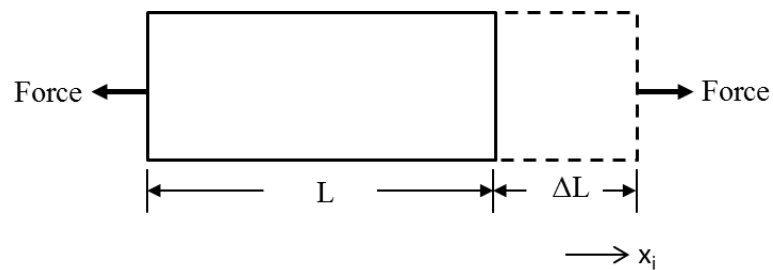
Figure 5-11. Schematic of extensional strain along x_i direction, which is $\Delta L/L$.

To make a strain gauge long in one dimension, "meandering" design is often used. Figure 5-12 shows one design of our strain gauges. When a strain is applied, a strain gauge measuring longitudinal strain (x axis) deforms in all directions, say it stretches along x axis and shrinks in y and z axes. Thus the change in resistance does not only come from the axis of interest, longitudinal direction, but also from the other transverse axes. To reduce the sensitivity of resistance change from transverse directions, strain gauges are often designed with "end loops", which are wider in width and thus have smaller resistance (Figure 5-12(d)).
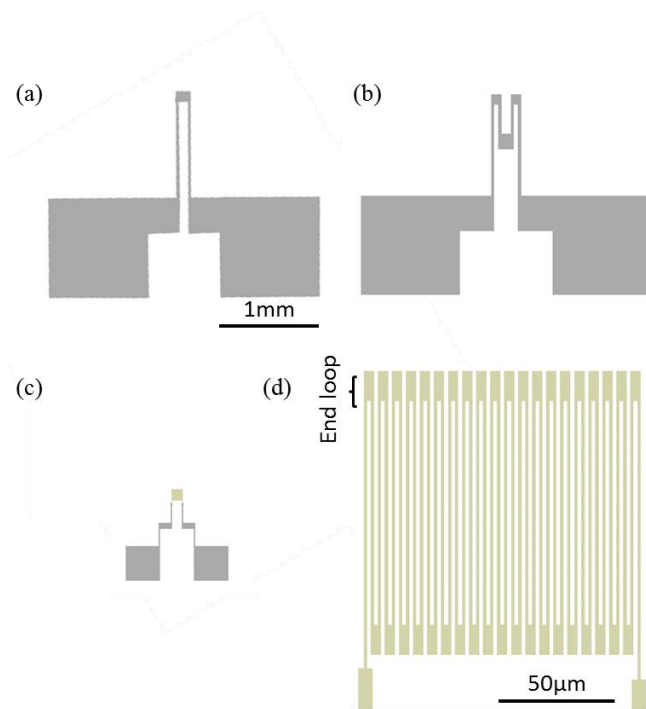
Figure 5-12. Three nichrome strain gauge designs for wafer flexure characterization. (a)-(c) are in same scales. All gauges are designed with end loops. (a) Gauge 20-100: The pattern consists of 2 aligned traces that are 20μm wide and spaced 100μm apart. (b) Gauge 25-50: The pattern is made with 4 aligned traces that are 25μm wide. (c) Gauge 1-1.5: A gauge with a meandering pattern, which is colored in dark yellow. (d) Zoom-in view of the meandering part in gauge (c). The uni-axial pattern consists of 40 aligned traces that are 1μm wide, spaced 1.5μm apart. The end loops are indicated.

5.2.4 Characterization of strain gauges: wafer flexure technique

We choose to deposit nichrome (Ni 80% Cr 20%) for our strain gauges because its gauge factor only changes within 7% from room temperature to cryogenic temperature [248, 249].

Before we characterize the piezoelectric wafer with nichrome gauges, we need to characterize the nichrome gauges and obtain their gauge factor. To do so, we fabricate nichrome gauges in several different geometries on a 4" SiO_2/Si wafer and obtain

the gauge factor of our gauges at room temperature using wafer flexure method [250].
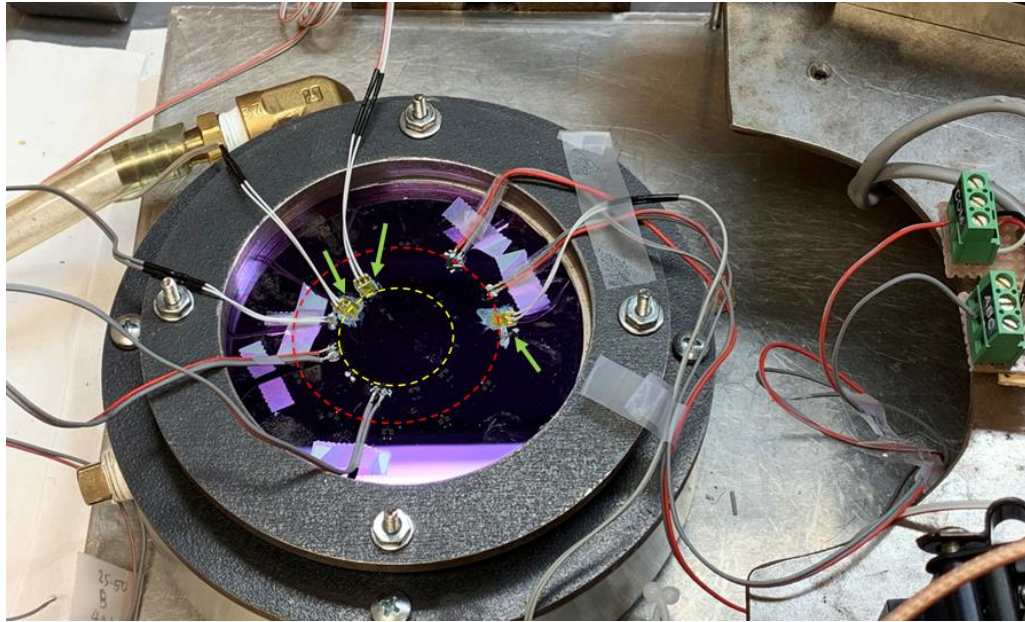
Figure 5-13. Wafer flexure setup.
All the strain gauges, home-made nichrome gauges and commercial ones, are either on the inner (yellow dashed line) or outer circle (red dashed line). Both circles and the 4" substrate wafer are concentric. The green arrows indicate the commercial gauges, which are larger-sized and encapsulated in polyimide. (The setup in this picture is built by Dr. Susan Trolier-McKinstry's group.)

Wafer preparation

30nm-thick nichrome strain gauges are deposited on a 4" SiO_2/Si wafer from NOVA Electronic Materials. Strain gauges are written with e-beam. Nichrome is deposited at 1Å/s rate with e-beam evaporation at Kurt J. Lesker Lab-18. The gauges are located on two concentric circles, inner and outer circles, with the same center of the substrate wafer (yellow and red dashed lines in Figure 5-13).

Solder the nichrome gauges with AWG 28 leads, which are the same leads as of strain gauges from Omega. Tape down the leads with scotch tapes to hold the leads in position. To make the soldered joint strong enough, put a blob of glue on top of each soldered joint. Afterward glue 1~2 commercial gauges (Omega KFH-1.5-120-C1-11L1M2R) on each circle.

Wafer flexure technique setup

We use the wafer flexure equipment in Dr. Susan Trolier-McKinstry's lab. The wafer is clamped onto an air-tight housing and flexed by oscillating air produced by a high power audio speaker (Figure 5-13). The frequency of the air oscillation is 4Hz, which is slow enough for the wafer to follow. Detailed setup is described in the paper of Shepard et al. [250].

Characterize nichrome strain gauges with commercial gauges

With commercial gauges, we can obtain the strain at the commercial gauges' positions. As the wafer flexure setup is radial symmetric, we can assume that the strain at positions in same distance to substrate wafer center are the same. In other words, the strain values are the same at each concentric circle with the 4" substrate wafer.
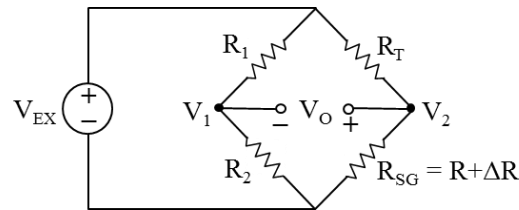
Figure 5-14. Schematic of Wheatstone bridge circuit used in wafer flexure setup.

R_T and R_{SG} are a tunable resistor and a strain gauge, respectively. V_{EX} and V_O are an external voltage source and output voltage, respectively. V_1 is the potential at the R_1-R_2 joint and V_2 is the potential at the R_T-R_{SG} joint. When $R_T / R_{SG} = R_1 / R_2$, V_O is zero and we say the circuit is balanced. (Figure is adapted from Application Note 078 by National Instruments [251].)

We can measure the strain experienced by a strain gauge by measuring the gauge's resistance change. We use a conventional Wheatstone bridge, which is the most frequently used circuit due to its outstanding sensitivity. Figure 5-14 depicts the Wheatstone bridge circuit used in our experiment.

$$V_O = V_2 - V_1 = \left[\frac{R_{SG}}{R_T + R_{SG}} - \frac{R_2}{R_1 + R_2} \right] \cdot V_{EX} \tag{5-8}$$

In our setup, the external voltage V_{EX} is an AC bias applied by a lock-in amplifier and $R_1 = R_2 = 2k\Omega$. R_T is a tunable resistor with maximum resistance $10k\Omega$. Suppose the resistance of the strain gauge R_{SG} is R. At the beginning of the measurement, R_T is tuned to match R_{SG} so the output voltage is zero and the circuit is balanced to start. When a strain is applied to the gauge, its resistance becomes $R+\Delta R$. The output voltage becomes $V_O = \frac{\Delta R}{4R + 2\Delta R} \cdot V_{EX}$. Define relative voltage change $V_r \equiv V_O/V_{EX}$ and write the relative resistance in terms of V_r: $\frac{\Delta R}{R} = \frac{4V_r}{1 - 2V_r}$. And thus strain can be written in the following form:

$$\varepsilon = \frac{\Delta R/R}{GF} = \frac{4V_r}{GF(1 - 2V_r)} \tag{5-9}$$

As the gauge factor of a commercial gauge is known, strain value can be obtained by measuring the output voltage of the Wheatstone bridge.
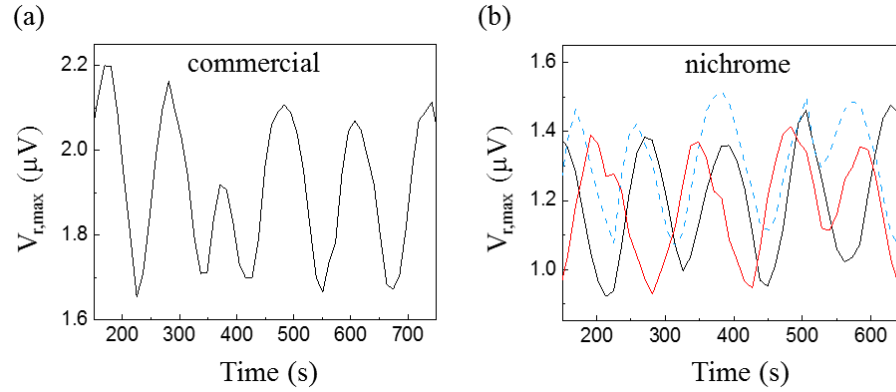
Figure 5-15. Plot of relative voltage change amplitude $V_{r,max}$ versus time. The substrate wafer oscillates at 4Hz and the $V_{r,max}$ is measured using the lock-in amplifier with a time constant 10s. (a) $V_{r,max}$-t plot from a commercial gauge CG1 located at the inner circle. The average $V_{r,max}$ is 1.9μV and the gauge factor of the commercial gauge is 1.84, from which we can deduct the strain amplitude 4.1με. (b) $V_{r,max}$-t plot from nichrome gauges at the inner circle: 25-50A (black solid line), 25-50B (red solid line, and 20-100A (blue dashed line). The average $V_{r,max}$ of the three gauges are 1.2μV, 1.2μV, and 1.3μV, respectively.

Throughout our flexure experiment, we use the same driving amplitude and frequency to drive the speaker. The speaker, and so does the substrate wafer, oscillates at 4Hz. Therefore ΔR and V_r also oscillate at 4Hz. Measuring V_r using a lock-in amplifier with frequency locked to the wafer driving signal, one can acquire the amplitude of V_r: $V_{r,max}$. $V_{r,max}$ corresponds to the relative voltage change when the wafer is applied the maximum strain, namely when the wafer is farthest away from its equilibrium plane. Figure 5-15(a) plots $V_{r,max}$ versus time from a commercial gauge CG1 located at the inner circle. We can plug average $V_{r,max}$ and gauge factor of the commercial gauge into equation (5-9) to obtain the strain amplitude at inner circle, which is 4.1×10^{-6}. As the strain produced by piezoelectric materials is about the order of μm/m, it is convenient to express strain in microstrain unit, με, where the strain value is multiplied by 10^6. In other words, the strain

amplitude at inner circle can be written as 4.1µε. We then measure $V_{r,max}$ versus time of a nichrome gauge 25-50A, which locates right next to CG1 at the inner circle (Figure 5-15(b) black curve). It is reasonable to assume that the strain the two gauges experience is similar. With the average $V_{r,max}$ of 25-50A and strain amplitude 4.1µε, we can get a gauge factor of 1.2 for 25-50A using equation (5-9).

We measured two more nichrome gauges at the inner circle, 25-50B and 20-100A (Figure 5-15(b)). 25-50B is adjacent to 25-50A and they have very similar $V_{r,max}$-t traces with the same $V_{r,max}$ average 1.2µV, which give the same gauge factor 1.2. 20-100A is 90 degree away from 25-50A and has a different geometry (see Figure 5-12 for our nichrome gauge patterns). Nonetheless it has an average $V_{r,max}$ equal to 1.3 µV, which is close to the other two 25-50 gauges and gives a gauge factor 1.3. Figure 5-15 supports the validity of two assumptions. One is that the strain at every position of the inner circle is similar. The other is that gauge factor is independent of lateral geometry: width, length and shape.

We also measured gauges at the outer circle but cannot get valid data. We suspect that the strain amplitude at the outer circle is too small to be measured by our setup.

5.2.5 Characterization of our piezoelectric substrate with home-made strain gauges

To measure how much strain can be applied to a 2D flake by our piezoelectric substrate, we fabricate a pair of perpendicular nichrome strain gauges close to the center of the pre-patterned gate electrode (shown in Figure 5-16).
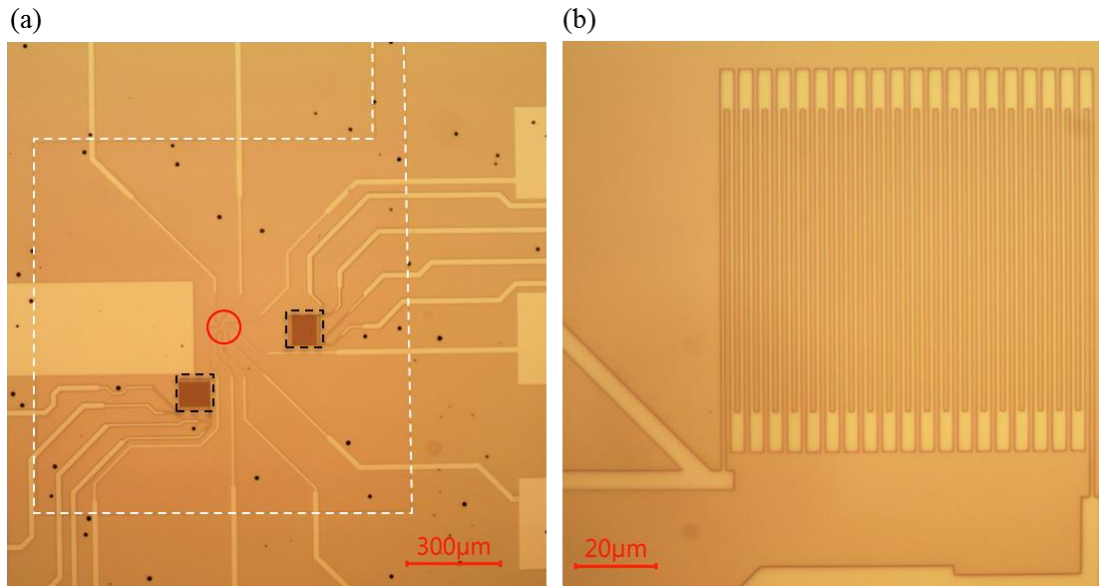
Figure 5-16. Nichrome strain gauges over the pre-patterned gate electrode.
(a) A pair of perpendicular strain gauges (outlined in black) are fabricated as close to the designed flake position (circled in red) as possible. The pre-patterned gate electrode is indicated by the white dashed line. The resistance of each strain gauge is about 150 kΩ.
(b) Magnified image of a strain gauge in (a).

The substrate is then poled on a hot plate following the process:

1. Heat up the substrate on a hot plate to 150 ˚C when electric field across PZT is zero.

2. Ramp up the electric field across PZT and park the field at around 8.4~11.2 kV/cm (corresponding voltage is 15~20 V for our PZT film) for 15 minutes. To avoid leakage of Al_2O_3, pre-patterned gate electrode is grounded and a negative voltage is applied to the bottom electrode.

3. Turn off the hot plate. Wait for the substrate to cool down to room temperature before ramp the electric field back to zero.

In the last part of this section, we are going to characterize our PZT film by answering the question: how much strain the PZT film can provide when a voltage V_{PZT} is applied across it. Note that after poling, we always apply an electric field in the same direction of the PZT polarization to avoid switching the polarization. To avoid leakage of Al_2O_3, pre-patterned gate electrode is grounded and a negative voltage V_{PZT} is applied to the bottom electrode by Keithley 2400. Because the piezoelectric coefficient d_{31} of PZT is negative, we expect the film to shrink in xy plane when an electric field is applied, which would reduce the resistance of the strain gauges.

We use a Wheatstone bridge setup for the strain measurement. Though we can measure the resistance of the strain gauges with a SR830 Lock-In Amplifier, the amplifier only has 4.5 digits of resolution, which is not enough to measure the resistance change due to strain of the order 1~10 $\mu\varepsilon$. We measure the change of output voltage V_O (illustrated in Figure 5-17) when varying the electric field applied across the PZT film.
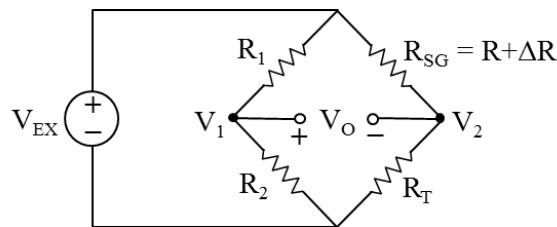
Figure 5-17. Schematic of Wheatstone bridge circuit used in this section.
R_T and R_{SG} are a tunable resistor and a nichrome strain gauge, respectively. V_{EX} and V_O are an external voltage source and output voltage, respectively. V_{EX} is applied by a SR830 Lock-In Amplifier with 0.5 V at 12.27 Hz. R_{SG} is ~150 kΩ, and R_1 and R_2 are ~100 kΩ. R_T is tuned to make the phase difference of V_O ~20 degree. (Figure is adapted from Application Note 078 by National Instruments [251].)

In our current setup, there is a background variation in V_O with a period of about one hour and an amplitude of ~15 µV when V_{EX} is 0.5 V. We suspect the variation is caused by the change of the ambient temperature. To bypass issues caused by the background variation, we sweep V_{PZT} at a higher rate such as 400 mV/s for the characterization. Figure 5-18 shows how we obtain the strain versus V_{PZT} relation. Figure 5-18(a) shows a V_O - V_{PZT} loop when V_{PZT} is swept from 0 V → $V_{PZT,MAX}$ → 0 V where $V_{PZT,MAX}$ = 10 V. The loop starts from a minimum V_O near V_{PZT} = 0, reaches maximum V_O around V_{PZT} = $V_{PZT,MAX}$, and then comes back to a lower V_O. The minimum and maximum V_O pair of the loop can be translated into the resistance change in R_{SG}, by which we can obtain the strain. Such strain is then recorded as one data point at V_{PZT} = 10 V in the strain versus V_{PZT} plot (Figure 5-18(b)). Data in (Figure 5-18(b)) are acquired from higher to lower V_{PZT}.
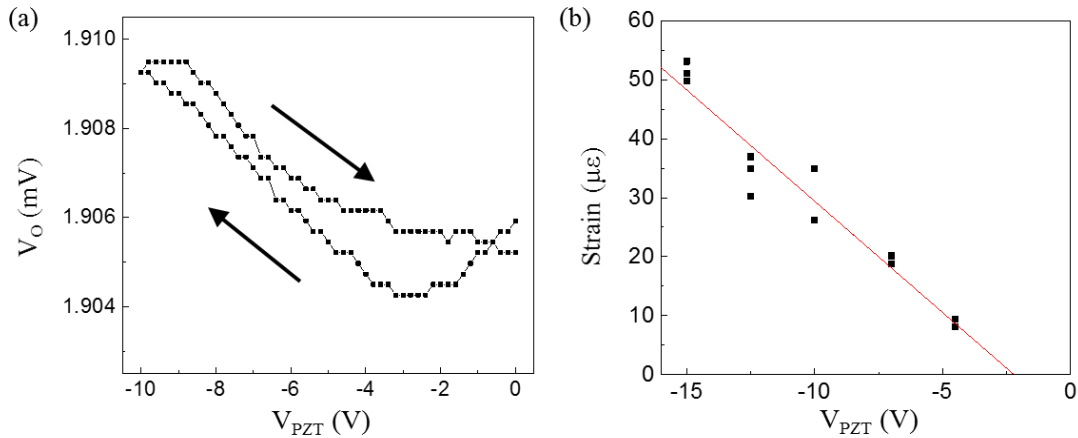
Figure 5-18. V_O - V_{PZT} loop and strain versus V_{PZT} relation.
(a) V_O - V_{PZT} loop when V_{PZT} is swept from 0 V → -10 V → 0 V. V_{PZT} is the voltage applied to bottom electrode while the pre-patterned gate electrode is grounded. (b) Strain versus V_{PZT} relation. The red line is a linear fit to the data points: strain(µɛ) = -3.777 V_{PZT}(V) + 0.323(µɛ).

The magnitude of the strain in Figure 5-18 is much smaller compared to that of a typical good PZT film and the sign of the strain is opposite. The strain in x-y plane is given by d_{31} times the electric field in z direction. A typical good PZT film has $d_{31} = -165 \sim -310$ pm/V [237, 238] so we were expecting a "negative" strain around $-0.12 \sim -0.23\%$ at the maximum field we applied (15V/2μm or 75 kV/cm).

As the data in Figure 5-18 were obtained from only one device, we cannot make a concluded statement. Further investigation is needed to figure out whether the small positive strain is a global behavior of our PZT film and what causes such a different film behavior.

5.2.6 Conclusion

We designed and fabricated a PZT-based piezoelectric substrate incorporating strain tuning, Al_2O_3 gating, ionic liquid gating, and electrical measurement capabilities. Since strain can be an effective knob tuning superconductivity, magnetism, ferroelectricity and ferroelasticity, the ability to control strain offers another playground in low-temperature measurements. We aim for a platform compatible with cryogenic measurements and available for convenient and reliable strain tuning. Further characterization of our piezoelectric substrate is needed to better understand its performance, which is essential for its application and improvement.

Appendix

Sub-micron electrode fabrication using optical lithography

We decide to fabricate our piezoelectric substrate with optical lithography due to its benefit of time and budget saving. The tool we use is GCA 8500 5X stepper with 365 nm monochromatic light. One challenge we faced was that optical lithography becomes less reliable when features are around 1 μm or smaller, which is the dimension of the electrodes we plan to have. When working with larger features like 2~4 µm or above, LOR/3012 double-layer photoresist works well. But because LOR is not light sensitive and dissolves fast in CD26 developer, the yield of our sub-micron electrodes is low if we use LOR/3012 resist. To address the issue, we substitute PMGI for LOR because PMGI is light sensitive and dissolves more slowly in developer.

Figure A-1 shows how PMGI/3012 double-layer photoresist works. After the sample spin coated with resist is exposed optically at a stepper, it is developed with CD26. This step is to dissolve exposed 3012 completely. Then the sample is treated with deep UV and the 3012 layer acts as a deep UV mask. Finally the sample is developed with developer 101A to dissolve UV treated PMGI. Note that 3012 does not dissolve in 101A. It is also important to keep in mind not to develop the sample with CD26 in step (c) because the whole 3012 layer is exposed by deep UV and it will dissolve in CD26 completely.
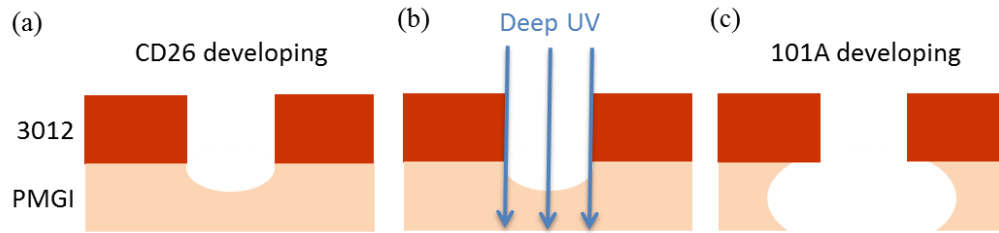
Figure A-1. How PMGI/3012 double-layer photoresist works.
(a) After expose the resist optically, develop with developerCD26 to dissolve exposed 3012. To dissolve exposed 3012 completely, some PMGI might see CD26 and dissolve. (b) Treat with deep UV to expose PMGI not covered by 3012, which acts as a deep UV mask. (c) Develop UV treated PMGI with developer 101A.

The following is the recipes we tried for PMGI/3012 dose tests. In each dose test, we try an array of different exposure time and focal planes (exposure time range 0.18s ~ 0.34s and focus change range −0.6 ~+0.6μm). The goal is to obtain a robust recipe for sub-micron electrode fabrication. It has to have some tolerance in the focal plane and exposure time.

Test recipe 1: Use PMGI SF2S, which is also called SF2Slow. The resist develops more slowly compared to PMGI SF2. Spin coated PMGI is baked at 210°C (measured by a thermal coupler thermometer).

Result: The developing rate of 210°C-baked PMGI SF2S is too slow. Most part of the array is underdeveloped. Only one condition with long exposure time (0.34s) gives the result we want, which is because much PMGI resist is developed in CD26 (step (a) in Fig. A-1) after such a long exposure time.

Test recipe 2: Still use PMGI SF2S but lower the PMGI baking temperature to 190°C. Increase the deep UV treatment time from 180s to 210s.

Result: By lowering the resist baking temperature, resist dissolves faster in the developer. But the developing rate of 190°C-baked PMGI SF2S is still too slow.

Test recipe 3: Instead of PMGI SF2S, use PMGI SF2 and bake it at 195°C. Result: This recipe works well. There is a window of exposure time and focus that can work: exposure time 0.26~0.30s and focus change $-0.6 \sim -0.2\mu m$.

Bibliography

1. K. S. Novoselov, A. K. Geim, S. V. Morozov, D. Jiang, Y. Zhang, S. V. Dubonos, I. V. Grigorieva and A. A. Firsov: Electric Field Effect in Atomically Thin Carbon Films. *Science* 306, 666 (2004)
2. L. Wang, I. Meric, P. Y. Huang, Q. Gao, Y. Gao, H. Tran, T. Taniguchi, K. Watanabe, L. M. Campos, D. A. Muller, J. Guo, P. Kim, J. Hone, K. L. Shepard and C. R. Dean: One-dimensional electrical contact to a two-dimensional material. *Science* 342, 614 (2013)
3. C. Lee, X. Wei, J. W. Kysar and J. Hone: Measurement of the Elastic Properties and Intrinsic Strength of Monolayer Graphene. *Science* 321, 385 (2008)
4. B. C. Janegitz, T. A. Silva, A. Wong, L. Ribovski, F. C. Vicentini, M. del Pilar Taboada Sotomayor and O. Fatibello-Filho: The application of graphene for in vitro and in vivo electrochemical biosensing. *Biosensors and Bioelectronic* 89, 224 (2017)
5. A. Rycerz, J. Tworzydło and C. W. J. Beenakker: Valley filter and valley valve in graphene. *Nature Physics* 3, 172 (2007)
6. X. Xu, W. Yao, D. Xiao and T. F. Heinz: Spin and pseudospins in layered transition metal dichalcogenides. *Nature Physics* 10, 343 (2014)
7. J. Li, K. Wang, K. J. McFaul, Z. Zern, Y. Ren, K. Watanabe, T. Taniguchi, Z. Qiao and J. Zhu: Gate-controlled topological conducting channels in bilayer graphene. *Nature Nanotechnology* 11, 1060 (2016)
8. K. F. Mak, C. Lee, J. Hone, J. Shan and T. F. Heinz: Atomically Thin MoS2: A New Direct-Gap Semiconductor. *Physical Review Letters* 105, 136805 (2010)
9. Z. Y. Zhu, Y. C. Cheng and U. Schwingenschlögl: Giant spin-orbit-induced spin splitting in two-dimensional transition-metal dichalcogenide semiconductors. *Physical Review B* 84, 153402 (2011)
10. D. Xiao, G.-B. Liu, W. Feng, X. Xu and W. Yao: Coupled Spin and Valley Physics in Monolayers of MoS2and Other Group-VI Dichalcogenides. *Physical Review Letters* 108, 196802 (2012)
11. F. H. L. Koppens, T. Mueller, P. Avouris, A. C. Ferrari, M. S. Vitiello and M. Polini: Photodetectors based on graphene, other two-dimensional materials and hybrid systems. *Nature Nanotechnology* 9, 780 (2014)
12. J. Feng, X. Qian, C.-W. Huang and J. Li: Strain-engineered artificial atom as a broad-spectrum solar energy funnel. *Nature Photonics* 6, 866 (2012)
13. S. Manzeli, D. Ovchinnikov, D. Pasquier, O. V. Yazyev and A. Kis: 2D transition metal dichalcogenides. *Nature Reviews Materials* 2, 17033 (2017)
14. K. R. Allakhverdiev, M. Ö. Yetis, S. Özbek, T. K. Baykara and E. Y. Salaev: Effective nonlinear GaSe crystal. Optical properties and applications. *Laser Physics* 19, 1092 (2009)
15. D. J. Late, B. Liu, J. Luo, A. Yan, H. S. S. R. Matte, M. Grayson, C. N. R. Rao and V. P. Dravid: GaS and GaSe Ultrathin Layer Transistors. *Advanced Materials* 24, 3549 (2012)

16. Y. Ma, Y. Dai, M. Guo, L. Yu and B. Huang: Tunable electronic and dielectric behavior of GaS and GaSe monolayers. *Physical Chemistry Chemical Physics* 15, 7098 (2013)

17. X. Li, M.-W. Lin, A. A. Puretzky, J. C. Idrobo, C. Ma, M. Chi, M. Yoon, C. M. Rouleau, I. I. Kravchenko, D. B. Geohegan and K. Xiao: Controlled Vapor Phase Growth of Single Crystalline, Two-Dimensional GaSe Crystals with High Photoresponse. *Scientific Reports* 4, 1 (2014)

18. T. Cao, Z. Li and S. G. Louie: Tunable Magnetism and Half-Metallicity in Hole-Doped Monolayer GaSe. *Physical Review Letters* 114, 236602 (2015)

19. N. C. Fernelius: Properties of Gallium Selenide Single Crystal. *Progress in Crystal Growth and Characterization of materials*, 1 (1994)

20. Y. Zhou, Y. Nie, Y. Liu, K. Yan, J. Hong, C. Jin, Y. Zhou, J. Yin, Z. Liu and H. Peng: Epitaxy and Photoresponse of Two-Dimensional GaSe Crystals on Flexible Transparent Mica Sheets. *ACS Nano* 8, 1485 (2014)

21. Z. Ben Aziza, D. Pierucci, H. Henck, M. G. Silly, C. David, M. Yoon, F. Sirotti, K. Xiao, M. Eddrief, J.-C. Girard and A. Ouerghi: Tunable quasiparticle band gap in few-layer GaSe/graphene van der Waals heterostructures. *Physical Review B* 96, 035407 (2017)

22. Y. Huang, E. Sutter, N. N. Shi, J. Zheng, T. Yang, D. Englund, H.-J. Gao and P. Sutter: Reliable Exfoliation of Large-Area High-Quality Flakes of Graphene and Other Two-Dimensional Materials. *ACS Nano* 9, 10612 (2015)

23. S. B. Desai, S. R. Madhvapathy, M. Amani, D. Kiriya, M. Hettick, M. Tosun, Y. Zhou, M. Dubey, J. W. Ager Iii, D. Chrzan and A. Javey: Gold-Mediated Exfoliation of Ultralarge Optoelectronically-Perfect Monolayers. *Advanced Materials* 28, 4053 (2016)

24. G. R. Bhimanapati, Z. Lin, V. Meunier, Y. Jung, J. Cha, S. Das, D. Xiao, Y. Son, M. S. Strano, V. R. Cooper, L. Liang, S. G. Louie, E. Ringe, W. Zhou, S. S. Kim, R. R. Naik, B. G. Sumpter, H. Terrones, F. Xia, Y. Wang, J. Zhu, D. Akinwande, N. Alem, J. A. Schuller, R. E. Schaak, M. Terrones and J. A. Robinson: Recent Advances in Two-Dimensional Materials beyond Graphene. *ACS Nano* 9, 11509 (2015)

25. K. V. Emtsev, A. Bostwick, K. Horn, J. Jobst, G. L. Kellogg, L. Ley, J. L. McChesney, T. Ohta, S. A. Reshanov, J. Röhrl, E. Rotenberg, A. K. Schmid, D. Waldmann, H. B. Weber and T. Seyller: Towards wafer-size graphene layers by atmospheric pressure graphitization of silicon carbide. *Nature Materials* 8, 203 (2009)

26. G. Li, Y.-Y. Zhang, H. Guo, L. Huang, H. Lu, X. Lin, Y.-L. Wang, S. Du and H.-J. Gao: Epitaxial growth and physical properties of 2D materials beyond graphene: from monatomic materials to binary compounds. *Chem. Soc. Rev.* 47, 6073 (2018)

27. K. S. Kim, Y. Zhao, H. Jang, S. Y. Lee, J. M. Kim, K. S. Kim, J.-H. Ahn, P. Kim, J.-Y. Choi and B. H. Hong: Large-scale pattern growth of graphene films for stretchable transparent electrodes. *Nature* 457, 706 (2009)

28. Y. Zhang, L. Zhang and C. Zhou: Review of Chemical Vapor Deposition of Graphene and Related Applications. *Accounts of Chemical Research* 46, 2329 (2013)

29. B. Liu, M. Fathi, L. Chen, A. Abbas, Y. Ma and C. Zhou: Chemical Vapor Deposition Growth of Monolayer WSe 2with Tunable Device Characteristics and Growth Mechanism Study. *ACS Nano* 9, 6119 (2015)

30. Y. Sheng, X. Wang, K. Fujisawa, S. Ying, A. L. Elias, Z. Lin, W. Xu, Y. Zhou, A. M. Korsunsky, H. Bhaskaran, M. Terrones and J. H. Warner: Photoluminescence Segmentation within Individual Hexagonal Monolayer Tungsten Disulfide Domains Grown by Chemical Vapor Deposition. *ACS Applied Materials & Interfaces* 9, 15005 (2017)

31. Z. Lin, A. McCreary, N. Briggs, S. Subramanian, K. Zhang, Y. Sun, X. Li, N. J. Borys, H. Yuan, S. K. Fullerton-Shirey, A. Chernikov, H. Zhao, S. McDonnell, A. M. Lindenberg, K. Xiao, B. J. LeRoy, M. Drndić, J. C. M. Hwang, J. Park, M. Chhowalla, R. E. Schaak, A. Javey, M. C. Hersam, J. Robinson and M. Terrones: 2D materials advances: from large scale synthesis and controlled heterostructures to improved characterization techniques, defects and applications. *2D Materials* 3, 042001 (2016)

32. K. Kang, S. Xie, L. Huang, Y. Han, P. Y. Huang, K. F. Mak, C.-J. Kim, D. Muller and J. Park: High-mobility three-atom-thick semiconducting films with wafer-scale homogeneity. *Nature* 520, 656 (2015)

33. M. J. Ludowise: Metalorganic chemical vapor deposition of III-V semiconductors. *Journal of Applied Physics* 58, R31 (1985)

34. L. Do Hee, Y. Sim, J. Wang and S.-Y. Kwon: Metal–organic chemical vapor deposition of 2D van der Waals materials—The challenges and the extensive future opportunities. *APL Materials* 8, 030901 (2020)

35. J. Engelmann, V. Grinenko, P. Chekhonin, W. Skrotzki, D. V. Efremov, S. Oswald, K. Iida, R. H. u. hne, J. H. a. nisch, M. Hoffmann, F. Kurth, L. Schultz and B. Holzapfel: Strain induced superconductivity in the parent compound BaFe2As2. *Nature Communications* 4, 2877 (2013)

36. W. Hou, A. Azizimanesh, A. Sewaket, T. Peña, C. Watson, M. Liu, H. Askari and S. M. Wu: Strain-based room-temperature non-volatile MoTe$_2$ ferroelectric phase change transistor. *Nature Nanotechnology*, 668 (2019)

37. D. V. Christensen, Y. Frenkel, Y. Z. Chen, Y. W. Xie, Z. Y. Chen, Y. Hikita, A. Smith, L. Klein, H. Y. Hwang, N. Pryds and B. Kalisky: Strain-tunable magnetism at oxide domain walls. *Nature Physics* 15, 269 (2019)

38. Y. Zhang, C.-H. Hu, Y.-H. Wen, S.-Q. Wu and Z.-Z. Zhu: Strain-tunable band gap of hydrogenated bilayer graphene. *New Journal of Physics* 13, 063047 (2011)

39. M. Ghorbani-Asl, S. Borini, A. Kuc and T. Heine: Strain-dependent modulation of conductivity in single-layer transition-metal dichalcogenides. *Physical Review B* 87, 235434 (2013)

40. J. Zhou, Y. Wu, H. Wang, Z. Wu, X. Li, W. Yang, C. Ke, S. Lu, C. Zhang and J. Kang: Strain manipulation of the polarized optical response in two-dimensional GaSe layers. *Nanoscale* 12, 4069 (2020)

41. Y. Ma, Y. Dai, M. Guo, C. Niu, Y. Zhu and B. Huang: Evidence of the Existence of Magnetism in Pristine VX$_2$ Monolayers (X = S, Se) and Their Strain-Induced Tunable Magnetic Properties. *ACS Nano* 6, 1695 (2012)

42. B. L. Chittari, Y. Park, D. Lee, M. Han, A. H. MacDonald, E. Hwang and J. Jung: Electronic and magnetic properties of single-layer MPX_3 metal phosphorous trichalcogenides. *Physical Review B* 94, 184428 (2016)

43. B. L. Chittari, D. Lee, A. H. MacDonald, E. Hwang and J. Jung: Carrier- and strain-tunable intrinsic magnetism in two-dimensional MAX(3) transition metal chalcogenides. *Physical Review B* 101, 085415 (2020)

44. M. Huang, T. A. Pascal, H. Kim, W. A. Goddard and J. R. Greer: Electronic-Mechanical Coupling in Graphene from in situ Nanoindentation Experiments and Multiscale Atomistic Simulations. *Nano Letters* 11, 1241 (2011)

45. K. Xu, K. Wang, W. Zhao, W. Bao, E. Liu, Y. Ren, M. Wang, Y. Fu, J. Zeng, Z. Li, W. Zhou, F. Song, X. Wang, Y. Shi, X. Wan, M. S. Fuhrer, B. Wang, Z. Qiao, F. Miao and D. Xing: The positive piezoconductive effect in graphene. *Nature Communications* 6, 8119 (2015)

46. F. Guan: Effect of Strain on the Mechanical and Transport Properties of Graphene. *Thesis*, 1 (2016)

47. F. Ding, H. Ji, Y. Chen, A. Herklotz, K. Dörr, Y. Mei, A. Rastelli and O. G. Schmidt: Stretchable Graphene: A Close Look at Fundamental Parameters through Biaxial Straining. *Nano Letters* 10, 3453 (2010)

48. C. R. Dean, A. F. Young, I. Meric, C. Lee, L. Wang, S. Sorgenfrei, K. Watanabe, T. Taniguchi, P. Kim, K. L. Shepard and J. Hone: Boron nitride substrates for high-quality graphene electronics. *Nature Nanotechnology* 5, 722 (2010)

49. A. S. Mayorov, R. V. Gorbachev, S. V. Morozov, L. Britnell, R. Jalil, L. A. Ponomarenko, P. Blake, K. S. Novoselov, K. Watanabe, T. Taniguchi and A. K. Geim: Micrometer-Scale Ballistic Transport in Encapsulated Graphene at Room Temperature. *Nano Letters* 11, 2396 (2011)

50. X. Xi, L. Zhao, Z. Wang, H. Berger, L. Forró, J. Shan and K. F. Mak: Strongly enhanced charge-density-wave order in monolayer NbSe2. *Nature Nanotechnology* 10, 765 (2015)

51. J. I. J. Wang, Y. Yang, Y.-A. Chen, K. Watanabe, T. Taniguchi, H. O. H. Churchill and P. Jarillo-Herrero: Electronic Transport of Encapsulated Graphene and WSe 2Devices Fabricated by Pick-up of Prepatterned hBN. *Nano Letters* 15, 1898 (2015)

52. S. Xu, Z. Wu, H. Lu, Y. Han, G. Long, X. Chen, T. Han, W. Ye, Y. Wu, J. Lin, J. Shen, Y. Cai, Y. He, F. Zhang, R. Lortz, C. Cheng and N. Wang: Universal low-temperature Ohmic contacts for quantum transport in transition metal dichalcogenides. In: *2D Materials*. IOP Publishing, (2015)

53. Z. Wang, D. n. K. Ki, H. Chen, H. Berger, A. H. MacDonald and A. F. Morpurgo: Strong interface-induced spin-orbit interaction in graphene on WS2. *Nature Communications* 6, 8339 (2015)

54. Z. Wang, D.-K. Ki, J. Y. Khoo, D. Mauro, H. Berger, L. S. Levitov and A. F. Morpurgo: Origin and Magnitude of `Designer' Spin-Orbit Interaction in Graphene on Semiconducting Transition Metal Dichalcogenides. *Physical Review X* 6, 041020 (2016)

55. M. Gmitra and J. Fabian: Proximity Effects in Bilayer Graphene on Monolayer WSe_2: Field-Effect Spin Valley Locking, Spin-Orbit Valve, and Spin Transistor. *Physical Review Letters* 119, 146401 (2017)

56. J. O. Island, X. Cui, C. Lewandowski, J. Y. Khoo, E. M. Spanton, H. Zhou, D. Rhodes, J. C. Hone, T. Taniguchi, K. Watanabe, L. S. Levitov, M. P. Zaletel and A. F. Young: SSpin–orbit-driven band inversion in bilayer graphene by the van der Waals proximity effect. *Nature* 571, 85 (2019)

57. J. Li, H.-B. Leng, H. Fu, K. Watanabe, T. Taniguchi, X. Liu, C.-X. Liu and J. Zhu: Superconducting proximity effect in a transparent van der Waals superconductor-metal junction. *Physical Review B* 101, 195405 (2020)

58. E. H. Hwang and S. Das Sarma: Acoustic phonon scattering limited carrier mobility in two-dimensional extrinsic graphene. *Physical Review B* 77, 115449 (2008)

59. J.-H. Chen, C. Jang, S. Xiao, M. Ishigami and M. S. Fuhrer: Intrinsic and extrinsic performance limits of graphene devices on SiO_2. *Nature Nanotechnology* 3, 206 (2008)

60. Y. Cao, V. Fatemi, S. Fang, K. Watanabe, T. Taniguchi, E. Kaxiras and P. Jarillo-Herrero: Unconventional superconductivity in magic-angle graphene superlattices. *Nature* 556, 43 (2018)

61. Y. Cao, V. Fatemi, A. Demir, S. Fang, S. L. Tomarken, J. Y. Luo, J. D. Sanchez-Yamagishi, K. Watanabe, T. Taniguchi, E. Kaxiras, R. C. Ashoori and P. Jarillo-Herrero: Correlated insulator behaviour at half-filling in magic-angle graphene superlattices. *Nature* 556, 80 (2018)

62. M. Yankowitz, S. Chen, H. Polshyn, Y. Zhang, K. Watanabe, T. Taniguchi, D. Graf, A. F. Young and C. R. Dean: Tuning superconductivity in twisted bilayer graphene. *Science* 363, 1059 (2019)

63. A. L. Sharpe, E. J. Fox, A. W. Barnard, J. Finney, K. Watanabe, T. Taniguchi, M. A. Kastner and D. Goldhaber-Gordon: Emergent ferromagnetism near three-quarters filling in twisted bilayer graphene. *Science* 365, 605 (2019)

64. X. Lu, P. Stepanov, W. Yang, M. Xie, M. A. Aamir, I. Das, C. Urgell, K. Watanabe, T. Taniguchi, G. Zhang, A. Bachtold, A. H. MacDonald and D. K. Efetov: Superconductors, orbital magnets and correlated states in magic-angle bilayer graphene. *Nature* 574, 653 (2019)

65. D. Simpson: Challenges for semiconductor spintronics. *Nature Physics*, 1 (2007)

66. V. V. Kruglyak, S. O. Demokritov and D. Grundler: Magnonics. *Journal of Physics D: Applied Physics* 43, 264001 (2010)

67. N. D. Mermin and H. Wagner: Absence of ferromagnetism or antiferromagnetism in one- or two-dimensional isotropic Heisenberg models. *Physical Review Letters* 17, 1133 (1966)

68. B. Huang, G. Clark, E. Navarro-Moratalla, D. R. Klein, R. Cheng, K. L. Seyler, D. Zhong, E. Schmidgall, M. A. McGuire, D. H. Cobden, W. Yao, D. Xiao, P. Jarillo-Herrero and X. Xu: Layer-dependent ferromagnetism in a van der Waals crystal down to the monolayer limit. *Nature* 546, 270 (2017)

69. P. Huang, P. Zhang, S. Xu, H. Wang, X. Zhang and H. Zhang: Recent advances in two-dimensional ferromagnetism: materials synthesis, physical properties and device applications. *Nanoscale* 12, 2309 (2020)

70. H. Ohno, A. Shen, F. Matsukura, A. Oiwa, A. Endo, S. Katsumoto and Y. Iye: (Ga,Mn)As: A new diluted magnetic semiconductor based on GaAs. *Applied Physics Letters* 69, 363 (1996)

71. D. Chiba, K. Takamura, F. Matsukura and H. Ohno: Effect of low-temperature annealing on (Ga,Mn)As trilayer structures. *Applied Physics Letters* 82, 3020 (2003)

72. K. W. Edmonds, K. Y. Wang, R. P. Campion, A. C. Neumann, N. R. S. Farley, B. L. Gallagher and C. T. Foxon: High-Curie-temperature $Ga_{1-x}Mn_xAs$ obtained by resistance-monitored annealing. *Applied Physics Letters* 81, 4991 (2002)

73. K. Zhang, S. Feng, J. Wang, A. Azcatl, N. Lu, R. Addou, N. Wang, C. Zhou, J. Lerach, V. Bojan, M. J. Kim, L.-Q. Chen, R. M. Wallace, M. Terrones, J. Zhu and J. A. Robinson: Manganese Doping of Monolayer MoS_2: The Substrate Is Critical. *Nano Letters* 15, 6586 (2015)

74. A. Ramasubramaniam and D. Naveh: Mn-doped monolayer MoS 2: An atomically thin dilute magnetic semiconductor. *Physical Review B* 87, 195201 (2013)

75. R. R. Nair, M. Sepioni, I. L. Tsai, O. Lehtinen, J. Keinonen, A. V. Krasheninnikov, T. Thomson, A. K. Geim and I. V. Grigorieva: Spin-half paramagnetism in graphene induced by point defects. *Nature Physics* 8, 199 (2012)

76. M. B. Lundeberg, R. Yang, J. Renard and J. A. Folk: Defect-Mediated Spin Relaxation and Dephasing in Graphene. *Physical Review Letters* 110, 156601 (2013)

77. S. Jiang, L. Li, Z. Wang, K. F. Mak and J. Shan: Controlling magnetism in 2D CrI_3 by electrostatic doping. *Nature Nanotechnology* 13, 549 (2018)

78. B. Huang, G. Clark, D. R. Klein, D. MacNeill, E. Navarro-Moratalla, K. L. Seyler, N. Wilson, M. A. McGuire, D. H. Cobden, X. Di, W. Yao, P. Jarillo-Herrero and X. Xu: Electrical control of 2D magnetism in bilayer CrI3. *Nature Nanotechnology* 13, 544 (2018)

79. Z. Wang, T. Zhang, M. Ding, B. Dong, Y. Li, M. Chen, X. Li, J. Huang, H. Wang, X. Zhao, Y. Li, L. Da, C. Jia, L. Sun, H. Guo, Y. Ye, D. Sun, Y. Chen, T. Yang, J. Zhang, S. Ono, Z. Han and Z. Zhang: Electric-field control of magnetism in a few-layered van der Waals ferromagnetic semiconductor. *Nature Nanotechnology* 13, 554 (2018)

80. Y. Deng, Y. Yu, Y. Song, J. Zhang, N. Z. Wang, Z. Sun, Y. Yi, Y. Z. Wu, S. Wu, J. Zhu, J. Wang, X. H. Chen and Y. Zhang: Gate-tunable room-temperature ferromagnetism in two-dimensional Fe_3GeTe_2. *Nature* 563, 94 (2018)

81. C. Gong, L. Li, Z. Li, H. Ji, A. Stern, Y. Xia, T. Cao, W. Bao, C. Wang, Y. Wang, Z. Q. Qiu, R. J. Cava, S. G. Louie, J. Xia and X. Zhang: Discovery of intrinsic ferromagnetism in two-dimensional van der Waals crystals. *Nature* 546, 265 (2017)

82. M. Bonilla, S. Kolekar, Y. Ma, H. C. Diaz, V. Kalappattil, R. Das, T. Eggers, H. R. Gutiérrez, M.-H. Phan and M. Batzill: Strong room-temperature ferromagnetism in VSe2 monolayers on van der Waals substrates. *Nature Nanotechnology* 13, 289 (2018)

83. M. M. Otrokov, I. I. Klimovskikh, H. Bentmann, A. Zeugner, Z. S. Aliev, S. Gass, A. U. Wolter, A. V. Koroleva, D. Estyunin and A. M. Shikin: Prediction and observation of the first antiferromagnetic topological insulator. *Nature* 576, 416 (2019)

84. M. M. Otrokov, I. P. Rusinov, M. Blanco-Rey, M. Hoffmann, A. Y. Vyazovskaya, S. V. Eremeev, A. Ernst, P. M. Echenique, A. Arnau and E. V. Chulkov: Unique

Thickness-Dependent Properties of the van der Waals Interlayer Antiferromagnet MnBi$_2$Te$_4$ Films. *Physical Review Letters* 122, 107202 (2019)

85. J. Cui, M. Shi, H. Wang, F. Yu, T. Wu, X. Luo, J. Ying and X. Chen: Transport properties of thin flakes of the antiferromagnetic topological insulator MnBi$_2$Te$_4$. *Physical Review B* 99, 155125 (2019)

86. Y. Deng, Y. Yu, M. Z. Shi, J. Wang, X. H. Chen and Y. Zhang: Quantum anomalous Hall effect in intrinsic magnetic topological insulator MnBi$_2$Te$_4$. *Science* 367, 895 (2020)

87. C. Liu, Y. Wang, H. Li, Y. Wu, Y. Li, J. Li, K. He, Y. Xu, J. Zhang and Y. Wang: Robust axion insulator and Chern insulator phases in a two-dimensional antiferromagnetic topological insulator. *Nature Materials* 19, 522 (2020)

88. D. Zhang, M. Shi, T. Zhu, D. Xing, H. Zhang and J. Wang: Topological Axion States in the Magnetic Insulator MnBi$_2$Te$_4$ with the Quantized Magnetoelectric Effect. *Physical Review Letters* 122, 206401 (2019)

89. Y. Gong, J. Guo, J. Li, K. Zhu, M. Liao, X. Liu, Q. Zhang, L. Gu, L. Tang, X. Feng, D. Zhang, W. Li, C. Song, L. Wang, P. Yu, X. Chen, Y. Wang, H. Yao, W. Duan, Y. Xu, S.-C. Zhang, X. Ma, Q.-K. Xue and K. He: Experimental Realization of an Intrinsic Magnetic Topological Insulator. *Chinese Physics Letters* 36, 076801 (2019)

90. J. Li, Y. Li, S. Du, Z. Wang, B.-L. Gu, S.-C. Zhang, K. He, W. Duan and Y. Xu: Intrinsic magnetic topological insulators in van der Waals layered MnBi$_2$Te$_4$-family materials. *Science Advances* 5, eaaw5685 (2019)

91. J. Ge, Y. Liu, J. Li, H. Li, T. Luo, Y. Wu, Y. Xu and J. Wang: High-Chern-Number and High-Temperature Quantum Hall Effect without Landau Levels. *National Science Review*, nwaa089 (2020)

92. S. H. Lee, Y. Zhu, Y. Wang, L. Miao, T. Pillsbury, H. Yi, S. Kempinger, J. Hu, C. A. Heikes, P. Quarterman, W. Ratcliff, J. A. Borchers, H. Zhang, X. Ke, D. Graf, N. Alem, C.-Z. Chang, N. Samarth and Z. Mao: Spin scattering and noncollinear spin structure-induced intrinsic anomalous Hall effect in antiferromagnetic topological insulator MnBi$_2$Te$_4$. *Physical Review Research* 1, 012011 (2019)

93. J. Q. Yan, S. Okamoto, M. A. McGuire, A. F. May, R. J. McQueeney and B. C. Sales: Evolution of structural, magnetic, and transport properties in MnBi$_{2-x}$Sb$_x$Te$_4$. *Physical Review B* 100, 104409 (2019)

94. J. Q. Yan, Q. Zhang, T. Heitmann, Z. Huang, K. Y. Chen, J. G. Cheng, W. Wu, D. Vaknin, B. C. Sales and R. J. McQueeney: Crystal growth and magnetic structure of MnBi$_2$Te$_4$. *Physical Review Materials* 3, 064202 (2019)

95. E. McCann and M. Koshino: The electronic properties of bilayer graphene. *Reports on Progress in Physics* 76, 056503 (2013)

96. J.-K. Lee, J.-G. Kim, K. P. S. S. Hembram, Y.-I. Kim, B.-K. Min, Y. Park, J.-K. Lee, D. J. Moon, W. Lee, S.-G. Lee and P. John: The Nature of Metastable AA' Graphite: Low Dimensional Nano- and Single-Crystalline Forms. *Scientific Reports* 6, 39624 (2016)

97. R. Saito, G. Dresselhaus and M. S. Dresselhaus: Physical Properties of Carbon Nanotubes. London: Imperial College Press, (1998)

98. J. C. Slonczewski and P. R. Weiss: Band Structure of Graphite. *Physical Review* 109, 272 (1958)

99. A. B. Kuzmenko, I. Crassee, D. van der Marel, P. Blake and K. S. Novoselov: Determination of the gate-tunable band gap and tight-binding parameters in bilayer graphene using infrared spectroscopy. *Physical Review B* 80, 165406 (2009)

100. K. von Klitzing, G. Dorda and M. Pepper: New Method for High-Accuracy Determination of the Fine-Structure Constant Based on Quantized Hall Resistance. *Physical Review Letters* 45, 494 (1980)

101. D. Tong: The Quantum Hall Effect. *TIFR Infosys Lectures.* *http://www.damtp.cam.ac.uk/user/tong/qhe.html* (2016)

102. S. Meng: Integer Quantum Hall Effect. *Proseminar in Theoretical Physics, Departement Physik ETH Zürich* (2018)

103. E. McCann: Asymmetry gap in the electronic band structure of bilayer graphene. *Physical Review B* 74, 161403 (2006)

104. F. Guinea, A. H. Castro Neto and N. M. R. Peres: Electronic states and Landau levels in graphene stacks. *Physical Review B* 73, 245426 (2006)

105. J. Li, Y. Tupikov, K. Watanabe, T. Taniguchi and J. Zhu: Effective Landau Level Diagram of Bilayer Graphene. *Physical Review Letters* 120, 047701 (2018)

106. J. Velasco Jr, Y. Lee, F. Zhang, K. Myhro, D. Tran, M. Deo, D. Smirnov, A. H. Macdonald and C. N. Lau: Competing ordered states with filling factor two in bilayer graphene. *Nature Communications* 5, 1 (2014)

107. M. Kharitonov: Canted Antiferromagnetic Phase of the ν=0Quantum Hall State in Bilayer Graphene. *Physical Review Letters* 109, 046803 (2012)

108. B. M. Hunt, J. I. A. Li, A. A. Zibrov, L. Wang, T. Taniguchi, K. Watanabe, J. Hone, C. R. Dean, M. Zaletel, R. C. Ashoori and A. F. Young: Direct measurement of discrete valley and orbital quantum numbers in bilayer graphene. *Nature Communications* 8, 948 (2017)

109. B. E. Feldman, J. Martin and A. Yacoby: Broken-symmetry states and divergent resistance in suspended bilayer graphene. *Nature Physics* 5, 889 (2009)

110. Y. Zhao, P. Cadden-Zimansky, Z. Jiang and P. Kim: Symmetry Breaking in the Zero-Energy Landau Level in Bilayer Graphene. *Physical review letters* 104, 066801 (2010)

111. R. T. Weitz, M. T. Allen, B. E. Feldman, J. Martin and A. Yacoby: Broken-Symmetry States in Doubly Gated Suspended Bilayer Graphene. *Science* 330, 812 (2010)

112. P. Maher, C. R. Dean, A. F. Young, T. Taniguchi, K. Watanabe, K. L. Shepard, J. Hone and P. Kim: Evidence for a spin phase transition at charge neutrality in bilayer graphene. *Nature Physics* 9, 154 (2013)

113. K. Lee, B. Fallahazad, J. Xue, D. C. Dillen, K. Kim, T. Taniguchi, K. Watanabe and E. Tutuc: Chemical potential and quantum Hall ferromagnetism in bilayer graphene. *Science* 345, 58 (2014)

114. A. Kou, B. E. Feldman, A. J. Levin, B. I. Halperin, K. Watanabe, T. Taniguchi and A. Yacoby: Electron-hole asymmetric integer and fractional quantum Hall effect in bilayer graphene. *Science* 345, 55 (2014)

115. P. Maher, L. Wang, Y. D. Gao, C. Forsythe, T. Taniguchi, K. Watanabe, D. Abanin, Z. Papic, P. Cadden-Zimansky, J. Hone, P. Kim and C. R. Dean: Tunable fractional quantum Hall phases in bilayer graphene. *Science* 345, 61 (2014)

116. J. I. A. Li, C. Tan, S. Chen, Y. Zeng, T. Taniguchi, K. Watanabe, J. Hone and C. R. Dean: Even-denominator fractional quantum Hall states in bilayer graphene. *Science* 358, 648 (2017)

117. A. K. Geim and I. V. Grigorieva: Van der Waals heterostructures. *Nature* 499, 419 (2013)

118. C. H. Lee, G. H. Lee, A. M. van der Zande, W. C. Chen, Y. L. Li, M. Y. Han, X. Cui, G. Arefe, C. Nuckolls, T. F. Heinz, J. Guo, J. Hone and P. Kim: Atomically thin p-n junctions with van der Waals heterointerfaces. *Nature Nanotechnology* 9, 676 (2014)

119. P. Rivera, J. R. Schaibley, A. M. Jones, J. S. Ross, S. F. Wu, G. Aivazian, P. Klement, K. Seyler, G. Clark, N. J. Ghimire, J. Q. Yan, D. G. Mandrus, W. Yao and X. D. Xu: Observation of long-lived interlayer excitons in monolayer $MoSe_2$-WSe_2 heterostructures. *Nature Communications* 6, 6242 (2015)

120. T. Roy, M. Tosun, X. Cao, H. Fang, D. H. Lien, P. D. Zhao, Y. Z. Chen, Y. L. Chueh, J. Guo and A. Javey: Dual-Gated MoS_2/WSe_2 van der Waals Tunnel Diodes and Transistors. *Acs Nano* 9, 2071 (2015)

121. Y. K. Luo, J. S. Xu, T. C. Zhu, G. Z. Wu, E. J. McCormick, W. B. Zhan, M. R. Neupane and R. K. Kawakami: Opto-Valleytronic Spin Injection in Monolayer MoS2/Few-Layer Graphene Hybrid Spin Valves. *Nano Letters* 17, 3877 (2017)

122. G. H. Lee and H. J. Lee: Proximity coupling in superconductor-graphene heterostructures. *Rep Prog Phys* 81, 056502 (2018)

123. Z. Y. Wang, C. Tang, R. Sachs, Y. Barlas and J. Shi: Proximity-Induced Ferromagnetism in Graphene Revealed by the Anomalous Hall Effect. *Physical Review Letters* 114, 016603 (2015)

124. P. Wei, S. Lee, F. Lemaitre, L. Pinel, D. Cutaia, W. Cha, F. Katmis, Y. Zhu, D. Heiman, J. Hone, J. S. Moodera and C. T. Chen: Strong interfacial exchange field in the graphene/EuS heterostructure. *Nature Materials* 15, 711 (2016)

125. C. L. Kane and E. J. Mele: Quantum spin Hall effect in graphene. *Physical Review Letters* 95, 226801 (2005)

126. Z. H. Qiao, W. Ren, H. Chen, L. Bellaiche, Z. Y. Zhang, A. H. MacDonald and Q. Niu: Quantum Anomalous Hall Effect in Graphene Proximity Coupled to an Antiferromagnetic Insulator. *Physical Review Letters* 112, 116404 (2014)

127. W. Han, R. K. Kawakami, M. Gmitra and J. Fabian: Graphene spintronics. *Nature Nanotechnology* 9, 794 (2014)

128. M. Gmitra and J. Fabian: Graphene on transition-metal dichalcogenides: A platform for proximity spin-orbit physics and optospintronics. *Physical Review B* 92, 155403 (2015)

129. B. W. Yang, E. Molina, J. Kim, D. Barroso, M. Lohmann, Y. W. Liu, Y. D. Xu, R. Q. Wu, L. Bartels, K. Watanabe, T. Taniguchi and J. Shi: Effect of Distance on Photoluminescence Quenching and Proximity-Induced Spin-Orbit Coupling in Graphene/WSe_2 Heterostructures. *Nano Letters* 18, 3580 (2018)

130. M. Kumagai and T. Takagahara: Excitonic and nonlinear-optical properties of dielectric quantum-well structures. *Physical Review B* 40, 12359 (1989)

131. A. K. M. Newaz, Y. S. Puzyrev, B. Wang, S. T. Pantelides and K. I. Bolotin: Probing charge scattering mechanisms in suspended graphene by varying its dielectric environment. *Nature Communications* 3, 734 (2012)

132. Y. X. Lin, X. Ling, L. L. Yu, S. X. Huang, A. L. Hsu, Y. H. Lee, J. Kong, M. S. Dressehaus and T. Palacios: Dielectric Screening of Excitons and Trions in Single-Layer MoS2. *Nano Letters* 14, 5569 (2014)

133. A. Raja, A. Chaves, J. Yu, G. Arefe, H. M. Hill, A. F. Rigosi, T. C. Berkelbach, P. Nagler, C. Schüller, T. Korn, C. Nuckolls, J. Hone, L. E. Brus, T. F. Heinz, D. R. Reichman and A. Chernikov: Coulomb engineering of the bandgap and excitons in two-dimensional materials. *Nature Communications* 8, 15251 (2017)

134. J. Jung, F. Zhang and A. H. MacDonald: Lattice theory of pseudospin ferromagnetism in bilayer graphene: Competing interaction-induced quantum Hall states. *Physical Review B* 83, 115408 (2011)

135. J. Velasco Jr, L. Jing, W. Bao, Y. Lee, P. Kratz, V. Aji, M. Bockrath, C. N. Lau, C. Varma, R. Stillwell, D. Smirnov, F. Zhang, J. Jung and A. H. MacDonald: Transport spectroscopy of symmetry-broken insulating states in bilayer graphene. *Nature Nanotechnology* 7, 156 (2012)

136. M. Kharitonov: Antiferromagnetic state in bilayer graphene. *Physical Review B* 86, 195435 (2012)

137. M. Kharitonov: Canted Antiferromagnetic Phase of the v=0 Quantum Hall State in Bilayer Graphene. *Physical Review Letters* 109, 046803 (2012)

138. J. Velasco, Y. Lee, F. Zhang, K. Myhro, D. Tran, M. Deo, D. Smirnov, A. H. MacDonald and C. N. Lau: Competing ordered states with filling factor two in bilayer graphene. *Nature Communications* 5, 4550 (2014)

139. J. Li, H. Fu, Z. Yin, K. Watanabe, T. Taniguchi and J. Zhu: Metallic Phase and Temperature Dependence of the v=0 Quantum Hall State in Bilayer Graphene. *Physical Review Letters* 122, 097701 (2019)

140. E. McCann and V. I. Fal'ko: Landau-level degeneracy and quantum hall effect in a graphite bilayer. *Physical Review Letters* 96, 086805 (2006)

141. J. Lambert and R. Côté: Quantum Hall ferromagnetic phases in the Landau level N=0 of a graphene bilayer. *Physical review B* 87, 115415 (2013)

142. G. Murthy, E. Shimshoni and H. A. Fertig: Spin-valley coherent phases of the v = 0 quantum Hall state in bilayer graphene. *Physical Review B* 96, 245125 (2017)

143. K. Shizuya: Structure and the Lamb-shift-like quantum splitting of the pseudo-zero-mode Landau levels in bilayer graphene. *Physical Review B* 86, 045431 (2012)

144. E. H. Rezayi and S. H. Simon: Breaking of Particle-Hole Symmetry by Landau Level Mixing in the v=5/2 Quantized Hall State. *Physical Review Letters* 106, 116801 (2011)

145. Z. Papic and D. A. Abanin: Topological Phases in the Zeroth Landau Level of Bilayer Graphene. *Physical Review Letters* 112 (2014)

146. A. A. Zibrov, C. Kometter, H. Zhou, E. M. Spanton, T. Taniguchi, K. Watanabe, M. P. Zaletel and A. F. Young: Tunable interacting composite fermion phases in a half-filled bilayer-graphene Landau level. *Nature* 549, 360 (2017)

147. J. Martin, B. E. Feldman, R. T. Weitz, M. T. Allen and A. Yacoby: Local compressibility measurements of correlated states in suspended bilayer graphene. *Physical review letters* 105, 256806 (2010)

148. J. Li, H. Wen, K. Watanabe, T. Taniguchi and J. Zhu: Gate-Controlled Transmission of Quantum Hall Edge States in Bilayer Graphene. *Physical Review Letters* 120, 057701 (2018)

149. W. Bao, J. Velasco, F. Zhang, L. Jing, B. Standley, D. Smirnov, M. Bockrath, A. H. MacDonald and C. N. Lau: Evidence for a spontaneous gapped state in ultraclean bilayer graphene. *Proceedings of the National Academy of Sciences* 109, 10802 (2012)

150. R. V. Gorbachev, F. V. Tikhonenko, A. S. Mayorov, D. W. Horsell and A. K. Savchenko: Weak localization in bilayer graphene. *Physical Review Letters* 98, 176805 (2007)

151. S. Tang, H. Wang, Y. Zhang, A. Li, H. Xie, X. Liu, L. Liu, T. Li, F. Huang, X. Xie and M. Jiang: Precisely aligned graphene grown on hexagonal boron nitride by catalyst free chemical vapor deposition. *Scientific Reports* 3, 2666 (2013)

152. L. Plucinski, R. L. Johnson, B. J. Kowalski, K. Kopalko, B. A. Orlowski, Z. D. Kovalyuk and G. V. Lashkarev: Electronic band structure of GaSe(0001): Angle-resolved photoemission and ab initiotheory. *Physical Review B* 68, 125304 (2003)

153. M.-W. Chen, H. Kim, D. Ovchinnikov, A. Kuc, T. Heine, O. Renault and A. Kis: Large-grain MBE-grown GaSe on GaAs with a Mexican hat- like valence band dispersion. *npj 2D Materials and Applications* 2, 2 (2018)

154. X. Li, L. Basile, B. Huang, C. Ma, J. Lee, I. V. Vlassiouk, A. A. Puretzky, M.-W. Lin, M. Yoon, M. Chi, J. C. Idrobo, C. M. Rouleau, B. G. Sumpter, D. B. Geohegan and K. Xiao: Van der Waals Epitaxial Growth of Two-Dimensional Single-Crystalline GaSe Domains on Graphene. *ACS Nano* 9, 8078 (2015)

155. A. Nakanishi and T. Matsubura: Optimized Bond Orbital Model for III-VI Compounds. *Journal of the Physical Society of Japan* 51, 3219 (1982)

156. C. T. T Tambo: Barrier formation at Cu, Ag and Au-GaSe layered semiconductors. *Surface Science* 222, 343 (1989)

157. K. Ueno, H. Abe, K. Saiki and A. Koma: Heteroepitaxy of Layered Semiconductor GaSe on a GaAs(111)B Surface. *Japanese Journal of Applied Physics* 30, L1352 (1991)

158. J. Keeling: Quantum Magnetism. *https://www.st-andrews.ac.uk/~jmjk/keeling/teaching/magnetism-notes.pdf*

159. D. Errandonea, A. Segura, F. J. Manjón, A. Chevy, E. Machado, G. Tobias, P. Ordejón and E. Canadell: Crystal symmetry and pressure effects on the valence band structure of γ-InSe and ε-GaSe: Transport measurements and electronic structure calculations. *Physical Review B* 71, 125206 (2005)

160. D. V. Rybkovskiy, A. V. Osadchy and E. D. Obraztsova: Transition from parabolic to ring-shaped valence band maximum in few-layer GaS, GaSe, and InSe. *Physical Review B* 90, 235302 (2014)

161. D. A. Bandurin, A. V. Tyurnina, G. L. Yu, A. Mishchenko, V. Zólyomi, S. V. Morozov, R. K. Kumar, R. V. Gorbachev, Z. R. Kudrynskyi, S. Pezzini, Z. D. Kovalyuk, U. Zeitler, K. S. Novoselov, A. Patanè, L. Eaves, I. V. Grigorieva, V. I. Fal'ko, A. K. Geim and Y. Cao: High electron mobility, quantum Hall effect and anomalous optical response in atomically thin InSe. *Nature Nanotechnology*, 1 (2016)

162. E. Mooser and M. Schlüter: The Band-Gap Excitons in Gallium Selenide. *Il Nuovo Cimento B* 18, 164 (1973)

163. J. Y. Tan, A. Avsar, J. Balakrishnan, G. K. W. Koon, T. Taychatanapat, E. C. T. O'Farrell, K. Watanabe, T. Taniguchi, G. Eda, A. H. Castro Neto and B. Özyilmaz:

Electronic transport in graphene-based heterostructures. *Applied Physics Letters* 104, 183504 (2014)

164. S. I. Drapak, S. V. Gavrylyuk, Z. D. Kovalyuk and O. S. Lytvyn: Native oxide emerging of the cleavage surface of gallium selenide due to prolonged storage. *Semiconductors* 42, 414 (2008)

165. C. Handschin, B. Fülöp, P. Makk, S. Blanter, M. Weiss, K. Watanabe, T. Taniguchi, S. Csonka and C. Schonenberger: Point contacts in encapsulated graphene. *Applied Physics Letters* 107, 183108 (2015)

166. A. Tiwari and M. Syväjärvi: Advanced 2D Materials. John Wiley & Sons, (2016)

167. W.-C. Huang, S.-H. Su, Y.-K. Hsu, C.-C. Wang and C.-S. Chang: Al Schottky contact on p-GaSe. *Superlattices and Microstructures* 40, 644 (2006)

168. S. Duman, B. Gürbulak, S. Doğan and A. Türüt: Capacitance and conductance-frequency characteristics of Au-Sb/p-GaSe:Gd Schottky barrier diode. *Vaccum* 85, 798 (2011)

169. T. J. Drummond: work function_osti.gov. *Journal of Applied Physics*, SAND99 (1999)

170. J.-K. Ho, C.-S. Jong, C. C. Chiu, C.-N. Huang, K.-K. Shih, L.-C. Chen, F.-R. Chen and J.-J. Kai: Low-resistance ohmic contacts to p-type GaN achieved by the oxidation of Ni/Au films. *Journal of Applied Physics* 86, 4491 (1999)

171. S. Chuang, C. Battaglia, A. Azcatl, S. McDonnell, J. S. Kang, X. Yin, M. Tosun, R. Kapadia, H. Fang, R. M. Wallace and A. Javey: MoS_2 P-type Transistors and Diodes Enabled by High Work Function MoO_x Contacts. *Nano Letters* 14, 1337 (2014)

172. M. Yamamoto, S. Nakaharai, K. Ueno and K. Tsukagoshi: Self-Limiting Oxides on WSe_2 as Controlled Surface Acceptors and Low-Resistance Hole Contacts. *Nano Letters* 16, 2720 (2016)

173. K. Zou, X. Hong, D. Keefer and J. Zhu: Deposition of High-Quality HfO_2 on Graphene and the Effect of Remote Oxide Phonon Scattering. *Physical Review Letters* 105, 126601 (2010)

174. S. R. Thomas, G. Adamopoulos, Y.-H. Lin, H. Faber, L. Sygellou, E. Stratakis, N. Pliatsikas, P. A. Patsalas and T. D. Anthopoulos: High electron mobility thin-film transistors based on Ga_2O_3 grown by atmospheric ultrasonic spray pyrolysis at low temperatures. *Applied Physics Letters* 105, 092105 (2014)

175. Y. Koide, T. Maeda, T. Kawakami, S. Fujita, T. Uemura, N. Shibata and M. Murakami: Effects of annealing in an oxygen ambient on electrical properties of ohmic contacts to p-type GaN. *Journal of Electronic Materials* 28, 341 (1999)

176. H. W. Jang, S. Y. Kim and J.-L. Lee: Mechanism for Ohmic contact formation of oxidized Ni/Au on p-type GaN. *Journal of Applied Physics* 94, 1748 (2003)

177. J. O. Song, J.-S. Ha and T.-Y. Seong: Ohmic-Contact Technology for GaN-Based Light-Emitting Diodes: Role of P-Type Contact. *IEEE Transactions on Electron Devices* 57, 42 (2010)

178. T. Maeda, Y. Koide and M. Murakami: Effects of NiO on electrical properties of NiAu-based ohmic contacts for p-type GaN. *Applied Physics Letters* 75, 4145 (1999)

179. A. Herz, D. Wang, T. Kups and P. Schaaf: Solid-state dewetting of Au/Ni bilayers: The effect of alloying on morphology evolution. *Journal of Applied Physics* 116, 044307 (2014)

180. G. Y. Robinson: Metallurgical and electrical properties of alloyed Ni/Au-Ge films on n-type GaAs. *Solid State Electronics* 18, 331 (1975)

181. W. T. Anderson Jr, A. Christou and J. E. Davey: Smooth and continuous Ohmic contacts to GaAs using epitaxial Ge films. *Journal of Applied Physics* 49, 2998 (1978)

182. T. S. Kuan, P. E. Batson, T. N. Jackson, H. Rupprecht and E. L. Wilkie: Electron microscope studies of an alloyed Au/Ni/Au-Ge ohmic contact to GaAs. *Journal of Applied Physics* 54, 6952 (1983)

183. T. Sands, V. G. Keramidas, A. J. Yu, K. M. Yu, R. Gronsky and J. Washburn: Ni, Pd, and Pt on GaAs: A comparative study of interfacial structures, compositions, and reacted film morphologies. *Journal of Materials Research* 2, 262 (1987)

184. H. Ishikawa, S. Kobayashi, Y. Koidea, S. Yamasaki, S. Nagai, J. Umezaki, M. Koike and M. Murakami: Effects of surface treatments and metal work functions on electrical properties at p-GaN/metal interfaces. *Journal of Applied Physics*, 1315 (1997)

185. M. Z. Hasan and C. L. Kane: Colloquium: Topological insulators. *Reviews of Modern Physics* 82, 3045 (2010)

186. C.-Z. Chang, J. Zhang, X. Feng, J. Shen, Z. Zhang, M. Guo, K. Li, Y. Ou, P. Wei, L.-L. Wang, Z.-Q. Ji, Y. Feng, S. Ji, X. Chen, J. Jia, X. Dai, Z. Fang, S.-C. Zhang, K. He, Y. Wang, L. Lu, X.-C. Ma and Q.-K. Xue: Experimental Observation of the Quantum Anomalous Hall Effect in a Magnetic Topological Insulator. *Science* 340, 167 (2013)

187. C.-X. Liu, S.-C. Zhang and X.-L. Qi: The Quantum Anomalous Hall Effect: Theory and Experiment. *Annual Review of Condensed Matter Physics* 7, 301 (2016)

188. N. Nagaosa and Y. Tokura: Topological properties and dynamics of magnetic skyrmions. *Nature Nanotechnology* 8, 899 (2013)

189. A. Fert, N. Reyren and V. Cros: Magnetic skyrmions: advances in physics and potential applications. *Nature Reviews Materials* 2, 17031 (2017)

190. Y. Taguchi, Y. Oohara, H. Yoshizawa, N. Nagaosa and Y. Tokura: Spin chirality, Berry phase, and anomalous Hall effect in a frustrated ferromagnet. *Science* 291, 2573 (2001)

191. A. Neubauer, C. Pfleiderer, B. Binz, A. Rosch, R. Ritz, P. G. Niklowitz and P. Boni: Topological Hall Effect in the A Phase of MnSi. *Physical Review Letters* 102 (2009)

192. X. Z. Yu, N. Kanazawa, Y. Onose, K. Kimoto, W. Z. Zhang, S. Ishiwata, Y. Matsui and Y. Tokura: Near room-temperature formation of a skyrmion crystal in thin-films of the helimagnet FeGe. *Nature Materials* 10, 106 (2011)

193. S. X. Huang and C. L. Chien: Extended Skyrmion Phase in Epitaxial FeGe (111) Thin Films. *Physical Review Letters* 108, 267201 (2012)

194. S. Heinze, K. von Bergmann, M. Menzel, J. Brede, A. Kubetzka, R. Wiesendanger, G. Bihlmayer and S. Blügel: Spontaneous atomic-scale magnetic skyrmion lattice in two dimensions. *Nature Physics* 7, 713 (2011)

195. J. Matsuno, N. Ogawa, K. Yasuda, F. Kagawa, W. Koshibae, N. Nagaosa, Y. Tokura and M. Kawasaki: Interface-driven topological Hall effect in SrRuO$_3$-SrIrO$_3$ bilayer. *Science Advances* 2, e1600304 (2016)
196. J. Jiang, D. Xiao, F. Wang, J.-H. Shin, D. Andreoli, J. Zhang, R. Xiao, Y.-F. Zhao, M. Kayyalha and L. Zhang: Concurrence of quantum anomalous Hall and topological Hall effects in magnetic topological insulator sandwich heterostructures. *Nature Materials* 19, 732 (2020)
197. J. Gallagher, K. Meng, J. Brangham, H. Wang, B. Esser, D. McComb and F. Yang: Robust zero-field skyrmion formation in FeGe epitaxial thin films. *Physical review letters* 118, 027201 (2017)
198. W. Wang, M. W. Daniels, Z. Liao, Y. Zhao, J. Wang, G. Koster, G. Rijnders, C.-Z. Chang, D. Xiao and W. Wu: Spin chirality fluctuation in two-dimensional ferromagnets with perpendicular magnetic anisotropy. *Nature Materials* 18, 1054 (2019)
199. T. Song, X. Cai, M. W.-Y. Tu, X. Zhang, B. Huang, N. P. Wilson, K. L. Seyler, L. Zhu, T. Taniguchi, K. Watanabe, M. A. McGuire, D. H. Cobden, D. Xiao, W. Yao and X. Xu: Giant tunneling magnetoresistance in spin-filter van der Waals heterostructures. *Science* 360, 1214 (2018)
200. W. Xing, L. Qiu, X. Wang, Y. Yao, Y. Ma, R. Cai, S. Jia, X. C. Xie and W. Han: Magnon Transport in Quasi-Two-Dimensional van der Waals Antiferromagnets. *Physical Review X* 9, 011026 (2019)
201. S. V. Eremeev, M. M. Otrokov and E. V. Chulkov: Competing rhombohedral and monoclinic crystal structures in MnPn$_2$Ch$_4$ compounds: An ab-initio study. *Journal of Alloys and Compounds* 709, 172 (2017)
202. R. C. Vidal, A. Zeugner, J. I. Facio, R. Ray, M. H. Haghighi, A. U. B. Wolter, L. T. C. Bohorquez, F. Caglieris, S. Moser, T. Figgemeier, T. R. F. Peixoto, H. B. Vasili, M. Valvidares, S. Jung, C. Cacho, A. Alfonsov, K. Mehlawat, V. Kataev, C. Hess, M. Richter, B. Büchner, J. v. d. Brink, M. Ruck, F. Reinert, H. Bentmann and A. Isaeva: Topological electronic structure and intrinsic magnetization in MnBi$_4$Te$_7$: a Bi$_2$Te$_3$-derivative with a periodic Mn sublattice. *aXiv:1906.08394* (2019)
203. C. Hu, X. Zhou, P. Liu, J. Liu, P. Hao, E. Emmanouilidou, H. Sun, Y. Liu, H. Brawer, A. P. Ramirez, H. Cao, Q. Liu, D. Dessau and N. Ni: A van der Waals antiferromagnetic topological insulator with weak interlayer magnetic coupling. *Nature Communications* 11, 97 (2020)
204. T. Murakami, Y. Nambu, T. Koretsune, X. Y. Gu, T. Yamamoto, C. M. Brown and H. Kageyama: Realization of interlayer ferromagnetic interaction in MnSb$_2$Te$_4$ toward the magnetic Weyl semimetal state. *Physical Review B* 100, 195103 (2019)
205. H. Weng, X. Dai and Z. Fang: Topological semimetals predicted from first-principles calculations. *Journal of Physics: Condensed Matter* 28, 303001 (2016)
206. Y. Chen, Y.-W. Chuang, S. H. Lee, Y. Zhu, K. Honz, Y. Guan, Y. Wang, K. Wang, Z. Mao, C. Heikes, P. Quarterman, P. Zajdel, J. A. Borchers, W. Ratcliff Ii and J. Zhu: Ferromagnetism in van der Waals compound MnSb$_{1.8}$Bi$_{0.2}$Te$_4$. *Physical Review Materials* 4, 064411 (2020)
207. N. Nagaosa, J. Sinova, S. Onoda, A. H. Macdonald and N. P. Ong: Anomalous Hall effect. *Reviews of Modern Physics* 82, 1539 (2010)

208. Y. Moritomo, Y. Tomioka, A. Asamitsu, Y. Tokura and Y. Matsui: Magnetic and electronic properties in hole-doped manganese oxides with layered structures: $La_{1-x}Sr_{1+x}MnO_4$. *Physical Review B* 51, 3297 (1995)

209. J. S. Gardner, M. J. P. Gingras and J. E. Greedan: Magnetic pyrochlore oxides. *Reviews of Modern Physics* 82, 53 (2010)

210. J. Wu and C. Leighton: Glassy ferromagnetism and magnetic phase separation in $La_{1-x}Sr_xCoO_3$. *Physical Review B* 67, 174408 (2003)

211. J. D. Bocarsly, C. Heikes, C. M. Brown, S. D. Wilson and R. Seshadri: Deciphering structural and magnetic disorder in the chiral skyrmion host materials $Co_xZn_yMn_z$ (x+y+z=20). *Physical Review Materials* 3, 014402 (2019)

212. D. Boldrin and A. S. E. Wills: Anomalous Hall Effect in Geometrically Frustrated Magnets. *Advances in Condensed Matter Physics* 2012, 615295 (2012)

213. H. Kawamura: Anomalous Hall Effect as a Probe of the Chiral Order in Spin Glasses. *Physical Review Letters* 90, 047202 (2003)

214. H. Chen, Q. Niu and A. H. Macdonald: Anomalous Hall Effect Arising from Noncollinear Antiferromagnetism. *Physical Review Letters* 112, 017205 (2014)

215. Y. S. Hor, P. Roushan, H. Beidenkopf, J. Seo, D. Qu, J. G. Checkelsky, L. A. Wray, D. Hsieh, Y. Xia, S. Y. Xu, D. Qian, M. Z. Hasan, N. P. Ong, A. Yazdani and R. J. Cava: Development of ferromagnetism in the doped topological insulator $Bi_{2-x}Mn_xTe_3$. *Physical Review B* 81, 195203 (2010)

216. J. S. Lee, A. Richardella, D. W. Rench, R. D. Fraleigh, T. C. Flanagan, J. A. Borchers, J. Tao and N. Samarth: Ferromagnetism and spin-dependent transport in n-type Mn-doped bismuth telluride thin films. *Physical Review B* 89, 174425 (2014)

217. D. Vaknin, D. M. Pajerowski, D. L. Schlagel, K. W. Dennis and R. McQueeney: Two-dimensional ordering and collective magnetic excitations in the dilute ferromagnetic topological insulator (Bi0.95 Mn0.05)2 Te3. *Physical Review B* 99, 220404(R) (2019)

218. A. F. May, S. Calder, D. S. Parker, B. C. Sales and M. A. McGuire: Competing magnetic ground states and their coupling to the crystal lattice in $CuFe_2Ge_2$. *Scientific Reports* 6, 35325 (2016)

219. D. Meng, H. Guo, Z. Cui, C. Ma, J. Zhao, J. Lu, H. Xu, Z. Wang, X. Hu, Z. Fu, R. Peng, J. Guo, X. Zhai, G. J. Brown, R. Knize and Y. Lu: Strain-induced high-temperature perovskite ferromagnetic insulator. *PNAS* 115, 2873 (2018)

220. A. D. Smith, F. Niklaus, A. Paussa, S. Vaziri, a. C. Fischer, M. Sterner, F. Forsberg, A. Delin, D. Esseni, P. Palestri, M. Ostling and M. C. Lemme: Electromechanical Piezoresistive Sensing in Suspended Graphene Membranes. *Nano Letters* 13, 3237 (2013)

221. M. Aslani, C. M. Garner, S. Kumar, D. Nordlund, P. Pianetta and Y. Nishi: Characterization of electronic structure of periodically strained graphene. *Applied Physics Letters* 107, 183507 (2015)

222. D. M. Parks: Lecture 7: Elements of Continuum Elasticity. In: *MIT OpenCourseWare, Mechanics and Materials II*. (2004)

223. P. Burnley. *https://serc.carleton.edu/NAGTWorkshops/mineralogy/mineral_physics/tensors.html#Strain,2019*

224. D. Damjanovic: Ferroelectric, dielectric and piezoelectric properties of ferroelectric thin films and ceramics. *Reports on Progress in Physics* 61, 1267 (1998)
225. Y.-C. Chen, C.-K. Cheng and S.-C. Shen: Design and Fabrication of a Displacement Sensor Using Screen Printing Technology and Piezoelectric Nanofibers in d33 Mode. *Sensors and Materials* 31, 233 (2019)
226. I. Kanno: Piezoelectric MEMS: Ferroelectric thin films for MEMS applications. *Japanese Journal of Applied Physics* 57, 040101 (2018)
227. X. Zhu: Piezoelectric ceramics materials: Processing, Properties, characterization and applications. (2009)
228. J. C. Burfoot and G. W. Taylor: Polar Dielectrics and Their Applications. London: Macmillan, (1979)
229. J. Sirohi and I. Chopra: Fundamental Understanding of Piezoelectric Strain Sensors. *Journal of Intelligent Material Systems and Structures* 11, 246 (2000)
230. B. Jaffe, W. R. C. Jr. and H. Jaffe: Piezoelectric Ceramics. *Academic Press, New York* (1971)
231. B. Noheda, J. A. Gonzalo, L. E. Cross, R. Guo, S. E. Park, D. E. Cox and G. Shirane: Tetragonal-to-monoclinic phase transition in a ferroelectric perovskite: The structure of $PbZr_{0.52}Ti_{0.48}O_3$. *Physical Review B* 61, 8687 (2000)
232. C. A. Randall, A. Kelnberger, G. Y. Yang, R. E. Eitel and T. R. Shrout: High Strain Piezoelectric Multilayer Actuators—A Material Science and Engineering Challenge. *Journal of Electroceramics* 14, 177 (2005)
233. K. Carl and K. H. Härdtl: On the origin of the maximum in the electromechanical activity in $Pb(Zr_xTi_{1-x})O_3$ ceramies near the morphotropic phase boundary. *physica status solidi a* 8, 87 (1971)
234. K. H. Yoon and H. R. Lee: Electric-field-induced strain and piezoelectric properties near the morphotropic phase boundary of $Pb(Mg_{1/3}Nb_{2/3})O_3$–$PbZrO_3$–$PbTiO_3$ ceramics. *Journal of Applied Physics* 89, 3915 (2001)
235. S.-E. Park and T. R. Shrout: Ultrahigh strain and piezoelectric behavior in relaxor based ferroelectric single crystals. *Journal of Applied Physics* 82, 1804 (1997)
236. S. Datta: Piezoelectric Materials: Crystal Orientation and Poling Direction. *https://www.comsol.com/blogs/piezoelectric-materials-crystal-orientation-poling-direction/*
237. S. J. Gross: Micromachined Switches and Cantilever Actuators based on Piezoelectric Lead Zirconate Titanate (PZT). In: *PhD Dissertation, The Pennsylvania State University*. (2004)
238. Dielectric and piezoelectric properties of soft piezoelectrics. *TRS Ceramics, www.trsceramics.com*
239. M. Oikawa and K. Toda: Preparation of Pb(Zr,Ti)O 3thin films by an electron beam evaporation technique. *Applied Physics Letters* 29, 491 (1976)
240. S. B. Krupanidhi, N. Maffei, M. Sayer and K. El Assal: rf planar magnetron sputtering and characterization of ferroelectric Pb(Zr,Ti)O 3films. *Journal of Applied Physics* 54, 6601 (1983)
241. R. A. Wolf and S. Trolier-McKinstry: Temperature dependence of the piezoelectric response in lead zirconate titanate films. *Journal of Applied Physics* 95, 1397 (2004)

242. L. Meidong, L. Chunru, W. Peiying, R. Yunhua, Z. Yike and L. Churong: Preparation of PZT ferroelectric thin films by sol-gel processing and their properties. *Sensors & Actuators: A. Physical* 49, 191 (1995)

243. A. J. Welsh, R. H. T. Wilke, M. A. Hickner and S. Trolier-McKinstry: Low-Cost, Damage-Free Patterning of Lead Zirconate Titanate Films. *Journal of the American Ceramic Society* 96, 2799 (2013)

244. W. Zhu, T. Borman, K. DeCesaris, B. Truong, M. M. Lieu, S. W. Ko, P. Mardilovich and S. TrolierMcKinstry: Influence of PbO content on the dielectric failure of Nb-doped {100}-oriented lead zirconate titanate films. *Journal of the American Ceramic Society* 102, 1734 (2018)

245. R. G. Polcawich, C. Feng, P. Vanatta, R. Piekarz, S. Trolier-McKinstry, M. Dubey and M. Ervin: Highly accelerated lifetime testing (HALT) of lead zirconate titanate (PZT) thin filmsHighly accelerated lifetime testing (HALT) of lead zirconate titanate (PZT) thin films. *Proceedings of the th IEEE International Symposium on Applications of Ferroelectrics* 1, 357 (2000)

246. R. W. M A Angadi: Longitudinal and Transverse Strain Sensitivity of Nichrome Films. *Materials Science and Engineering B* 7, L1 (1990)

247. I. H. Kazi, P. M. Wild, T. N. Moore and M. Sayer: Characterization of sputtered nichrome (Ni–Cr 80/20 wt.%) films for strain gauge applications. *Thin Solid Films* 515, 2602 (2006)

248. A. Kaufman: Investigation of Strain Gages for Use at Cryogenic Temperatures. *Experimental Mechanics*, 1 (1963)

249. G. R. Higson: Recent advances in strain gauges. *Journal of Scientific Instruments* 41, 405 (1964)

250. J. F. Shepard, P. J. Moses and S. Trolier-McKinstry: The wafer flexure technique for the determination of the transverse piezoelectric coefficient (dyl) of PZT thin films. *Sensors & Actuators: A. Physical* 71, 133 (1998)

251. Strain Gauge Measurement – A Tutorial. *National Instruments*, Application Note 078

VITA
Ya-Wen Chuang

Education

PhD in Physics, 2020, The Pennsylvania State University, United States of America
M.S. in Physics, 2014, National Tsing-Hua University, Taiwan
B.S. in Interdisciplinary Program: Physics and Math, 2012, National Tsing-Hua University, Taiwan

Publications

- "Ferromagnetism in van der Waals compound $MnSb_{1.8}Bi_{0.2}Te_4$",
  Y. Chen, **Y.-W. Chuang**, S. H. Lee, Y. Zhu, K. Honz, Y. Guan, Y. Wang, K Wang, Z. Mao, C. Heikes, P. Quarterman, P. Zajdel, J. A. Borchers, W. Ratcliff II, and J. Zhu (accepted by Phys. Rev. Mater.)
- "Atomically thin half-van der Waals metals enabled by confinement heteroepitaxy",
  N. Briggs, B. Bersch, Y. Wang, J. Jiang, R. Koch, N. Nayir, K. Wang, M. Kolmer, W. Ko, A. Duran, S. Subramanian, C. Dong, J. Shallenberger, M. Fu, Q. Zou, **Y.-W. Chuang**, Z. Gai, A.-P. Li, A. Bostwick, C. Jozwiak, C.-Z. Chang, E. Rotenberg, J. Zhu, A. van Duin, V. Crespi, and J. Robinson, Nat. Mater. (2020)
- "Landau levels of bilayer graphene in a WSe_2/bilayer graphene van der Waals heterostructure",
  Y.-W. Chuang, J. Li, H. Fu, K. Watanabe, T. Taniguchi and J. Zhu, Phys. Rev. B 100, 195402 (2019)
- "Spin relaxation in fluorinated single and bilayer graphene",
  S. Wellnhofer, A. Stabile, D. Kochan, M. Gmitra, **Y.-W. Chuang**, J. Zhu, and J. Fabian, Phys. Rev. B 100, 035421 (2019)
- "Purification of Single Photons from Room-Temperature Quantum Dots",
  S.-W. Feng, C.-Y. Cheng, C.-Y. Wei, J.-H. Yang, Y.-R. Chen, **Y.-W. Chuang**, Y.-H. Fan, and C-S. Chuu, Phys. Rev. Lett. 119, 143601 (2017)

Conference Presentations

- American Physical Society March Meeting, Boston   March 2019
  "A different Landau level energy diagram in bilayer graphene proximitized by WSe_2"
- American Physical Society March Meeting, New Orleans March 2017
  "Transport and magneto-transport study of ultrathin WSe_2"